

## ABSTRACT

Bray, Kevin Robert. Surface Mechanisms in Low-Temperature Plasma Deposition of Silicon (under the direction of Dr. Gregory N. Parsons).

Dynamic scaling of surface roughness evolution during plasma deposition of amorphous silicon is utilized to characterize surface transport mechanisms. Different surface transport mechanisms leave distinct imprints in the surface that can be distinguished through fractal analysis. Surface roughness is characterized using atomic force microscopy (AFM) and the static and dynamic scaling coefficients  $\alpha$  and  $\beta$  and the lateral correlation length  $L_c$  are extracted from the evolution of surface roughness and are used to identify surface mechanisms. Values of  $\alpha = 1.0$  and  $\beta = 0.3$  have been obtained, which reveal that surfaces are smoothed through surface diffusion during film growth. Temperature dependence of the  $L_c$  is used to calculate diffusion barriers with values around 0.2 eV, consistent with the diffusion of a weakly bound physisorbed species. The effects of process conditions such as substrate temperature, diluent gases composition, process pressure, RF power density, and reactor configuration on the scaling parameters have been investigated. An amorphous silicon kinetic growth model has been developed that incorporates surface coverage dependent diffusion barriers. The model reproduces most experimentally observed results, although some deposition conditions are identified where the model is not valid.

**SURFACE MECHANISMS IN LOW-TEMPERATURE  
PLASMA DEPOSITION OF SILICON**

by

**Kevin R. Bray**

A dissertation submitted to the Graduate Faculty of

North Carolina State University

in partial fulfillment of the

requirements for the Degree of

Doctor of Philosophy

**Chemical Engineering**

Raleigh, North Carolina

2002

**APPROVED BY:**

---

Dr. David F. Ollis

---

Dr. H. Henry Lamb

---

Dr. Carlton M. Osburn

---

Dr. Gregory N. Parsons  
Chair of Advisory committee

To Noel, who has been patient and supportive of me for many years.

## **BIOGRAPHY**

Kevin Robert Bray was born on January 3, 1972, in Champaign, Illinois. After a few years in Lexington, Kentucky, he moved to Cary, North Carolina. He graduated from Apex High School in 1990. After deciding to pursue a career in Chemical Engineering, he began his education at Brigham Young University in Provo, Utah, where he graduated in April 1997 with a Bachelors of Science degree. In the fall of 1997, he began his graduate education at North Carolina State University.

## ACKNOWLEDGEMENTS

I would like to thank Dr. Gregory N. Parsons for his support, advice, direction and encouragement during the course of this research. I am grateful to Dr. Parsons for his mentorship in introducing me to the field of electronic materials. Special thanks also goes to members of our research group: Ashfaquul Chowdhury and Chris Makosiej for teaching me how to use the PECVD reactor, Dr. Laura Smith for tutoring me on the use of the AFM, Atul Gupta and Kie Jin Park for providing amorphous silicon films for analysis, Jim Chambers, Jason Kelly and Dong Niu for thoughtful discussions, and Leonard Nelson for his enthusiasm and his hands on help when needed.

I am also grateful to Dr. John Robertson and Andrew Flewitt for introducing me to the methods of surface scaling and analysis and for encouraging me to pursue these studies. I am thankful for their collaboration and discussions and the samples they prepared for our analysis. I would also like to thank Dr. Edmund Seebauer and his research group for providing HSG silicon samples and for their encouragement to pursue the study of these materials. I would also like to express appreciation for Joan O'Sullivan, Henry Taylor, Harold Morton and other members of the cleanroom staff for their assistance. Special thanks to Kit Yeung for his resourceful solutions for maintaining and repairing research tools.

I acknowledge my parents for instilling in me the desire to learn and excel and for their support over the many years of school. I also thank my wife Noel for her patience and support.

I acknowledge the National Science Foundation and DARPA for their financial support of this research.

# TABLE OF CONTENTS

<b>List of Tables .....</b>	<b>xi</b>
<b>List of Figures.....</b>	<b>xii</b>
<b>Chapter 1 .....</b>	<b>1</b>
<b>1 Introduction.....</b>	<b>1</b>
1.1 Overview of the Dissertation.....	1
1.2 Low Temperature Amorphous Silicon.....	2
1.3 Plasma Processing.....	4
1.3.1 Amorphous Silicon Deposition.....	4
1.3.2 Plasma Reactors .....	5
1.4 Dynamic Scaling.....	6
1.4.1 Scaling Functions.....	6
1.4.2 Atomic Force Microscopy .....	8
1.4.3 Determination of Scaling Parameters.....	10
1.5 Overview of the Following Chapters.....	11
1.6 References .....	16
<b>Chapter 2 .....</b>	<b>24</b>
<b>2 Surface Transport Kinetics in Low Temperature Silicon Deposition Determined from Topography Evolution .....</b>	<b>24</b>
2.1 Introduction .....	26
2.2 Dynamic Scaling, and Definition of Surface Scaling Parameters .....	28
2.2.1 Characterization of Surface Morphology .....	28

2.2.2	Determination of Scaling Parameters.....	31
2.3	Experimental Method.....	32
2.3.1	Hydrogenated Amorphous Silicon Deposition .....	32
2.3.2	Topography Analysis .....	33
2.4	Results and Discussion.....	34
2.4.1	Frequency and Dimensional Analysis to Characterize Fractal Scaling ....	34
2.4.2	Effect of Thickness and Gas Composition on Scaling Coefficients .....	36
2.4.3	Silicon Nucleation and Film Coalescence .....	37
2.4.4	Effect of Temperature on Surface Transport During Silicon Deposition .	38
2.5	Summary and Conclusion .....	40
2.6	Acknowledgements.....	41
2.7	References .....	42
<b>Chapter 3</b>	<b>.....</b>	<b>58</b>
<b>3</b>	<b>Effect of Hydrogen on Adsorbed Precursor Diffusion Kinetics during</b>	
	<b>Hydrogenated Amorphous Silicon Deposition .....</b>	<b>58</b>
3.1	Introduction .....	60
3.2	Experimental Method.....	61
3.3	Results.....	61
3.4	Discussion .....	63
3.5	Conclusions .....	64
3.6	Acknowledgements.....	65
3.7	Appendex.....	65
3.8	References .....	67

<b>Chapter 4</b> .....	<b>72</b>
<b>4 Effects of Deposition Conditions on the Surface Transport Kinetics in Low</b>	
<b>Temperature Silicon Deposition</b> .....	<b>72</b>
4.1. Introduction .....	74
4.2 Experimental Method.....	75
4.2.1 Hydrogenated Amorphous Silicon Deposition .....	75
4.2.2 Topography Analysis .....	76
4.3 Results and Discussion.....	77
4.3.1 Temperature and Process Pressure.....	77
4.3.2 Diluent Gas .....	79
4.3.2 RF Power Density .....	80
4.4 Summary and Conclusion .....	81
4.5 Acknowledgements.....	83
4.6 References .....	84
<b>Chapter 5</b> .....	<b>95</b>
<b>5 Substrate Temperature Dependence of the Dynamic Scaling Coefficient during</b>	
<b>Plasma Deposition of Silicon</b> .....	<b>95</b>
5.1 Introduction .....	97
5.2 Experimental Method.....	101
5.3 Results and Discussion.....	101
5.4 Conclusions .....	104
5.5 Acknowledgements.....	104
5.6 References .....	105

<b>Chapter 6 .....</b>	<b>111</b>
<b>A Surface Hydride-Dependent Precursor Diffusion Model for Low Temperature Amorphous Silicon Deposition.....</b>	<b>111</b>
6.1 Introduction .....	113
6.2 Kinetic Model .....	117
6.2.1 Valence Balance for the Surface Atoms.....	117
6.2.2 Overall Site Balance Equation for the Surface Atoms.....	120
6.2.3 Surface Reactions.....	121
6.2.4 Site Balance Equations for Various Surface Species.....	128
6.3 Results .....	132
6.3.1 Effect of Temperature .....	133
6.3.2 Effect of Incident Precursor Flux on Surface Composition .....	136
6.4 Macroscopic Parameters .....	138
6.4.1 Determining the Macroscopic Parameters Characterizing Film Growth	138
6.4.2 Comparison with Experiments.....	145
6.5 Conclusions .....	150
6.6 Acknowledgements.....	151
6.7 References .....	152
<b>Chapter 7 .....</b>	<b>177</b>
<b>7 Intrinsic Diffusivity of Silicon on Silicon .....</b>	<b>177</b>
7.1 Introduction .....	179
7.2 Experimental Method.....	181
7.3 Results.....	181

7.4	Discussion .....	183
7.5	Conclusions .....	183
7.6	Acknowledgements.....	184
7.7	References .....	185
<b>Chapter 8 .....</b>		<b>190</b>
<b>8 Conclusions and Future Studies.....</b>		<b>190</b>
8.1	Conclusions .....	190
8.1.1	Dynamic Scaling.....	190
8.1.2	Kinetic Parameters .....	191
8.1.3	Kinetic Model .....	191
8.2	Future Studies .....	192
8.2.1	Dynamic Scaling.....	192
8.2.2	Kinetic Model .....	193

## LIST OF TABLES

Table 2.1: Summary of scaling coefficients, coalescence time and correlation length for various source gas, substrates and substrate temperatures. The static scaling coefficient, $\alpha$ , is determined from dimensional analysis, and Fourier index is obtained from frequency analysis.....	44
Table 6.1(a): List of Reactions (and the corresponding rate expressions) used in the model.....	155
Table 6.1(b): List of Reaction Rate parameters used in the model. The rate constants, $u_n$ , are given as $A_n \exp(-E_n/k_B T)$ , here $k_B$ is the Boltzmann's constant and $h$ is Planck's constant. ....	156

## LIST OF FIGURES

Fig. 1.1: Radial gas flow PECVD reactor schematic. ....	20
Fig. 1.2: Large area PECVD reactor schematic. ....	21
Fig. 1.3: Effect of tip radius on resolution of features in AFM. ....	22
Fig 1.4: Schematic of how AFM determines surface topography during tapping mode. ....	23
Fig. 2.1: Artificial self-similar and self-affine profiles. Isotropic magnification of a) self-similar and b) self-affine profiles are shown in the circles. ....	45
Fig. 2.2: Power spectral density plots for a) 1000 Å a-Si:H film deposited by plasma CVD from SiH <sub>4</sub> /He; and b) 1.5 μm Al deposited by evaporation. The spectrum is observed to decrease with a slope of $i$ , the Fourier index, above the critical frequency $q_c$ . The a-Si has a larger value for $i$ , indicating surface diffusion is more prominent than in the evaporation process. ....	46
Fig. 2.3(a): RMS roughness vs. length scale. Comparison between PECVD a-Si:H and evaporated Al. Evaporated Al has a smaller $\alpha$ , indicating it has a rougher surface than the plasma deposited a-Si. The roughness of the a-Si film saturates at a critical length, $L_c$ , of 75 nm while the Al film has an $L_c$ of 300 nm. ....	47
Fig. 2.3(b): RMS roughness vs. length scale. Comparison of deposition time for films deposited at 25°C. The static scaling coefficient $\alpha$ , remains small for thin (non-coalesced) films, and then reaches a constant value for thick films. ....	48
Fig. 2.3(c): RMS roughness vs. length scale. Comparison of substrate temperature for films deposited from a SiH <sub>4</sub> /He mixture for 20 minutes. ....	49

Fig. 2.4: Saturated RMS roughness (determined by dimensional analysis) vs. deposition time for silicon deposited from SiH<sub>4</sub>/He mixtures on Si. The surface diffusion model indicates that  $\sigma$  should increase with time with a slope of  $\beta = 0.25$ . At times greater than one minute, a best fit of the roughness data yields  $\beta = 0.26 \pm 13$ . The error was determined from the quality of the least squares fit. The dashed line is an extension of the fit and does not represent a fit of the data in that region of the graph. The error bars are  $3\sigma$  values determined from >5 measurements of multiple films deposited with the same conditions.....50

Fig. 2.5(a): Initial nucleation of a-Si films grown for 30 s at a) 25°C. The films have coalesced. The 25°C film has small, jagged nuclei while the 100°C film has larger, rounder nuclei.....51

Fig. 2.5(b): Initial nucleation of a-Si films grown for 30 s at 100°C. The films have coalesced. The 25°C film has small, jagged nuclei, while the 100°C film has larger, rounder nuclei.....52

Fig. 2.6(a): Fully developed nucleation of films grown for 3 min at 25°C.....53

Fig. 2.6(b): Fully developed nucleation of films grown for 3 min at 100°C. There are no distinguishable differences between the topographies of the surfaces. ....54

Fig. 2.7(a): Dependence of static scaling coefficient on deposition time and temperature for a-Si films deposited on c-Si substrates.  $\alpha$  increases with deposition time until it saturates at  $\alpha=1$ . The increase occurs more rapidly as temperature increases. Coalescence was determined by direct qualitative analysis of AFM images. A similar trend occurs for films grown on both c-Si and glass. The curves are guides for the eye.....55

Fig. 2.7(b): Dependence of static scaling coefficient on deposition time and temperature for a-Si films deposited on glass substrates.  $\alpha$  increases with deposition time until it saturates at  $\alpha=1$ . The increase occurs more rapidly as temperature increases. Coalescence was determined by direct qualitative analysis of AFM images. A similar trend occurs for films grown on both c-Si and glass. The curves are guides for the eye.....56

Fig. 2.8: Arrhenius plot of  $L_c^2$  for samples deposited for 20 minutes. The linear slope indicates a thermally activated diffusion process with an activation energy of  $E_a = 0.2\text{eV}$ .....57

Fig. 3.1: Fractal analysis of  $1000\text{\AA}$  a-Si:H films deposited with varying helium and hydrogen dilutions. a)  $\text{SiH}_4/\text{He}$  1/49, b)  $\text{SiH}_4/\text{He}$  1/99, c)  $\text{SiH}_4/\text{He}/\text{H}_2$  1/49/50, d)  $\text{SiH}_4/\text{He}/\text{H}_2$  1/149/50. The correlation length,  $L_c$ , where the RMS roughness saturates with length, increases with hydrogen dilution. The curves are offset for clarity. Lines are guides for the eye.....69

Fig. 3.2: The correlation length,  $L_c$  vs. the  $\text{H}_2/\text{SiH}_4$  ratio.  $L_c$  remains constant with low  $\text{H}_2$  dilutions, then increases with high hydrogen dilutions for films deposited at a)  $25^\circ\text{C}$ , b)  $100^\circ\text{C}$ , and c)  $150^\circ\text{C}$ . The lines are guides for the eye.....70

Fig. 3.3: Arrhenius plots of  $\ln(L_c^2)$  vs.  $1/T$  for a-Si:H films deposited from  $\text{SiH}_4$  (from reactor two),  $\text{SiH}_4/\text{He}$  and  $\text{SiH}_4/\text{He}/\text{H}_2$  mixtures (from reactor one).....71

Fig. 4.1(a): Effect of Process Pressure. Arrhenius plot of  $\ln(L_c^2)$  vs.  $1/T$  at various pressures.....86

Fig. 4.1(b): Effect of Process Pressure. RMS Roughness vs. measurement length for various pressures.....87

Fig. 4.2: Arrhenius plot of  $\ln(L_c^2)$  vs.  $1/T$  for films deposited from  $\text{SiH}_4/\text{H}_2$  in reactor 1 and reactor 2. Below  $150^\circ\text{C}$ , both processes show the same activation barrier. Films above  $150^\circ\text{C}$  in showerhead reactor show a shift in the activation barrier. 88

Fig. 4.3(a): Atomic force microscopy images of films deposited from pure  $\text{SiH}_4$  at  $150^\circ\text{C}$  in the showerhead reactor..... 89

Fig. 4.3(b): Atomic force microscopy images of films deposited from pure  $\text{SiH}_4$  at  $350^\circ\text{C}$  in the showerhead reactor..... 90

Fig. 4.4(a): Atomic force microscopy images of films deposited from  $\text{SiH}_4/\text{H}_2$  at  $150^\circ\text{C}$  in the showerhead reactor..... 91

Fig. 4.4(b): Atomic force microscopy images of films deposited from  $\text{SiH}_4/\text{H}_2$  at  $350^\circ\text{C}$  in the showerhead reactor..... 92

Fig. 4.5: RMS Roughness vs. measurement length for films deposited from  $\text{SiH}_4/\text{H}_2$  at  $25^\circ\text{C}$  and  $350^\circ\text{C}$ . Both films exhibit a static scaling coefficient of  $\alpha = 0.7$ , indicating the same transport mechanism dominates the growth process at both temperatures. .... 93

Fig. 4.6: Effect of RF Power Density. Activation barrier ( $E_a$ ) and Correlation Length ( $L_c$ ) vs. Power Density.  $L_c$  increases with increasing power, while  $E_a$  remains constant. The lines are guides to the eye..... 94

Fig. 5.1. Saturated RMS Roughness vs. deposition time for films deposited from  $25^\circ\text{C}$  to  $300^\circ\text{C}$ . Dynamic scaling coefficient,  $\beta$ , is extracted from a best fit of the data. 108

Fig. 5.2(a): Dynamic scaling coefficient,  $\beta$ , vs. substrate temperature. Includes data from Figure 5.1 and previously published data from the literature for RFPECVD amorphous silicon deposition. The line is a guide to the eye..... 109

Fig 5.2(b): Dynamic scaling coefficient, $\beta$ , vs. substrate temperature from Ref. [7] for expanding thermal plasma deposition of amorphous silicon. ....	110
Fig. 6.1(a): Distribution of different surface hydrides vs. temperature for $E_a(\text{abs}) = 0.4$ eV for Flux = 1/sec. ....	157
Fig. 6.1(b): Distribution of different surface hydrides vs. temperature for $E_a(\text{abs}) = 0.4$ eV for Flux = 10/sec. ....	158
Fig. 6.1(c): Distribution of different surface hydrides vs. temperature for $E_a(\text{abs}) = 0.4$ eV for Flux = 100/sec. ....	159
Fig. 6.1(d): Distribution of different surface hydrides vs. temperature for $E_a(\text{abs}) = 0.4$ eV for Flux = 400/sec. ....	160
Fig. 6.1(e): Distribution of different surface hydrides vs. temperature for $E_a(\text{abs}) = 0.1$ eV for Flux = 10/sec. ....	161
Fig. 6.2: Variation of surface layer H content with temperature for varying silyl radical flux. (a) Flux = 1/sec, (b) Flux = 10/sec, (c) Flux = 100/sec, (d) Flux = 400/sec for $E_a(\text{abs}) = 0.4$ eV and (e) Flux = 10/sec and $E_a(\text{abs}) = 0.1$ eV. ....	162
Fig. 6.3(a): Effect of temperature on the surface dangling bond concentrations. Overall surface dangling bond concentration vs. temperature for silyl radical flux (a) Flux = 1/sec, (b) Flux = 10/sec, (c) Flux = 100/sec and (d) Flux = 400/sec for $E_a(\text{abs}) = 0.4$ eV and (e) Flux = 10/sec and $E_a(\text{abs}) = 0.1$ eV. ....	163
Fig. 6.3(b): Effect of temperature on the surface dangling bond concentrations. Contribution of individual mechanisms to dangling bond creation, including creation of dangling bonds by direct H abstraction by H, assuming H flux equal to silyl flux for $E_a(\text{abs}) = 0.4$ eV. ....	164

Fig. 6.3(c): Effect of temperature on the surface dangling bond concentrations.  
 Contribution of individual mechanisms to dangling bond removal for  $E_a(\text{abs}) = 0.4 \text{ eV}$ ..... 165

Fig 6.4: Effect of temperature on the surface coverage of physisorbed radicals for varying silyl radical flux with  $E_a(\text{abs}) = 0.4 \text{ eV}$  (a) Flux = 1/sec, (b) Flux = 10/sec, (c) Flux = 100/sec and (d) Flux = 400/sec and (e) Flux = 10/sec with  $E_a(\text{abs}) = 0.1 \text{ eV}$ ..... 166

Fig. 6.5: Surface Si-Si bond ( $q_5$ ) fraction vs. temperature for varying silyl radical flux with  $E_a(\text{abs}) = 0.4 \text{ eV}$  (a) Flux = 1/sec, (b) Flux = 10/sec, (c) Flux = 100/sec and (d) Flux = 400/sec and (e) Flux = 10/sec with  $E_a(\text{abs}) = 0.1 \text{ eV}$ ..... 167

Fig. 6.6: Schematic of various reaction and sticking probabilities on the surface..... 168

Fig. 6.7(a): Growth rate variations with deposition conditions (temperature, silyl radical flux and hydrogen abstraction barrier)..... 169

Fig 6.7(b): Contribution of different incorporation pathways to growth rate for Flux = 10/sec and  $E_a(\text{abs}) = 0.4 \text{ eV}$ . ..... 170

Fig 6.7(c): Contribution of different incorporation pathways to growth rate for Flux = 10/sec and  $E_a(\text{abs}) = 0.1 \text{ eV}$ . ..... 171

Fig. 6.8: Reaction and sticking probabilities ( $\alpha$  and  $s$ ) predicted by the kinetic model vs. temperature for varying silyl radical flux with  $E_a(\text{abs}) = 0.4 \text{ eV}$ . (a) Flux = 1/sec, (b) Flux = 10/sec, (c) Flux = 100/sec, and (d) Flux = 400/sec and (e) Flux = 10/sec with  $E_a(\text{abs}) = 0.1 \text{ eV}$ . ..... 172

Fig. 6.9(a): Diffusion length vs. temperature for varying silyl radical flux with  $E_a(\text{abs}) = 0.4 \text{ eV}$ ..... 173

Fig. 6.9(b): Semi-log plot of  $L_d^2$  vs  $1/T$  to calculate the apparent activation barriers for the diffusion of physisorbed radicals on the surface for varying silyl radical flux with  $E_a(\text{abs}) = 0.4$  eV. .... 174

Fig. 6.9(c): Diffusion length vs. temperature for silyl radical flux = 10/sec with  $E_a(\text{abs}) = 0.1$  eV..... 175

Fig 6.9(d): Semi-log plot of  $L_d^2$  vs  $1/T$  to calculate the apparent activation barriers for the diffusion of physisorbed radicals on the surface for silyl radical flux = 10/sec with  $E_a(\text{abs}) = 0.1$  eV..... 176

Fig. 7.1: Atomic force microscopy image of HSG silicon surface. Two regions of the surface are observed. Region (a) consists of several large HSG grains and region (b) consists of the smooth, amorphous silicon between the grains. .... 186

Fig. 7.2. Dimensional fractal analysis of HSG silicon regions (a) and (b). RMS Roughness increases with measurement length and then saturates..... 187

Fig. 7.3. Static scaling coefficient,  $\alpha$ , vs. anneal temperature.  $\alpha$  remains constant with temperature..... 188

Fig. 7.4. Arrhenius plot of  $L_c^2$  vs.  $1/T$  for correlation length obtained from region (b). Diffusion barrier of  $E_a = 0.88 \pm 0.38$  eV is obtained from a best fit of the data. 189

# CHAPTER 1

## 1 INTRODUCTION

### 1.1 OVERVIEW OF THE DISSERTATION

The past few decades have presented an unprecedented growth in the semiconductor industry. Improvements in manufacturing and processing have provided high quality materials for improved device performance. As this momentum is carried into the 21<sup>st</sup> century, a better understanding of the fundamentals of thin film growth and surface transport properties are needed to further improve material quality and sustain device quality. This dissertation focuses on improving our understanding of the transport properties that control the surface roughness of hydrogenated amorphous silicon (a-Si:H) deposited at low temperatures using plasma enhanced chemical vapor deposition (PECVD) techniques. Hydrogenated amorphous silicon deposition results in smooth conformal films over a wide temperature range. Several kinetic models attempting to describe the growth process and explain experimental results have been proposed. But these attempts have not been successful in replicating experimentally observed trends with realistic kinetic parameters.

This dissertation aims at identifying the dominant surface transport mechanism leading to smooth films during a-Si:H deposition. This is accomplished through the use of a fractal analysis technique that extracts information about surface

transport from an examination of the surface topography evolution. These results are then coupled with a new “valence balance” approach to develop a new quantitative kinetic growth model for a-Si:H.

## **1.2 LOW TEMPERATURE AMORPHOUS SILICON**

Traditionally, semiconductor devices are processed at high temperatures in order to obtain the best electrical and materials properties needed for optimal performance. As industry approaches the sub 150 nm device range, thermal constraints become more important and lower temperature processing is necessary to control dopant diffusion and activation. New device structures involving amorphous silicon and dielectrics integrated on top of complementary MOS (CMOS) devices will require low temperature processes. Ideally, room temperature fabrication of both amorphous silicon (a-Si) and dielectrics would be desirable.

Hydrogenated amorphous silicon (a-Si:H) has been widely studied for use as thin film transistors (TFT) in active matrix liquid crystal displays and as solar cells. The optimum substrate temperature for deposition is between 200 – 300°C [1-5]. There has been much interest recently in producing high-quality a-Si:H films at low temperatures [1-11]. Different reactor geometries in PECVD systems, including tubular reactors [1], asymmetric reactors [9, 12], and heated mesh above the substrate [8] have been developed to deposit a-Si:H at low temperatures. Alternative techniques such as reactive magnetron sputtering (RMS) [4, 13], inductively coupled plasma [5, 14], hot wire CVD [15], and thermal evaporation [16] have also been used to deposit low temperature

a-Si:H. The majority of these as-deposited films do not show very good photoelectric properties. These properties improve dramatically upon annealing [2, 4, 7, 9, 12, 17]. There are a few reports of a-Si:H films deposited at temperatures  $< 100^{\circ}\text{C}$  with photoconductivities of  $10^{-5} \text{ S / cm}$  using an inductively coupled plasma [14] and PECVD in a “super chamber” [18] without annealing.

The deposition process can also be modified to improve the photoelectric properties of the deposited films. Intermittent deposition, where a shutter periodically blocks the substrate and prevents deposition, has been shown to decrease the defect density in the a-Si:H films [11, 19]. The properties improve with increased waiting time (closed shutter). Ultraviolet illumination of the substrate during deposition has also increased the photoconductivity, for both continuous and intermittent deposition [10]. Hydrogen dilution has also been shown to improve a-Si:H film properties [5, 9, 18].

An important use of amorphous silicon is in thin film transistors (TFTs) for active matrix flat panel displays. Although current flat panel display technology utilizes liquid crystals for creating images, organic light emitting diode (OLED) technology has been improving and has expanded the possibility of developing active matrix OLED displays. The organic materials used in these displays cannot withstand processing above  $\sim 200 - 250^{\circ}\text{C}$ , which limits the device design and processing temperature. Research is also progressing in the development of TFTs on flexible, transparent, polymeric substrates. These polymers decompose at temperatures above  $\sim 200^{\circ}\text{C}$  and will also require lower temperature processing.

## 1.3 PLASMA PROCESSING

### 1.3.1 Amorphous Silicon Deposition

Plasma enhanced chemical vapor deposition (PECVD) is widely used to deposit amorphous silicon. The most obvious advantage of plasma deposition is that it allows thin films to be deposited on almost any substrate at the desired temperature. But plasma processes are complex. A silicon containing source gas, usually  $\text{SiH}_4$  or  $\text{Si}_2\text{H}_6$ , is flowed into a deposition chamber. Plasma is generated between the electrodes by applying a radio frequency (RF) power source. Ions, radicals and electrons are all created within the gases in the plasma. Thousands of reactions are occurring in the gas phase. There has been a significant amount of research devoted to characterizing plasma reactions for amorphous silicon deposition. The silyl radical ( $\text{SiH}_3$ ) has been identified as the primary precursor for a-Si growth from a silane plasma. For years, it was believed that a-Si growth proceeded through a physisorbed Si-H-Si three-centered bond [20-23]. Recent calculations have shown this three-centered bond configuration is not stable [24, 25]. Recent experiments indicate that  $\text{SiH}_3$  may insert directly into strained Si-Si bonds on the surface [26]. There is still not a complete understanding of how plasma process conditions, such as power, temperature, pressure and gas dilutions, impact the surface topography of the growing film.

### 1.3.2 Plasma Reactors

There are many different methods for low temperature PECVD. The most common design is “direct” plasma, which involves a capacitively coupled radio-frequency (RF) power source where the sample is loaded onto the cathode while the RF power is supplied to the anode. Plasma is generated between the electrodes and the radicals generated lead to deposition both on the substrate and the reactor walls. A different approach that is gaining acceptance is remote PECVD. Here the plasma is generated away from the substrate to reduce ion bombardment on the surface. Remote PECVD also allows better control of the reactions by selectively exposing gases to the plasma and injecting precursors near the substrate. Although this technique is not as well adept for large area deposition, advances in reactor and process modeling are making it more feasible for industrial use. Several novel plasma reactor configurations have been studied to produce high quality hydrogenated amorphous silicon at low temperatures.

Figures 1.1 and 1.2 show the deposition tools used for a-Si:H growth. The first reactor used for amorphous silicon deposition is a capacitively coupled rf (13.56 MHz) parallel plate PECVD system with circular geometry (2.2 cm electrode separation, 28 cm diameter) and radial gas flow. The second reactor utilized in these experiments is a large area (1000 cm<sup>2</sup>) load-locked, parallel plate PECVD reactor with an electrode spacing of 1.6 cm. A showerhead gas distribution system is used for the uniform delivery of gases into the reaction zone, resulting in uniform film growth over the electrode area.

## 1.4 DYNAMIC SCALING

### 1.4.1 Scaling Functions

Surface morphology of deposited films, determined using scanning electron microscopy, scanning probe microscopy, or small angle X-ray scattering techniques, is typically analyzed using a height-height correlation function

$$C(R) = \langle z(r)z(r+R) \rangle_{r,R} \quad (1)$$

or a height-difference correlation function:

$$G(R) = \langle [z(r) - z(r+R)]^2 \rangle_{r,R} \quad (2)$$

where  $z(r)$  is the height at any point  $r$  on the surface and  $\langle \rangle_{r,R}$  refers to the average over all pairs of surface points separated by a distance  $R$ . The data is then compressed and displayed in terms of a power spectral density function:

$$g(|q|) = F[C(|r|)] \quad (3)$$

where  $F$  is the two-dimensional Fourier transform operator. Early models used Gaussian or modified Gaussian functions to describe and predict surface correlation functions [27] which allowed the surface structure to be described by a minimal set of parameters including the standard deviation of the surface height, and the lateral correlation length. Later models utilized concepts of topographical scaling, where surface self-affinity or surface self-similarity is used to describe growing surfaces [28]. The height-difference correlation function can also be written in terms of a scaling function,  $f(R/L_c)$ :

$$G(R) = 2s^2 f(R/L_c) \quad (4)$$

where  $\sigma$  is the root mean square roughness of the surface, and  $L_c$  is the maximum lateral length scale over which surface roughness correlations persist [27]. The scaling function has an asymptotic form  $f(x) = (R/L_c)^{2\alpha}$  for  $x < 1$ , and  $f(x) = 1$  for  $x > 1$ , where  $\alpha$  is the static scaling coefficient (or Hurst parameter). Values for the static scaling coefficient range from 0 – 1, with  $\alpha$  approaching 0 for jagged surfaces and 1 for smooth surfaces [29]. For the dynamic scaling hypothesis proposed by Sinha et.al. [30] the height-height correlation function is written as an exponential:

$$C(R) = \mathbf{s}^2 \exp[-(R/L_c)^{2a}] \quad (5)$$

Dynamic scaling also predicts that for a self-affine surface, the root-mean-square (rms) roughness of the surface scales as:

$$\mathbf{s} \sim R^a f(t^b / R^a) \quad (6)$$

where  $t$  is the deposition time (proportional to film thickness) and  $\beta$  is the dynamic or temporal scaling exponent [27, 31].

Surface kinetic models describe the balance between random arrival of species from the gas phase and a variety of thermally activated processes that operate on the surface. For growth of thin films from the vapor phase, if the species responsible for film deposition are randomly incorporated into the surface without appreciable surface transport, then stochastic, or random, surface growth will result in a rough surface. In the early 1950s, Herring described four distinct surface transport mechanisms that reduce surface roughness: i) viscous flow; ii) evaporation-condensation; iii) bulk diffusion and iv) surface diffusion [32]. The relationship between the surface topography and the surface transport mechanism comes from an analysis of the time and amount of material needed to produce a geometrically similar change in two different sized clusters using

each mechanism. These mechanisms leave distinct imprints on the topography that are recognizable through fractal analyses. In 1986, Kardar, Parisi and Zhang described the development of surface roughness based on symmetry arguments [33]. Later models related the symmetry models to transport processes using equations of motion with terms corresponding to specific surface smoothing or roughening mechanisms [27]. Continuum models including linear and non-linear terms in the equations of motion are used to analyze surface roughness data to determine scaling coefficients under different conditions. Matching the experimentally determined scaling exponents with continuum growth models then identifies the primary transport mechanisms.

#### **1.4.2 Atomic Force Microscopy**

Atomic force microscopy (AFM) is useful for studying surface topography and nucleation of thin films. We use a Digital Instruments Dimension 3000 AFM. Two modes are available to image surfaces. First is contact mode. In this mode, a stylus is brought into contact with the surface. The stylus is then dragged across the surface maintaining contact. A silicon nitride tip is used for this mode of imaging. A laser is reflected off the back of the tip and records the motion to image the topography. There are some disadvantages to imaging in contact mode. Because the tip is moving directly across the surface, it is possible to damage the surface during imaging. The tip radius ranges from 20 – 60 nm. The tip radius limits the lateral resolution that can be achieved during imaging. Figure 1.3 is a schematic of the effect of the tip radius on the ability to sample surface features.

Tapping mode is the second option available for surface imaging. The surface probe consists of a silicon tip that is oscillated near its resonance frequency. A laser reflects off the tip and the deflection pattern is recorded with a photodiode to create a regular sinusoidal electronic signal. To obtain the surface topography, the oscillating tip is brought in contact with the surface. Contact with the surface alters the tip oscillation pattern and an algorithm transposes the changes in the oscillation pattern into a topographic image of the surface. Figure 1.4 is a schematic of how the tip oscillations change as the tip interacts with the surface. There are two major advantages in tapping mode over contact mode. First, the nominal tip radius is 5 – 10 nm. This allows higher lateral resolution. The lateral resolution is important in the scaling analysis where the roughness change with lateral size of the image is used to extract coefficients. The second advantage is that the tip is not in continuous contact with the surface during tapping mode. This helps reduce tip induced damage or artifacts during imaging, especially when examining soft samples. Tapping mode was used for all imaging discussed in this thesis.

Built into the software is an algorithm for calculating RMS roughness. The RMS roughness is calculated as:

$$\mathbf{s} = \left[ \frac{\sum (Z_i - Z_{ave})^2}{N} \right]^{\frac{1}{2}} \quad (7)$$

where  $Z_i$  is the height at point  $i$ ,  $Z_{ave}$  is the average height of the surface, and  $N$  is the number of points included in the measurement. The program allows for smaller areas with the image to be selected. This technique allows the roughness over multiple length scales to be determined from one image. To facilitate analysis of the data, we prepared a macro in Igor Pro that imports the surface height data from the AFM scans and calculates

RMS roughness over several length scales within the image. Several scan sizes were measured to insure there were no artificial effects introduced into the analysis from the scan size. The PSD is another function that can be calculated with the AFM software. The square of the Fourier Transform is radially averaged and normalized in the radial direction. Comparison between the static scaling coefficient and the lateral correlation length showed close agreement between the RMS roughness method and the PSD analysis.

### 1.4.3 Determination of Scaling Parameters

Both the static scaling coefficient,  $\alpha$ , and the dynamic scaling coefficient,  $\beta$ , are needed to distinguish surface transport mechanisms uniquely. Two methods, dimensional and frequency analysis are used to analyze topography data. Dimensional analysis involves determining RMS surface roughness at various length scales ( $L$ ) and deposition times ( $t$ ), then obtaining scaling coefficients [27, 34] using  $\sigma \sim L^\alpha$  and  $\sigma_{\text{sat}} \sim t^\beta$ . Frequency analysis utilizes the Fourier transform of the surface topography [35, 36] to obtain the power spectral density (PSD). The one dimensional PSD is obtained by using the radius in reciprocal space as the spatial frequency and radially averaging the two dimensional spectrum [37]. The Fourier index is determined from the PSD using the power law relationship  $\text{PSD} \sim q^{-i}$  for wavenumbers  $q$  greater than a critical frequency,  $q_c$  (inverse of the critical length,  $q_c=1/L_c$ ), and  $\alpha$  is determined directly from  $i$ . Radial averaging generally gives a better correlation with fractal dimension than linear averaging. For the dimensional analysis, RMS roughness was calculated on different

length scales. The roughness increased with increasing length up to a critical length where the roughness saturated. The static scaling coefficient is obtained from the slope of the increasing roughness and the correlation length is point where the roughness saturates.

For the linear continuum model with surface transport dominated by surface diffusion, the scaling coefficients are expected to attain values of  $\alpha = 1$  and  $\beta = 0.25$  [27, 38, 39]. When nonlinear terms are included, scaling coefficients of  $\alpha = 0.67$  and  $\beta = 0.2$  are expected for diffusion [39]. For transport by evaporation and condensation [27], expected values are  $\alpha = 0$  and  $\beta = 0$ . There are several reports analyzing kinetic smoothing mechanisms of hydrogenated amorphous silicon deposited using plasma deposition [40, 41] and thermal evaporation [16]. Typically,  $\alpha$  is measured between 0.8 – 1 and  $\beta$  between 0.2 – 0.33, consistent with self-similar geometry and transport by surface diffusion. As expected, these values are distinctly different from parameters typically reported for evaporated metal surfaces. Static scaling coefficients are typically  $\sim 0.7$ - $0.8$  with  $\alpha = 0.82$  for Ag and  $\alpha = 0.68$  for Pt [38], which are consistent with values reported for surface diffusion and step growth [27, 38], i.e.  $\alpha = 0.67$  and  $\beta = 0.2$ .

## **1.5 OVERVIEW OF THE FOLLOWING CHAPTERS**

Understanding the kinetics of surface processes is an important issue for controlling film quality. With current trends toward lower temperature processing, thermodynamic balances, which apply in the equilibrium limit, are no longer sufficient to explain film properties. To date, results directly identifying surface transport kinetic

processes in low temperature silicon growth are not available. The technique for surface transport analysis presented and utilized here employs direct surface characterization, and does not require identification or supposition of the particular gas-phase precursor responsible for growth, or the adsorbed surface species responsible for diffusion. The evolution of surface topography provides insight into the mechanisms occurring on the surface. In Chapter 2, we discuss the basis for a fractal analysis approach to understand film growth. Under certain deposition conditions, a-Si:H can be characterized by a surface diffusion continuum equation. After establishing that a-Si:H surface topography evolution is dominated by surface diffusion, we use fractal analyses to extract the correlation length from the surface topography. The correlation length is an estimate of the surface diffusion length and can be used to calculate kinetic parameters. Using a range of deposition conditions, we calculate a surface diffusion activation barrier,  $E_a$ , of  $\sim 0.2\text{eV}$ .

In Chapter 3, we extend the range of parameters under investigation and look at hydrogen dilution during plasma deposition. We find that small  $\text{H}_2/\text{SiH}_4$  dilution ratios decrease the precursor diffusion length while the diffusion barrier remains constant. For higher dilution ratios, we see an increase in the surface diffusion length and a decrease in the activation barrier. We discuss these results in relation with a new surface hydride dependent kinetic growth model.

A wider analysis of deposition parameters is presented in Chapter 4. The effects of RF power density and process pressure are investigated. A wider study of hydrogen dilution is also presented. Two deposition reactors were used to demonstrate the robustness of the analysis used. We observed the correlation length increased as we

increased the power density. This is attributed to an increase in low energy ion bombardment enhancing the surface mobility. The diffusion barrier remained constant with power, indicating the surface structure was unchanged. Changing the incident flux by altering the process pressure was also studied. Decrease in the radical flux increased the diffusion length and decreased the activation barrier. These results are consistent with predictions from our kinetic model presented in the Chapter 6. Arrhenius plots for films deposited from  $H_2/SiH_4$  in two plasma reactors were compared. A difference in the correlation length was noticeable between the two systems, but the diffusion barrier from each reactor was equal. This demonstrates that the same surface processes are dominating in both systems and the analysis is not system dependent. The amorphous to microcrystalline transition can be seen with a change in the activation barrier, but the scaling analysis shows that the same surface transport mechanisms are dominant on both the amorphous and microcrystalline surfaces.

Chapter 5 focuses on the temperature dependence of the scaling coefficients obtained through the fractal analysis. Specifically, the dynamic scaling coefficient,  $\beta$ , is examined vs. substrate temperature.  $\beta$  is found to remain constant with temperature from 25°C to 300°C. These results indicate that the dominant surface transport mechanism remains constant with substrate temperature. This result is consistent with trends predicted by our kinetic model discussed in Chapter 6. Surface growth is dominated by the addition of mobile physisorbed radicals until the hydrogen desorption temperature is reached.

A new surface hydride dependent kinetic model is presented in Chapter 6. Two key ingredients differentiate it from previous models for amorphous silicon growth.

First, it proposes that the surface diffusion barrier is surface coverage dependent. The diffusion barrier for a radical physisorbed on a tri-hydride surface will differ from the barrier on a mono- or di-hydride surface. The second key to the model is the introduction of a “valence balance”. The valence balance counts each bond on the surface, not just atoms, and allows bond dependent reactions, such as insertion into a strained Si bond and Si-Si network bond formation, to be accounted for along with the traditional site balance. Model predictions are discussed and compared with available experimental data. The model is consistent with all of the available data.

Hemispherical grained silicon (HSG) provides a unique opportunity to study surface diffusion on amorphous materials. HSG forms by surface-diffusion-driven crystallization of a-Si that begins at the free surface above about 600°C. The crystallites mushroom out of the surface as small grains up to 100 nm in size. Since the grain shape is roughly size-invariant, the growth is limited by diffusion over the a-Si surface. In Chapter 7, fractal analysis of HSG surface topography is used to extract scaling coefficients and correlation lengths. The coefficients confirm surface diffusion dominates the topography evolution and values for the intrinsic diffusion of silicon on silicon are calculated from the correlation lengths.

In Chapter 8, we recount the key results and conclusions from our work. Dynamic scaling has been used to obtain kinetic parameters for surface diffusion. Thermally activated surface diffusion has been observed. Apparent diffusion barriers have been estimated from correlation lengths. The diffusion barriers depend on the process conditions. The kinetic model we developed reproduces several experimental

trends in amorphous silicon growth. In this chapter we also propose future experiments and research to increase our understanding of amorphous silicon.

## 1.6 REFERENCES

- [1] J.P. Conde, K.K. Chan, J.M. Blum, and J.J. Cuomo, *Journal of Applied Physics*, **71**, 3981 (1992).
- [2] M.K. Cheung and M.A. Petrich, *Journal of Applied Physics*, **73**, 3237 (1993).
- [3] P. Roca i Cabarrocas, *Applied Physics Letters*, **65**, 1674 (1994).
- [4] G.N. Parsons, C. Wang, M.J. Williams, and G. Lucovsky, *Journal of Non-Crystalline Solids*, **114**, 178 (1989).
- [5] M. Goto, H. Toyoda, M. Kitagawa, T. Hirao, and H. Sugai, *Japanese Journal of Applied Physics Part 1-Regular Papers Short Notes & Review Papers*, **36**, 3714 (1997).
- [6] G. Lucovsky, B.N. Davdison, G.N. Parsons, and C. Wang, *Journal of Non-Crystalline Solids*, **114**, 154 (1989).
- [7] M. Kunst and H.-C. Neitzert, *Journal of Applied Physics*, **69**, 8320 (1991).
- [8] A. Matsuda, *Plasma Physics and Controlled Fusion*, **39**, 431 (1997).
- [9] T. Seth, P.N. Dixit, C. Mukherjee, C. Anandan, and R. Bhattacharyya, *Thin Solid Films*, **264**, 11 (1995).
- [10] A. Suzuki, G. Ganguly, and A. Matsuda, *Applied Physics Letters*, **63**, 2806 (1993).
- [11] T. Kamei, N. Hata, and A. Matsuda, *Journal of Non-Crystalline Solids*, **200**, 999 (1996).
- [12] O.S. Panwar, C. Mukherjee, and R. Bhattacharyya, *Solar Energy Materials & Solar Cells*, **57**, 373 (1999).

- [13] C.S. McCormick, C.E. Weber, J.R. Abelson, G.A. Davis, R.E. Weiss, and V. Aebi, *Journal of Vacuum Science & Technology a-Vacuum Surfaces and Films*, **15**, 2770 (1997).
- [14] M. Goto, H. Toyoda, M. Kitagawa, T. Hirao, and H. Sugai, *Japanese Journal of Applied Physics Part 2-Letters*, **35**, L1009 (1996).
- [15] M.B. Schubert, *Thin Solid Films*, **337**, 240 (1999).
- [16] H.-N. Yang, Y.-P. Zhao, G.-C. Wang, and T.-M. Lu, *Physical Review Letters*, **76**, 3774 (1996).
- [17] J.P. Conde, K.K. Chan, J.M. Blum, M. Arienzo, P.A. Monteiro, J.A. Ferreira, V. Chu, and N. Wyrsh, *Journal of Applied Physics*, **73**, 1826 (1993).
- [18] Y. Hishikawa, S. Tsuge, N. Nakamura, S. Tsuda, S. Nakano, and Y. Kuwano, *Journal of Applied Physics*, **69**, 508 (1991).
- [19] T. Kamei, G. Ganguly, N. Hata, and A. Matsuda, *Journal of Non-Crystalline Solids*, **164-166**, 43 (1993).
- [20] J.R. Abelson, *Applied Physics A*, **56**, 493 (1993).
- [21] J. Perrin, M. Shiratani, P. Kae-Nune, H. Videlot, J. Jolly, and J. Guillon, *Journal of Vacuum Science and Technology A*, **16**, 278 (1998).
- [22] A. Matsuda, K. Nomoto, Y. Takeuchi, A. Suzuki, A. Yuuki, and J. Perrin, *Surface Science*, **227**, 50 (1990).
- [23] G. Ganguly and A. Matsuda, *Journal of Non-Crystalline Solids*, **164-166**, 31 (1993).
- [24] A. Gupta, H. Yang, and G.N. Parsons, *Surface Science*, **496**, 307 (2002).
- [25] R. Dewarrat and J. Robertson, *Journal of Non-Crystalline Solids*, **299-302**, 48 (2002).

- [26] A. von Keudell and J.R. Abelson, *Physical Review B*, **59**, 5791 (1999).
- [27] W.M. Tong and R.S. Williams, *Annual Review of Physical Chemistry*, **45**, 401 (1994).
- [28] F. Family and T. Vicsek, *Journal of Physics A*, **18**, L75 (1985).
- [29] M. Lutt, J.P. Schlomka, M. Tolan, J. Stettner, O.H. Seeck, and W. Press, *Physical Review B-Condensed Matter*, **56**, 4085 (1997).
- [30] S.K. Sinha, E.B. Sirota, S. Garoff, and H.B. Stanley, *Physical Review B*, **38**, 2297 (1988).
- [31] H. You, R.P. Chiarello, H.K. Kim, and K.G. Vandervoort, *Physical Review Letters*, **70**, 2900 (1993).
- [32] C. Herring, *Journal of Applied Physics*, **21**, 301 (1950).
- [33] M. Kardar, G. Parisi, and Y.C. Zhang, *Physical Review Letters*, **56**, 889 (1986).
- [34] P. Meakin, *Fractals, scaling and growth far from equilibrium*. (Cambridge UP, Cambridge, 1998).
- [35] A.I. Oliva, J.L. Sacedon, E. Anguiano, M. Aguilar, J.A. Aznarez, and J.A. Mendez, *Surface Science*, **417**, L1139 (1998).
- [36] M. Aguilar, E. Anguiano, and M. Pancorbo, *Journal of Microscopy*, **172**, 233 (1993).
- [37] S.J. Fang, S. Haplepete, W. Chen, C.R. Helms, and H. Edwards, *Journal of Applied Physics*, **82**, 5891 (1997).
- [38] W.U. Schmidt, R.C. Alkire, and A.A. Gewirth, *Journal of the Electrochemical Society*, **143**, 3122 (1996).
- [39] A.L. Barabasi and H.E. Stanley, *Fractal Concepts in Surface Growth* (Cambridge UP, Cambridge, 1995).

[40] D.M. Tanenbaum, A.L. Laracuente, and A. Gallagher, *Physical Review B-Condensed Matter*, **56**, 4243 (1997).

[41] M. Kondo, T. Ohe, K. Saito, T. Nishimiya, and A. Matsuda, *Journal of Non-Crystalline Solids*, **227-230**, 890 (1998).

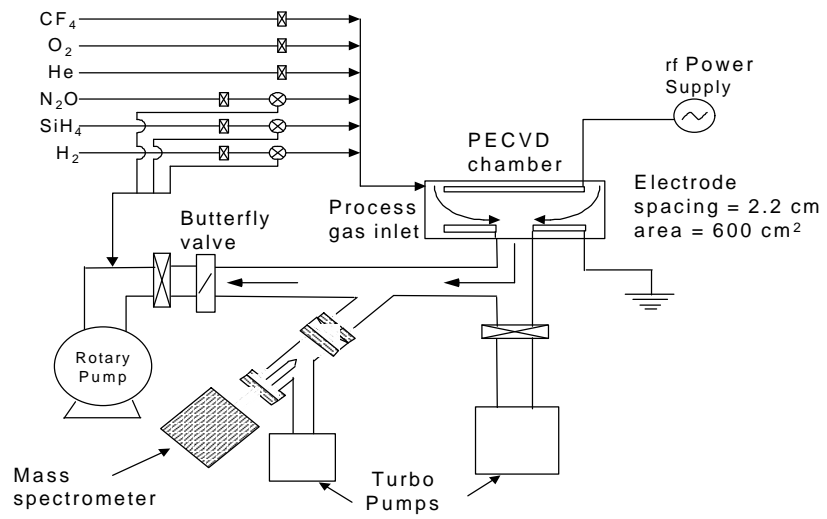


Fig. 1.1: Radial gas flow PECVD reactor schematic.

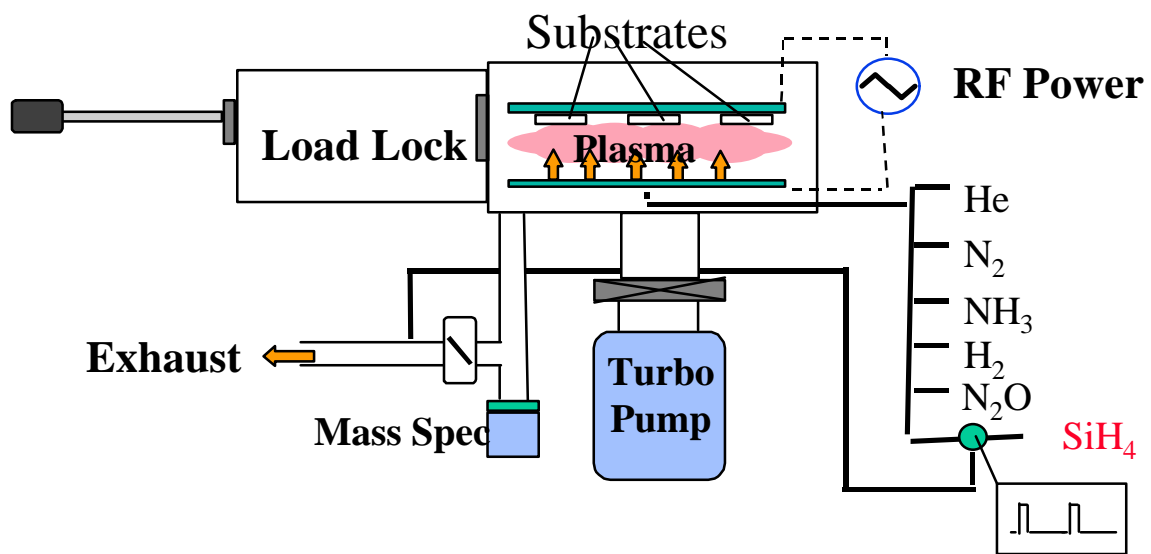


Fig. 1.2: Large area PECVD reactor schematic.

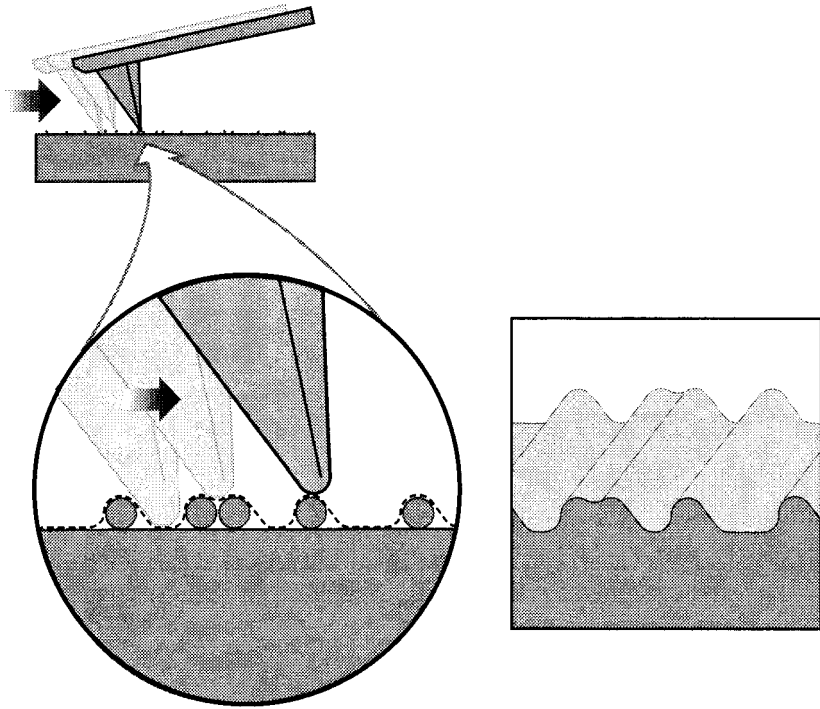


Fig. 1.3: Effect of tip radius on resolution of features in AFM.

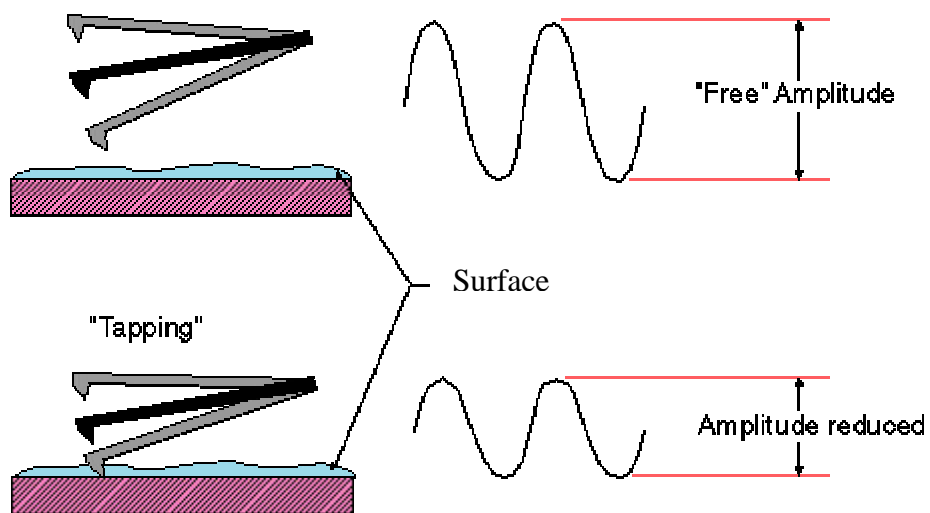


Fig 1.4: Schematic of how AFM determines surface topography during tapping mode.

*Chapter 2 is a reprint of a manuscript published in Physical Review B 65(3) 035311, 2002.*

## **CHAPTER 2**

# **2 SURFACE TRANSPORT KINETICS IN LOW TEMPERATURE SILICON DEPOSITION DETERMINED FROM TOPOGRAPHY EVOLUTION**

by: Kevin R. Bray and Gregory N. Parsons

*Department of Chemical Engineering, North Carolina State University, Raleigh, NC 27695-7905*

### **ABSTRACT**

In this article, surface transport kinetics during low temperature silicon thin film deposition are characterized using time dependent surface topography and dynamic scaling models. Analysis of surface morphology indicates that diffusion of adsorbed species dominates surface transport, with a characteristic diffusion length that increases with surface temperature. A diffusion activation barrier of  $\sim 0.2\text{eV}$  is obtained, consistent

with hydrogen-mediated adspecies diffusion on the growth silicon surface. Samples are compared over a range of deposition temperatures (25 to 350°C) and film thickness (20 to 5000 Å) deposited using silane with helium or argon dilution, on glass and silicon substrates. Self-similar surface structure is found to depend on detailed film growth conditions, but is independent of film thickness after nuclei coalescence. For films deposited using helium dilution, static and dynamic scaling parameters are consistent with self-similar fractal geometry scaling, and the lateral correlation length increases from 45 nm to 150 nm as temperature increases from 25 to 150°C. These results are discussed in relation to current silicon deposition models and with topography evolution observed during low temperature growth of other amorphous material systems.

## 2.1 INTRODUCTION

A current challenge in low temperature thin film deposition is to understand kinetics of surface processes to control surface reactions and improve material properties. Growth models based on thermodynamic balances only strictly apply in the equilibrium limit, where mass transport on the surface is fast relative to the arrival of depositing species. This limit is impractical for current technologically relevant processes where high deposition rates, smooth surfaces, limited disruption of substrate materials (i.e. dopant profiles, polymer structure, bond structure and composition, etc.), and controlled reactivity at the surface are critically important. The technological need for lower deposition temperatures requires that the deposition procedure be maintained far from equilibrium, where kinetic rate processes dominate surface mechanisms. Therefore, understanding thermally activated elementary process steps is particularly important to describe film growth, and kinetic processes have received significant attention theoretically and experimentally over the past several years [1-6].

Hydrogenated amorphous silicon can be deposited by a variety of low temperature techniques, including plasma enhanced chemical vapor deposition, reactive sputtering, and hot wire chemical vapor deposition. Mechanisms in a-Si:H deposition continue to receive attention because of the push to improve material defect density and stability for commercial applications, including solar cells and thin film transistor devices. Also, hydrogenated amorphous silicon is a good model system to understand activated low temperature deposition processes because the process proceeds from a single precursor (silane) in commonly available direct rf plasma deposition tools.

Plasma deposition of hydrogenated amorphous silicon results in very smooth, conformal surfaces and non-thermally activated growth rates over temperatures ranging from  $<25^{\circ}$  to  $400^{\circ}\text{C}$ . Typical models for a-Si:H growth presume that radical precursors generated in the gas phase adsorb and diffuse on the surface with low thermal barriers, giving rise to the observed smooth conformal surface coverage [4-6]. Surface transport parameters are typically characterized by comparing experimental macroscopic parameters (such as growth rate or step coverage) with precursor dependent reaction models [7, 8], or are estimated through simulations [4, 6, 9-11]. To date, results directly identifying surface transport kinetic processes in low temperature silicon growth are not available. The technique for surface transport analysis presented and utilized here employs direct surface characterization, and does not require identification or supposition of the particular gas-phase precursor responsible for growth, or the adsorbed surface species responsible for diffusion.

Results presented below demonstrate that silicon surface transport during low temperature plasma deposition is dominated by thermally activated adspecies diffusion, with an activation barrier of 0.2eV. The diffusion barrier is an important parameter for kinetic growth models for silicon, and this work presents a unique direct experimental characterization of this parameter. The basic approach used here has been used previously to characterize surface diffusion during physical vapor deposition of glassy metals [12]. This article addresses limitations and requirements for applying this method to analysis of silicon deposition, and demonstrates differences between deposition of hydrogenated silicon and other materials.

## 2.2 DYNAMIC SCALING, AND DEFINITION OF SURFACE SCALING PARAMETERS

### 2.2.1 Characterization of Surface Morphology

Surface morphology of deposited films, determined using scanning electron microscopy, scanning probe microscopy, or small angle X-ray scattering techniques, is typically analyzed using a height-height correlation function:

$$C(\mathbf{R}) = \langle z(\mathbf{r})z(\mathbf{r} + \mathbf{R}) \rangle_{\mathbf{r},\mathbf{R}} \quad (1)$$

or a height-difference correlation function:

$$G(\mathbf{R}) = \langle [z(\mathbf{r}) - z(\mathbf{r} + \mathbf{R})]^2 \rangle_{\mathbf{r},\mathbf{R}} \quad (2)$$

where  $z(\mathbf{r})$  is the height at any point  $\mathbf{r}$  on the surface and  $\langle \rangle_{\mathbf{r},\mathbf{R}}$  refers to the average over all pairs of surface points separated by a distance  $\mathbf{R}$ . The data is then compressed and displayed in terms of a power spectral density function:

$$g(|\mathbf{q}|) = F[C(|\mathbf{r}|)] \quad (3)$$

where  $F$  is the two-dimensional Fourier transform operator. Early models used Gaussian or modified Gaussian functions to describe and predict surface correlation functions [3], which allowed the surface structure to be described by a minimal set of parameters including the standard deviation of the surface height, and the lateral correlation length. Later models utilized concepts of topographical scaling, where surface self-affinity or surface self-similarity is used to describe growing surfaces [1]. A surface that follows fractal growth is self-affine, indicating a correlation between roughness amplitude and lateral scale. Self-similarity is a special case of self-affinity, where the roughness

exhibits isotropic scaling [2] with a constant ratio between the vertical and lateral components, independent of lateral scale. The distinction between self-affinity and self-similarity is shown schematically in Figure 2.1. The height-difference correlation function can also be written in terms of a scaling function,  $f(R/L_c)$ :

$$G(R) = 2\sigma^2 f(R/L_c) \quad (4)$$

where  $\sigma$  is the root mean square roughness of the surface, and  $L_c$  is the maximum lateral length scale over which surface roughness correlations persist [3]. The scaling function has an asymptotic form  $f(x) = (R/L_c)^{2\alpha}$  for  $x < 1$ , and  $f(x) = 1$  for  $x > 1$ , where  $\alpha$  is the static scaling coefficient (or Hurst parameter). Values for the static scaling coefficient range from 0 – 1, with  $\alpha$  approaching 0 for jagged surfaces and 1 for smooth surfaces [13]. For the dynamic scaling hypothesis proposed by Sinha et.al. [14], the height-height correlation function is written as an exponential:

$$C(R) = \sigma^2 \exp[-(R/L_c)^{2\alpha}] \quad (5)$$

Dynamic scaling also predicts that for a self-affine surface, the root-mean-square (rms) roughness of the surface scales as:

$$\sigma \sim R^\alpha f(t^\beta/R^\alpha) \quad (6)$$

where  $t$  is the deposition time (proportional to film thickness) and  $\beta$  is the dynamic or temporal scaling exponent [3, 15]. When the argument of function  $f$  is much less than 1, then  $f$  approaches  $t^\beta/R^\alpha$  and when the argument is greater than 1,  $f$  is constant. This indicates that the rms roughness will be a function of the length scale ( $R$ ) used for the analysis until the roughness value saturates at a constant value ( $\sigma_{\text{sat}}$ ) for large lengths. For a self-affine surface, a log-log plot of  $\sigma$  vs.  $R$  will yield a straight line with slope

between 0 and 1 for  $R < L_c$ . For the more restricted case of a self-similar surface, the same functional form holds with  $\alpha=1$ .

The Fourier transform of the dynamic scaling autocorrelation function results in the spectral density function:  $g(|\mathbf{q}|) = [\alpha\sigma^2 L_c^2/\pi]$  for  $|\mathbf{q}| < 1/L_c$ , and  $g(|\mathbf{q}|) = [\alpha\sigma^2/L_c^{2\alpha}\pi]q^{-2(\alpha+1)}$  for  $|\mathbf{q}| > 1/L_c$ . The quantity  $i = 2(\alpha+1)$  is the Fourier index, and will have a value between 0 and 4 for a self-affine surface, and will be  $\sim 4$  when the surface is self-similar. For growth on a two-dimensional surface, the static scaling exponent and the Fourier index are related through the fractal dimension [3, 16],  $D_f = (8 - i)/2$ , which is also related to  $\alpha$  by  $D_f = (3 - \alpha)$ .

Surface kinetic models describe the balance between random arrival of species from the gas phase and a variety of thermally activated processes that operate on the surface. For growth of thin films from the vapor phase, if the species responsible for film deposition are randomly incorporated into the surface without appreciable surface transport, then stochastic, or random, surface growth will result in a rough surface. In the early 1950s, Herring described four distinct surface transport mechanisms that reduce surface roughness: i) viscous flow; ii) evaporation-condensation; iii) bulk diffusion and iv) surface diffusion [17]. The relationship between the surface topography and the surface transport mechanism comes from an analysis of the time and amount of material needed to produce a geometrically similar change in two different sized clusters using each mechanism. These mechanisms leave distinct imprints on the topography that are recognizable through fractal analyses. In 1986, Kardar, Parisi and Zhang described the development of surface roughness based on symmetry arguments [18]. Later models related the symmetry models to transport processes using equations of motion with terms

corresponding to specific surface smoothing or roughening mechanisms [3]. Continuum models including linear and non-linear terms in the equations of motion are used to analyze surface roughness data to determine scaling coefficients under different conditions. Matching the experimentally determined scaling exponents with continuum growth models then identifies the primary transport mechanisms.

## 2.2.2 Determination of Scaling Parameters

Both the static scaling coefficient,  $\alpha$ , and the dynamic scaling coefficient,  $\beta$ , are needed to distinguish surface transport mechanisms uniquely. Two methods, dimensional and frequency analysis are used to analyze topography data. Dimensional analysis involves determining rms surface roughness at various length scales ( $L$ ) and deposition times ( $t$ ), then obtaining scaling coefficients [3, 19] using  $\sigma \sim L^\alpha$  and  $\sigma_{\text{sat}} \sim t^\beta$ . Frequency analysis utilizes the Fourier transform of the surface topography [16, 20] to obtain the power spectral density (PSD). The one dimensional PSD is obtained by using the radius in reciprocal space as the spatial frequency and radially averaging the two dimensional spectrum [21]. The Fourier index is determined from the PSD using the power law relationship  $\text{PSD} \sim q^{-i}$  for wavenumbers  $q$  greater than a critical frequency,  $q_c$  (inverse of the critical length,  $q_c=1/L_c$ ), and  $\alpha$  is determined directly from  $i$ . Radial averaging generally gives a better correlation with fractal dimension than linear averaging.

For the linear continuum model with surface transport dominated by surface diffusion, the scaling coefficients are expected to attain values of  $\alpha = 1$  and  $\beta = 0.25$  [2, 3, 22]. When nonlinear terms are included, scaling coefficients of  $\alpha = 0.67$  and  $\beta = 0.2$

are expected for diffusion [2]. For transport by evaporation and condensation [3], expected values are  $\alpha = 0$  and  $\beta = 0$ . There are several reports analyzing kinetic smoothing mechanisms of hydrogenated amorphous silicon deposited using plasma deposition [23, 24] and thermal evaporation [25]. Typically,  $\alpha$  is measured between 0.8 – 1 and  $\beta$  between 0.2 – 0.33, consistent with self-similar geometry and transport by surface diffusion. As expected, these values are distinctly different from parameters typically reported for evaporated metal surfaces. Static scaling coefficients are typically  $\sim 0.7$ - $0.8$  with  $\alpha = 0.82$  for Ag and  $\alpha = 0.68$  for Pt [22], which are consistent with values reported for surface diffusion and step growth [3, 22], i.e.  $\alpha = 0.67$  and  $\beta = 0.2$ .

## **2.3 EXPERIMENTAL METHOD**

### **2.3.1 Hydrogenated Amorphous Silicon Deposition**

To analyze silicon deposition processes, films were deposited using an rf (13.56 MHz) parallel plate plasma deposition system with circular geometry (diameter=28cm) and radial gas flow. Deposition temperature ranged from 25 to 150°C, and film thickness was varied from 20 to 5000Å. Film thickness was determined by step-height profilometry for films  $>100\text{Å}$ , and from the extrapolated growth rate for thinner films. Growth rate was linear for all conditions. Silane gas, diluted to 2% with He and/or Ar, was used for the depositions, and the total gas flow rate was fixed at 100 standard cubic centimeters per minute (sccm). The process pressure was fixed at 0.6 Torr, and the rf power was  $8\text{mW}/\text{cm}^2$ . Using  $\text{SiH}_4/\text{He}$  gas mixtures, the deposition rate was

~50Å/minute, and slower rates (~22Å/min) were observed using SiH<sub>4</sub>/Ar mixtures. Substrates included clean Si(100) and 7059 glass.

### 2.3.2 Topography Analysis

Atomic force microscopy (AFM) for surface topography analysis was conducted using a Digital Instruments Dimension 3000, with a Nanoscope IIIa controller and vibration-shielded hood. Imaging was performed in intermittent contact mode, using c-Si cantilever probes with a nominal tip radius of 5 – 10 nm. Image analysis was performed using built-in software functions to calculate the root-mean-square (rms) roughness,  $\sigma$ , and the power spectral density (PSD) spectrum. The rms roughness is computed using the function:

$$\sigma = [\sum (Z_i - Z_{ave})^2 / N]^{1/2} \quad (7)$$

where  $Z_{ave}$  is the average height in a given area,  $Z_i$  is the height of a given point, and N is the number of points in the area. The PSD is calculated from an algorithm that is based on radially averaging the two dimensional Fast Fourier Transform of the image. Scan sizes of 200 x 200nm<sup>2</sup>, 500 x 500nm<sup>2</sup>, and 1 x 1µm<sup>2</sup> were measured to insure there were no artificial effects introduced into the analysis from the scan size. The probe tip was changed as needed to maintain good images.

All AFM measurements were performed under ambient conditions. An important consideration is the effect of probe tip size and geometry, and surface ambient exposure, on surface topography results. To address this question, a 480nm thick a-Si film deposited at 350°C and previously characterized using STM directly connected to a

plasma deposition reactor [26] was analyzed in ambient in our lab using AFM. Using the same range of scan sizes (50 to 250nm), the radially averaged Fourier transform of the on-line STM measurement showed a slope of  $\sim 1.2$ , and the AFM measurement produced a slope of 1.2 – 1.3, indicating that ambient exposure does not significantly affect surface topography over the height and length scales analyzed. The AFM analysis was able to extend to scan sizes greater than 1  $\mu\text{m}$  which enabled a greater range of frequencies for analyzing the power spectrum. The AFM will generally have a larger tip radius than the STM, which will allow the STM to better access topography data over short (<10nm) length scales. However, for the dimensional analysis, the smallest roughness calculations performed used length scales exceeding 20nm, which is larger than twice the nominal AFM tip radius. Therefore, for the length scales of interest, ambient AFM and on-line STM techniques give reasonably similar results, and the AFM images are sufficient to extract useful topography data and surface scaling parameters.

## **2.4 RESULTS AND DISCUSSION**

### **2.4.1 Frequency and Dimensional Analysis to Characterize Fractal Scaling**

Extraction of surface scaling parameters from the fractal dimension requires that the surface structure follow fractal geometry scaling. Therefore, we first demonstrate that self-similar surface scaling can be achieved over a wide range of process conditions (but not all conditions) for a-Si:H deposition. Also, for demonstration and experiment control, the amorphous silicon surface is compared to an evaporated aluminum surface,

which is expected to exhibit substantially different surface topography and scaling. Topography is analyzed using both frequency and dimensional analysis.

Figure 2.2 shows the power spectral density used for frequency analysis for two samples: sample (a) is a 1000 Å a-Si:H deposited using a silane plasma diluted with helium, and sample (b) is a 1.5µm thick evaporated aluminum film. For both surfaces, the PSD has an almost constant value in the low frequency range. This relates to large real space features and a substantial change in roughness is not expected on that scale. Above the critical frequency ( $q_c=0.01\text{nm}^{-1}$  for Si and  $0.003\text{nm}^{-1}$  for Al in the spectra shown), the PSD decreases exponentially on the log-log plot with a  $1/q^i$  dependence with  $i = 4.1$  for a-Si and  $i = 3.5$  for the Al surface.

For dimensional analysis, the static scaling exponent is determined for the same Si and Al surfaces from the plot shown in Fig. 2.3(a). The plot of rms surface roughness vs. measurement length gives a linear slope of  $\alpha$  up to the critical length [3, 22],  $L_c$ , and the roughness saturates at  $\sigma_{\text{sat}}$  for large lengths. The a-Si film shows a value of  $\alpha = 1.03$ , consistent with self-similar scaling, and the Al film has a value of  $\alpha = 0.77$ , which is in the expected range for evaporated metals [22]. The data in Figure 2.3(a) indicate critical lengths for these a-Si and Al samples are  $L_c = 75\text{nm}$  and  $330\text{nm}$ , respectively.

Generally for silicon films deposited using  $\text{SiH}_4/\text{He}$  mixtures, including the films shown in Figures 2.2 and 2.3, dimensional analyses result in values that saturate at  $\alpha \approx 1$ , and frequency analyses result in Fourier index  $i \approx 4$ . These values are both consistent with self-similar scaling geometry in the surface morphology of deposited silicon films. As will be shown below, deposition using argon dilution disrupts the self-similar scaling geometry.

## 2.4.2 Effect of Thickness and Gas Composition on Scaling Coefficients

The surface topography was examined for silicon plasma deposition as a function of temperature, film thickness, and diluent gas species. Specifically, static scaling coefficient values were extracted using dimensional analysis for silicon deposited from SiH<sub>4</sub>/He and SiH<sub>4</sub>/Ar mixtures on crystalline silicon substrates for various deposition times. The static scaling coefficient was observed to increase during the initial growth (corresponding to film nucleation and coalescence, as shown below), then saturate at  $\alpha=1.09 \pm 0.05$  for He dilution and  $\alpha=0.63 \pm 0.01$  for Ar dilution. The smaller saturation value for Ar diluted silane indicates a distinctly different (non-self-similar) surface topography for the Ar diluted process. This difference in surface topography between Ar and He dilution is presumably due to the larger energy transfer during Ar ion bombardment. For comparison, Fourier index values are determined from frequency analysis for a-Si:H films deposited from SiH<sub>4</sub>/He. The values for  $i$  are constant with  $i = 4.1 \pm 0.3$  for deposition times from 1 to over 30 minutes, corresponding to thicknesses greater than 1500Å. Using the relationship between  $\alpha$  and  $i$ , the Fourier index obtained from frequency analysis corresponds to  $\alpha = 1.05$ , which is consistent with  $\alpha$  obtained using dimensional analysis on the same set of films. This result further supports the self-similar structure of the growing a-Si:H surface. Thicker films have also been measured and indicate that self-similar behavior extends to film thickness at least as large as 5000Å.

For films grown with helium dilution at 25°C and 100°C, the dynamic scaling exponent,  $\beta$ , is determined from the slope of  $\sigma_{\text{sat}}$  plotted vs. deposition time shown in Fig.

2.4. For short deposition times, the surface roughness values are not expected to follow the scaling trend because the silicon nuclei have not completely coalesced. A least squares fit to the points for deposition  $\geq 1$  minute results in  $\beta = 0.26 \pm 0.13$ . For this self-affine surface, the coefficients of  $i \approx 4$ ,  $\alpha \approx 1$  and  $\beta \approx 0.25$  are consistent with surface transport dominated by adatom diffusion [2, 3, 22]. Further support for surface diffusion is obtained from analysis of nuclei coalescence in the initial stages of film growth.

### 2.4.3 Silicon Nucleation and Film Coalescence

Film coalescence can be directly observed using AFM analysis and related to observed trends in the static scaling coefficient. Figure 2.5 shows AFM images for films deposited for 30 seconds at (a) 25 and (b) 100°C. The nuclei in the 25°C film are small (17nm) and jagged, whereas the 100°C film exhibits larger (45nm), rounder nuclei. Note that the vertical scale for sample (b) is 10x larger than sample (a). The static scaling coefficient for the image in Fig. 2.5(a) is  $\sim 0.25$ , similar to that measured for the clean substrate. The film deposited at 100°C in Fig. 2.5(b) has  $\alpha = 0.8$ , close to  $\alpha \approx 1$  observed for thicker films. The AFM images and roughness analysis indicate the nuclei are not yet coalesced at low temperature, but they have begun to coalesce at higher temperature. At longer deposition times, AFM images in Figure 2.6 indicate complete coalescence, and films show surface morphology independent of substrate temperature, consistent with the constant scaling coefficient observed.

Figure 2.3(b) shows the rms roughness vs. length scale for a-Si films deposited from SiH<sub>4</sub>/He mixtures on silicon substrates, for deposition times ranging from 10 to

~1200s. The slope of the curves,  $\alpha$ , are small for short deposition time (similar to values measured for the clean silicon substrate) and increase and saturate for longer times. Values for  $\alpha$  determined from data in Fig. 2.3(b) and from other films deposited at various temperatures on silicon and glass substrates are plotted versus deposition time in Fig. 2.7. The value for  $\alpha$  increases with deposition time then saturates near  $\alpha=1$ . The transition from the initial  $\alpha$  value to the saturated value corresponds to nuclei coalescence observed in the AFM images, and the horizontal arrows in Figure 2.7(a) indicate the range of coalescence times determined from AFM. The time required to reach saturation decreases with increasing temperature, indicating that films coalesce more rapidly at higher temperature, consistent with thermally activated surface diffusion. A plot of the inverse inflection time vs.  $1/T$  gives an activation energy of  $\sim 0.07\text{eV}$  for films deposited on silicon. The data in Figure 2.7(b) shows that nucleation and coalescence occurs at a slower rate on glass than on clean silicon substrates.

A summary of scaling parameters (from dimensional and frequency analysis), coalescence times, and correlation lengths, obtained from silicon films deposited using various source gases, substrates, and substrate temperatures is given in Table 2.1.

#### **2.4.4 Effect of Temperature on Surface Transport During Silicon Deposition**

Figure 2.3(c) shows the rms roughness vs. length scale for  $1000\text{\AA}$  thick a-Si:H films deposited from silane/helium mixtures at various temperatures. Over the range studied, the slope  $\alpha = 1.09 \pm 0.05$  and is independent of temperature. However, as temperature increases, the saturation roughness decreases, and the correlation length,  $L_c$ ,

is observed to increase. The correlation length is a good estimate of the surface diffusion length [4, 23] and has been used to evaluate activation barriers for surface diffusion for glassy metals formed by physical vapor deposition [12]. The surface diffusion coefficient is proportional to the square of the diffusion length. Figure 2.8 shows an Arrhenius plot of  $\ln(L_c^2)$ , determined from the data in Fig. 2.3(c). The data shows a good fit to a straight line and the slope indicates an activation energy of  $E_a = 0.20 \pm 0.02\text{eV}$ . Therefore, the data in Figures 2.3, 2.4, 2.7 and 2.8 are consistent with surface transport in a-Si:H deposition being dominated by adspecies diffusion with an activation barrier of 0.2eV. Other indirect estimates of surface diffusion activation barriers during a-Si:H growth [4, 6, 7, 9-11] are typically in the range of 0.16 to 0.3eV. The value we obtain is within this range, but it is important to note that the approach used here involves direct evaluation of deposited surfaces using a model of surface topography evolution not previously used to characterize surface transport kinetics in silicon growth.

Surface diffusion barriers determined from analysis of glassy metal surfaces formed by physical vapor deposition are significantly larger than that found here for silicon deposition. The smaller barrier in our analysis is consistent with a hydrogen-mediated precursor diffusion process. Diffusion on a clean glassy metal surface requires direct metallic bond-breaking and reforming, so a barrier close to the bond enthalpy is expected. For hydrogenated silicon growth, barriers less than the bond enthalpy are expected due to the reduction of surface energy by bonded surface hydrogen. Silyl precursor adsorption on hydrogenated silicon surfaces is typically believed [4-6] to involve formation of a surface three-center bond ( $\text{Si-H-SiH}_3$ ), where diffusion proceeds through motion of the physisorbed  $\text{SiH}_3$  between Si-H sites. A relatively weak three-

center bond structure is presumed, consistent with a small diffusion activation barrier. However, recent calculations of SiH<sub>3</sub>/Si-H surface interactions [27] indicate that the three-center bond does not have a state sufficiently stable to account for observed diffusion processes. Another possible picture, also consistent with a relatively small diffusion activation energy, is that silyl radicals adsorb onto silicon sites and diffuse through Si-Si bond breaking and reforming, where bond breaking is facilitated by H insertion into the (weaker) stretched Si-Si bond, and Si-Si bond formation is accompanied by molecular hydrogen formation and release. Other elemental adsorption and diffusion steps could also be considered that are also consistent with the observed results.

## 2.5 SUMMARY AND CONCLUSION

Fractal analyses, including dimensional and frequency methods, have been used to evaluate surface morphology of plasma deposited hydrogenated amorphous silicon surfaces formed under various deposition conditions. Using SiH<sub>4</sub>/He mixtures, surface transport is dominated by surface diffusion, with a characteristic diffusion length that increases with surface temperature. Diffusion kinetics are consistent with a diffusion activation barrier of ~0.2eV and with values estimated previously by other approaches. The coalescence of deposited film nuclei on the substrate surface is identified from the evolution of the static scaling coefficient. After initial nuclei coalescence, the surface topography of films formed from SiH<sub>4</sub>/He mixtures is consistent with a self-similar geometry, independent of film thickness. Results indicate that surface transport occurs

by diffusion of adsorbed surface species, and the lateral correlation length increases from 45 nm to 150 nm as temperature increases from 25 to 150°C. Argon dilution resulted in a more stochastic, rough surface, consistent with effects due to larger mass ion bombardment during deposition. The activation barrier of 0.2eV obtained for silicon surfaces is smaller than 0.5eV observed for diffusion on glassy metal surfaces, and is ascribed to effects of surface hydrogen in promoting diffusion of silicon adspecies. These results show that analysis of surface topography evolution can be used to obtain important surface kinetic parameters in the growth of silicon-based materials.

## **2.6 ACKNOWLEDGEMENTS**

This work was supported under NSF Grant No.'s 9624612 and 0072784. The authors also thank A. Flewitt and J. Robertson for helpful discussions and for sharing with us silicon samples and topological data.

## 2.7 REFERENCES

- [1] F. Family and T. Vicsek, *Journal of Physics A*, 18, L75 (1985).
- [2] A.L. Barabasi and H.E. Stanley, *Fractal Concepts in Surface Growth* (Cambridge UP, Cambridge, 1995).
- [3] W.M. Tong and R.S. Williams, *Annual Review of Physical Chemistry*, 45, 401 (1994).
- [4] J. Robertson, *Journal of Applied Physics*, 87, 2608 (2000).
- [5] J. Perrin, M. Shiratani, P. Kae-Nune, H. Videlot, J. Jolly, and J. Guillon, *Journal of Vacuum Science and Technology A*, 16, 278 (1998).
- [6] G. Ganguly and A. Matsuda, *Journal of Non-Crystalline Solids*, 164-166, 31 (1993).
- [7] K. Maeda, A. Kuroe, and I. Umezu, *Physical Review B*, 51, 10635 (1995).
- [8] A. Matsuda, *Thin Solid Films*, 337, 1 (1999).
- [9] M.J. Kushner, *Journal of Applied Physics*, 62, 4763 (1987).
- [10] K.K. Gleason, K.S. Wang, M.K. Chen, and J.A. Reimer, *Journal of Applied Physics*, 61, 2866 (1987).
- [11] R. Robertson and A. Gallagher, *Journal of Chemical Physics*, 85, 3623 (1986).
- [12] B. Reinker, M. Moske, and K. Samwer, *Physical Review B*, 56, 9887 (1997).
- [13] M. Lutt, J.P. Schlomka, M. Tolan, J. Stettner, O.H. Seeck, and W. Press, *Physical Review B*, 56, 4085 (1997).
- [14] S.K. Sinha, E.B. Sirota, S. Garoff, and H.B. Stanley, *Physical Review B*, 38, 2297 (1988).

- [15] H. You, R.P. Chiarello, H.K. Kim, and K.G. Vandervoort, *Physical Review Letters*, 70, 2900 (1993).
- [16] A.I. Oliva, J.L. Sacedon, E. Anguiano, M. Aguilar, J.A. Aznarez, and J.A. Mendez, *Surface Science*, 417, L1139 (1998).
- [17] C. Herring, *Journal of Applied Physics*, 21, 301 (1950).
- [18] M. Kardar, G. Parisi, and Y.C. Zhang, *Physical Review Letters*, 56, 889 (1986).
- [19] P. Meakin, *Fractals, scaling and growth far from equilibrium*. (Cambridge UP, Cambridge, 1998).
- [20] M. Aguilar, E. Anguiano, and M. Pancorbo, *Journal of Microscopy*, 172, 233 (1993).
- [21] S.J. Fang, S. Haplepete, W. Chen, C.R. Helms, and H. Edwards, *Journal of Applied Physics*, 82, 5891 (1997).
- [22] W.U. Schmidt, R.C. Alkire, and A.A. Gewirth, *Journal of the Electrochemical Society*, 143, 3122 (1996).
- [23] D.M. Tanenbaum, A.L. Laracuente, and A. Gallagher, *Physical Review B*, 56, 4243 (1997).
- [24] M. Kondo, T. Ohe, K. Saito, T. Nishimiya, and A. Matsuda, *Journal of Non-Crystalline Solids*, 227-230, 890 (1998).
- [25] H.-N. Yang, Y.-P. Zhao, G.-C. Wang, and T.-M. Lu, *Physical Review Letters*, 76, 3774 (1996).
- [26] A.J. Flewitt, J. Robertson, and W.I. Milne, *Journal of Applied Physics*, 85, 8032 (1999).
- [27] A. Gupta, H. Yang, and G.N. Parsons, *Surface Science*, 496, 307 (2002).

Film (source gas)	Substrate	Substrate Temp.	$\alpha$	Fourier Index	Coalescence Time (s)	Correlation Length (nm)	Self- similar?
None	c-Si	--	0.25		N/A	N/A	N
None	Corning 7059 glass	--	0.30		N/A	N/A	N
a-Si:H (SiH <sub>4</sub> /He)	c-Si	25°C	1.07	4.1	52	45	Y
		75°C	1.04	4.7		65	Y
		100°C	1.10	4.2	31	70	Y
		125°C	1.00	4.3		110	Y
		150°C	1.09	4	24	150	Y
a-Si:H (SiH <sub>4</sub> /He)	Corning 7059 glass	25°C	0.96	4.2	68	44	Y
		100°C	1.00	4.5	36	62	Y
a-Si:H (SiH <sub>4</sub> /Ar)	c-Si	25°C	0.63	5.1		80	N
Evaporated Al	Quartz	25°C	0.77	3.5		300	N

Table 2.1: Summary of scaling coefficients, coalescence time and correlation length for various source gas, substrates and substrate temperatures. The static scaling coefficient,  $\alpha$ , is determined from dimensional analysis, and Fourier index is obtained from frequency analysis.

N/A - Not Applicable

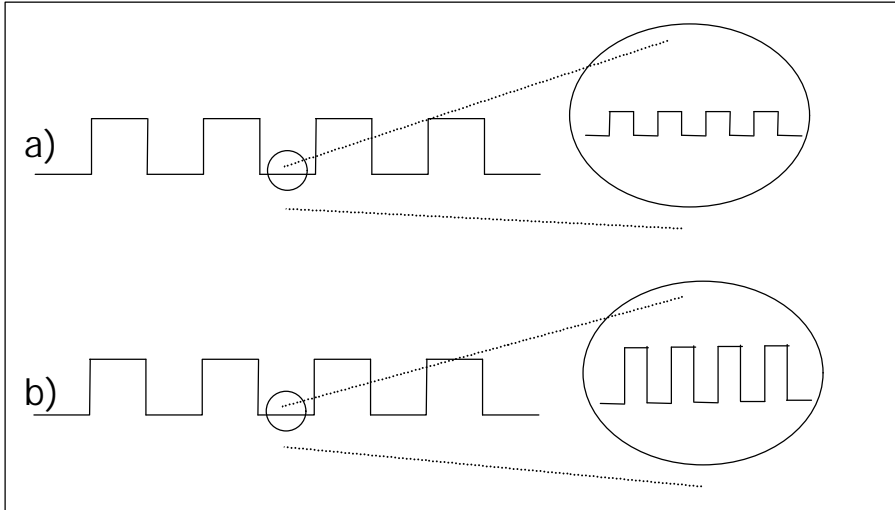


Fig. 2.1: Artificial self-similar and self-affine profiles. Isotropic magnification of a) self-similar and b) self-affine profiles are shown in the circles.

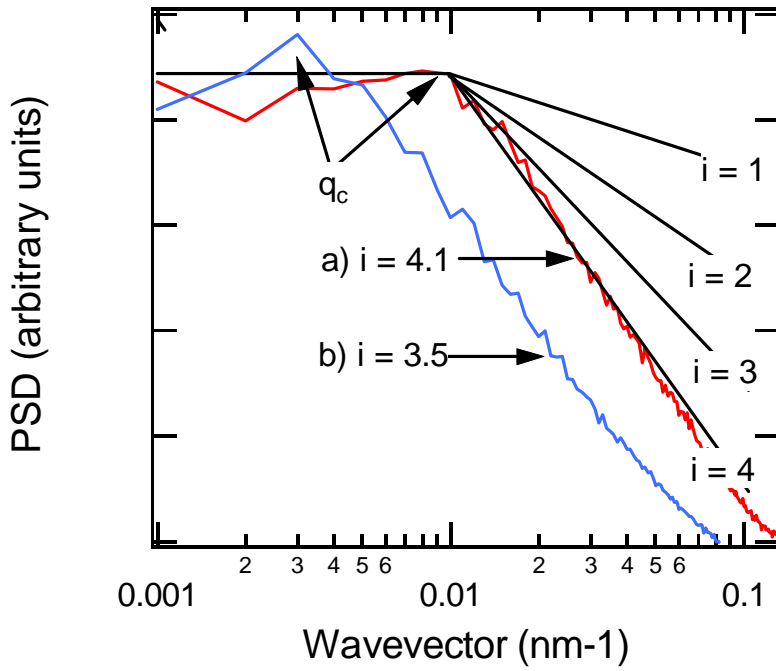


Fig. 2.2: Power spectral density plots for a) 1000 Å a-Si:H film deposited by plasma CVD from SiH<sub>4</sub>/He; and b) 1.5 μm Al deposited by evaporation. The spectrum is observed to decrease with a slope of  $i$ , the Fourier index, above the critical frequency  $q_c$ . The a-Si has a larger value for  $i$ , indicating surface diffusion is more prominent than in the evaporation process.

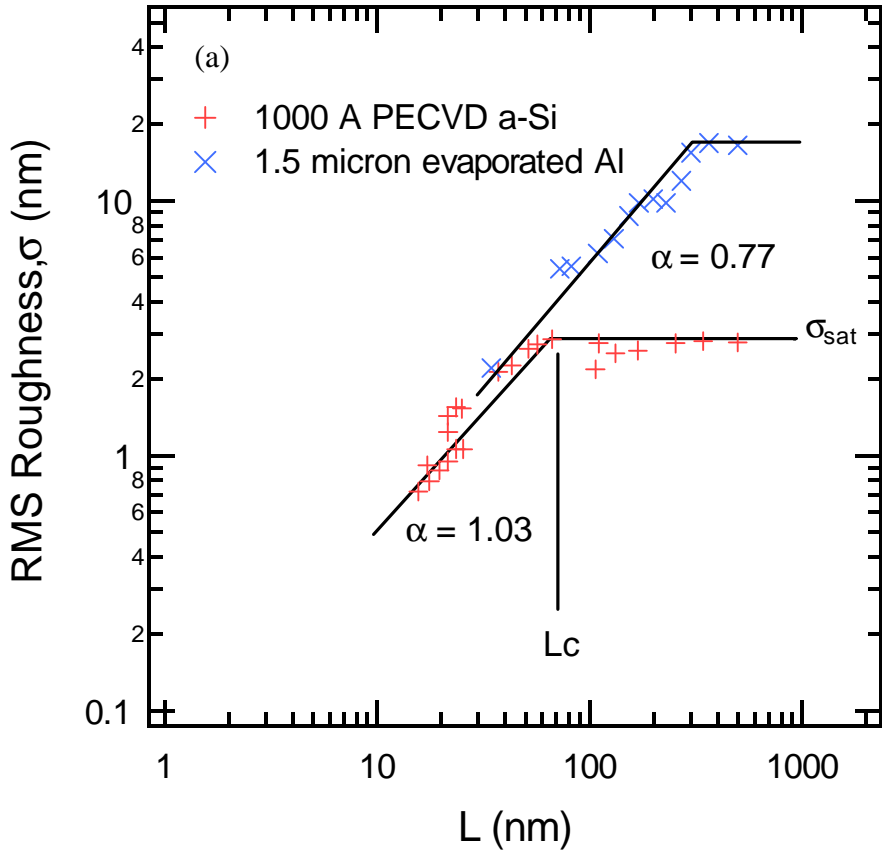


Fig. 2.3(a): RMS roughness vs. length scale. Comparison between PECVD a-Si:H and evaporated Al. Evaporated Al has a smaller  $\alpha$ , indicating it has a rougher surface than the plasma deposited a-Si. The roughness of the a-Si film saturates at a critical length,  $L_c$ , of 75 nm while the Al film has an  $L_c$  of 300 nm.

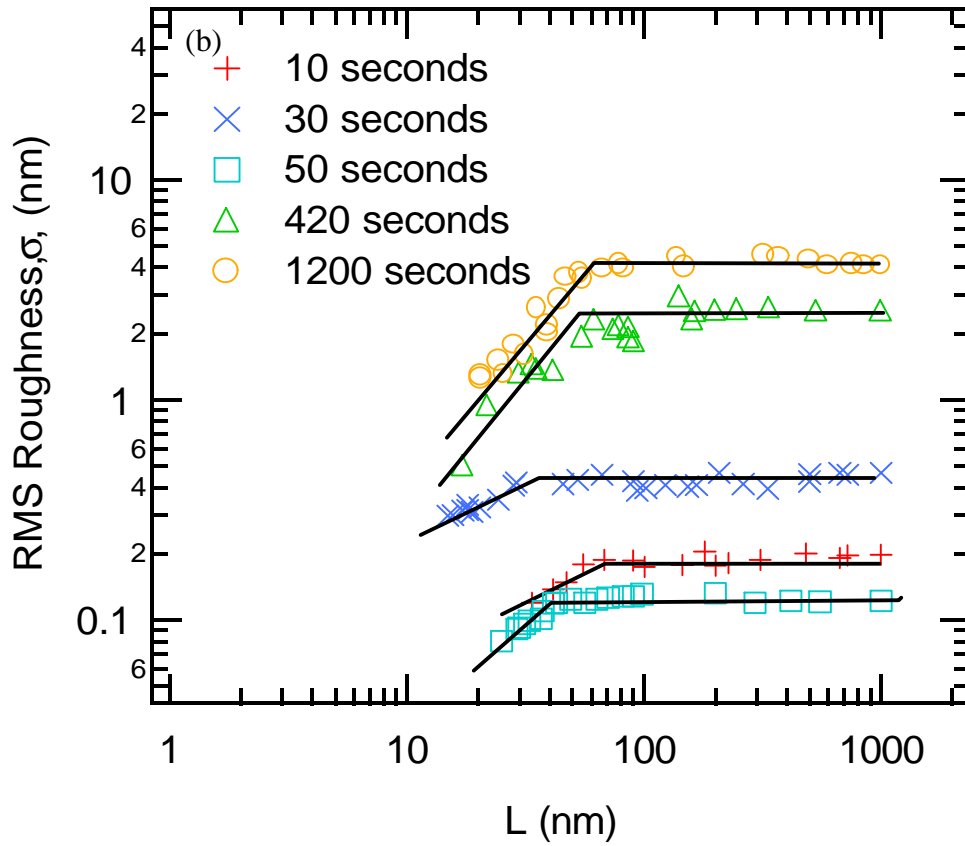


Fig. 2.3(b): RMS roughness vs. length scale. Comparison of deposition time for films deposited at 25°C. The static scaling coefficient  $\alpha$ , remains small for thin (non-coalesced) films, and then reaches a constant value for thick films.

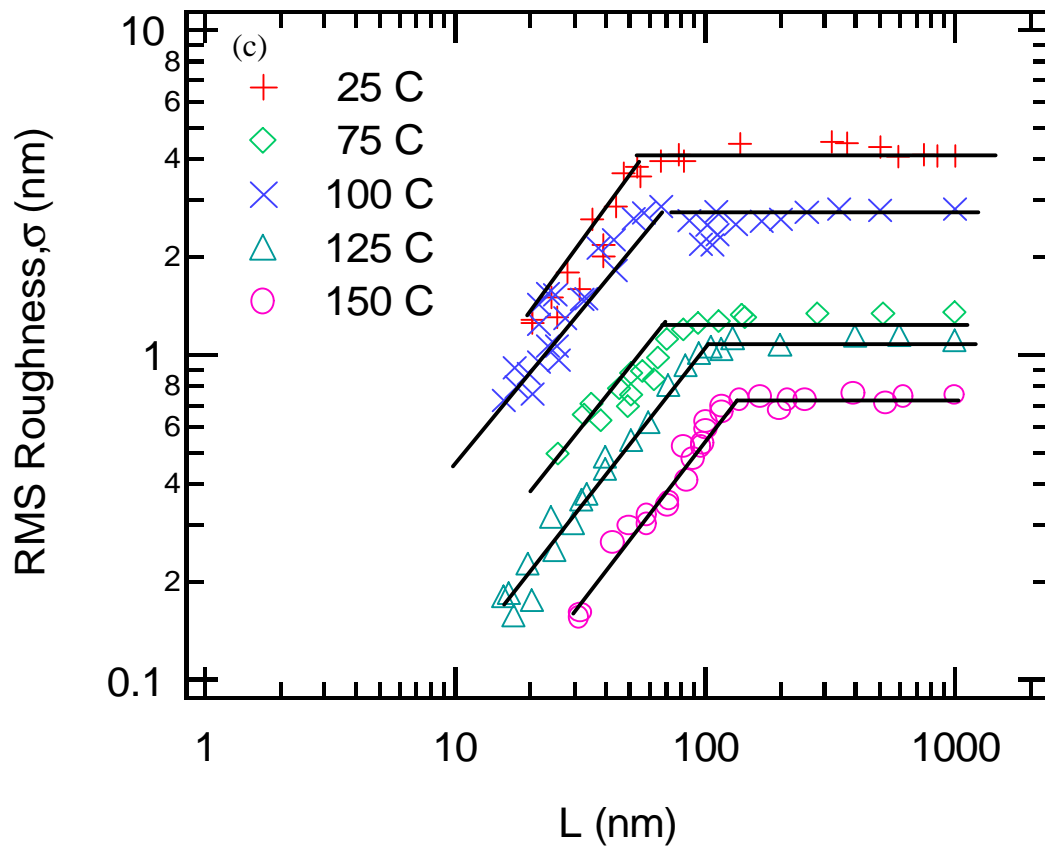


Fig. 2.3(c): RMS roughness vs. length scale. Comparison of substrate temperature for films deposited from a  $\text{SiH}_4/\text{He}$  mixture for 20 minutes.

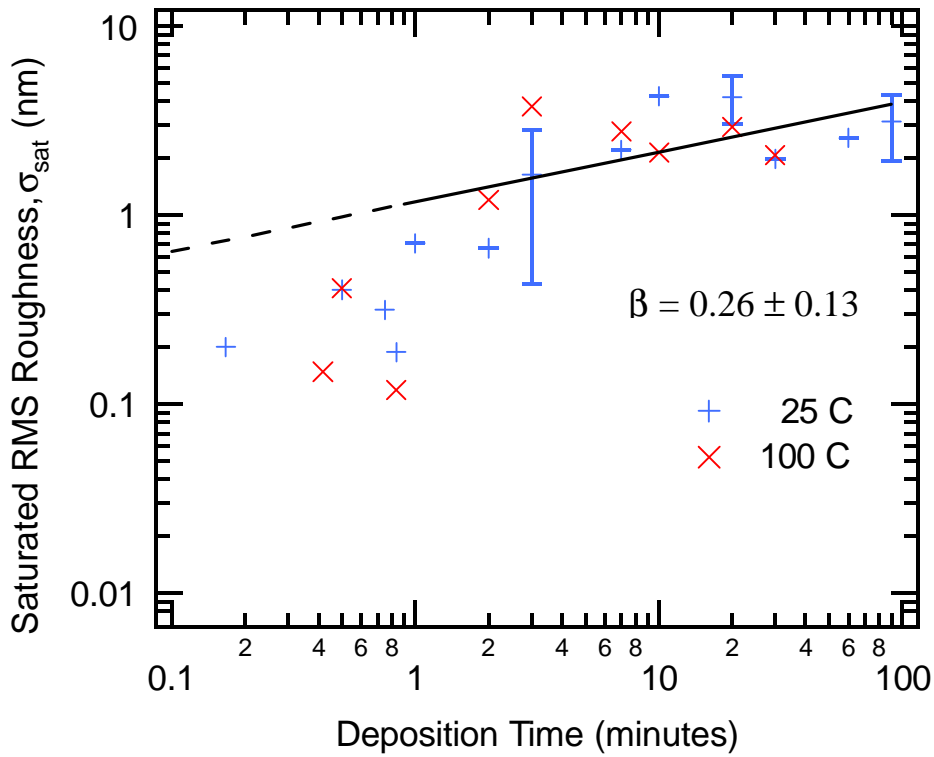


Fig. 2.4: Saturated RMS roughness (determined by dimensional analysis) vs. deposition time for silicon deposited from  $\text{SiH}_4/\text{He}$  mixtures on Si. The surface diffusion model indicates that  $\sigma$  should increase with time with a slope of  $\beta = 0.25$ . At times greater than one minute, a best fit of the roughness data yields  $\beta = 0.26 \pm 0.13$ . The error was determined from the quality of the least squares fit. The dashed line is an extension of the fit and does not represent a fit of the data in that region of the graph. The error bars are  $3\sigma$  values determined from  $>5$  measurements of multiple films deposited with the same conditions.

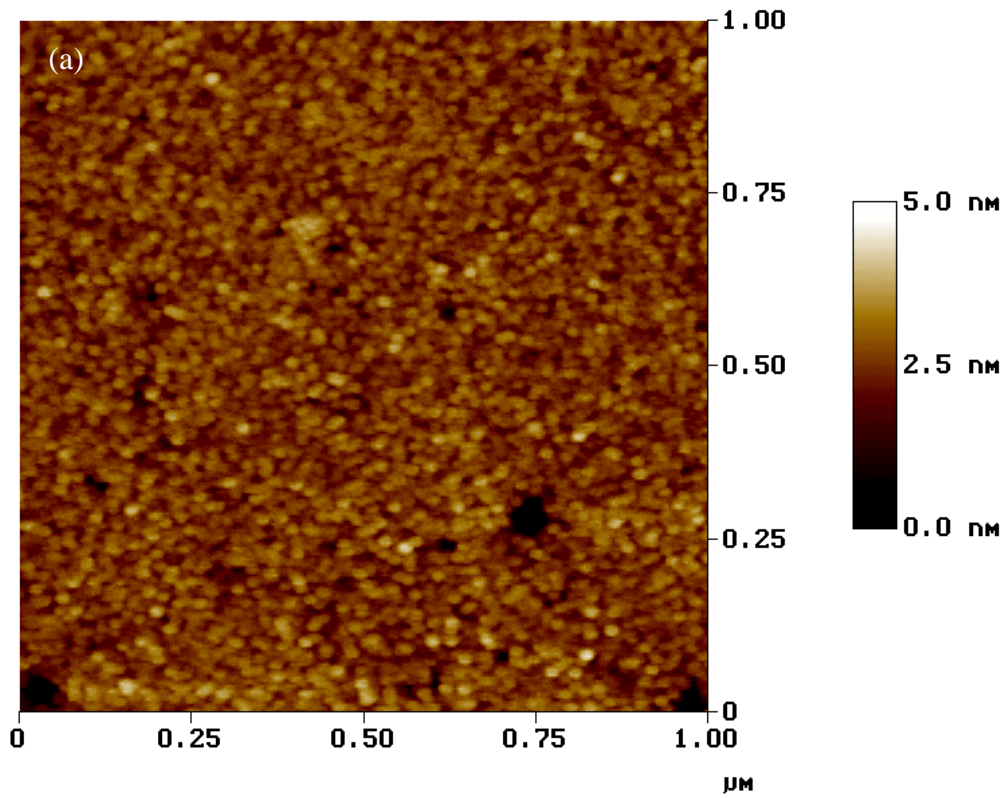


Fig. 2.5(a): Initial nucleation of a-Si films grown for 30 s at a) 25°C. The films have coalesced. The 25°C film has small, jagged nuclei while the 100°C film has larger, rounder nuclei.

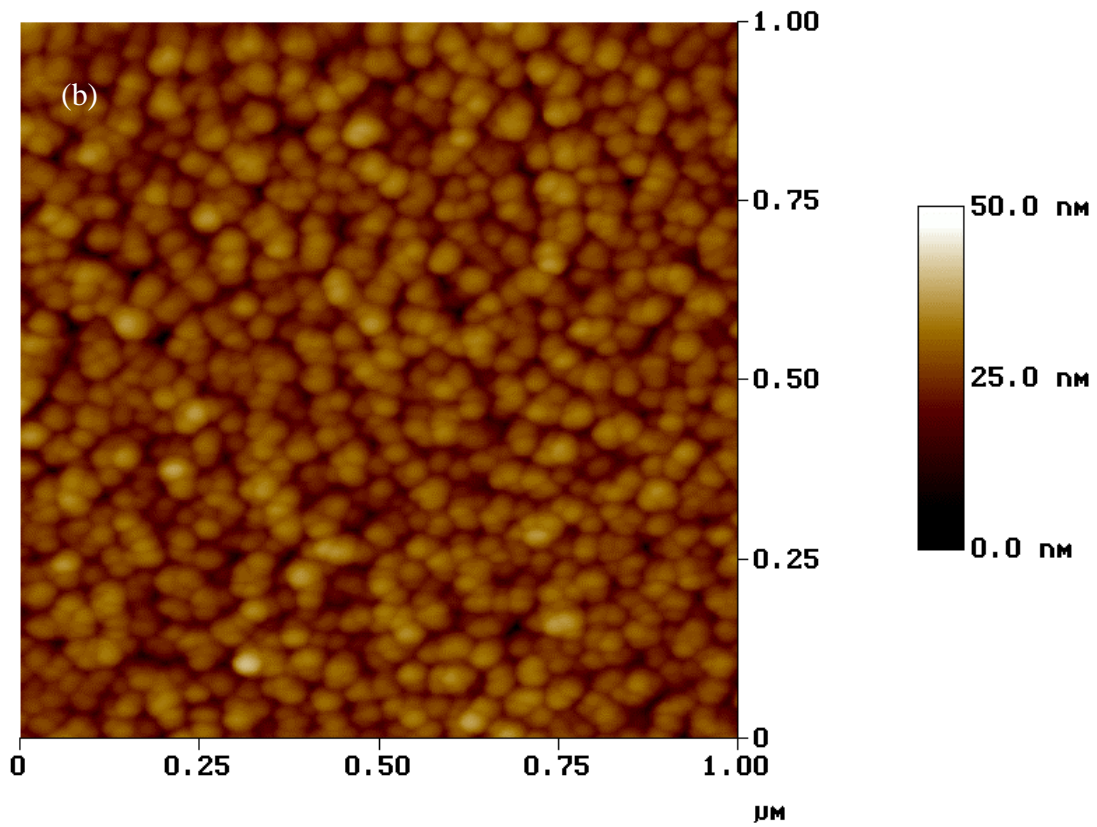


Fig. 2.5(b): Initial nucleation of a-Si films grown for 30 s at 100°C. The films have coalesced. The 25°C film has small, jagged nuclei, while the 100°C film has larger, rounder nuclei.

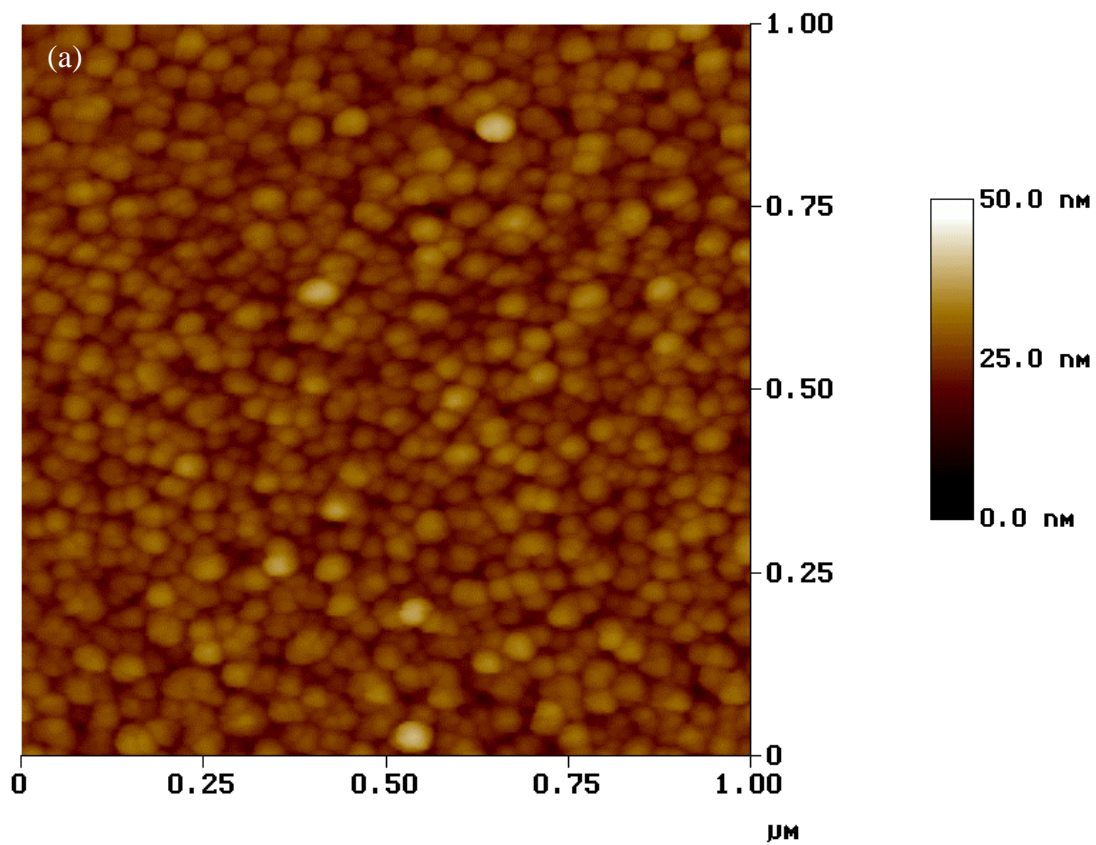


Fig. 2.6(a): Fully developed nucleation of films grown for 3 min at 25°C.

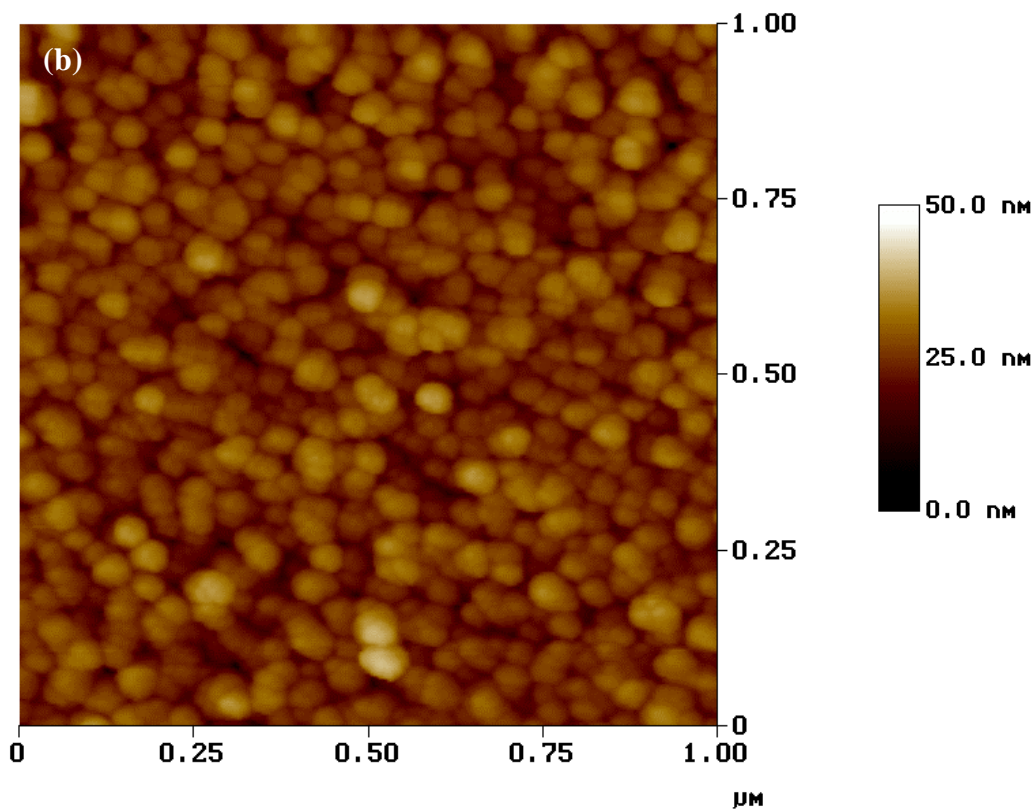


Fig. 2.6(b): Fully developed nucleation of films grown for 3 min at 100°C. There are no distinguishable differences between the topographies of the surfaces.

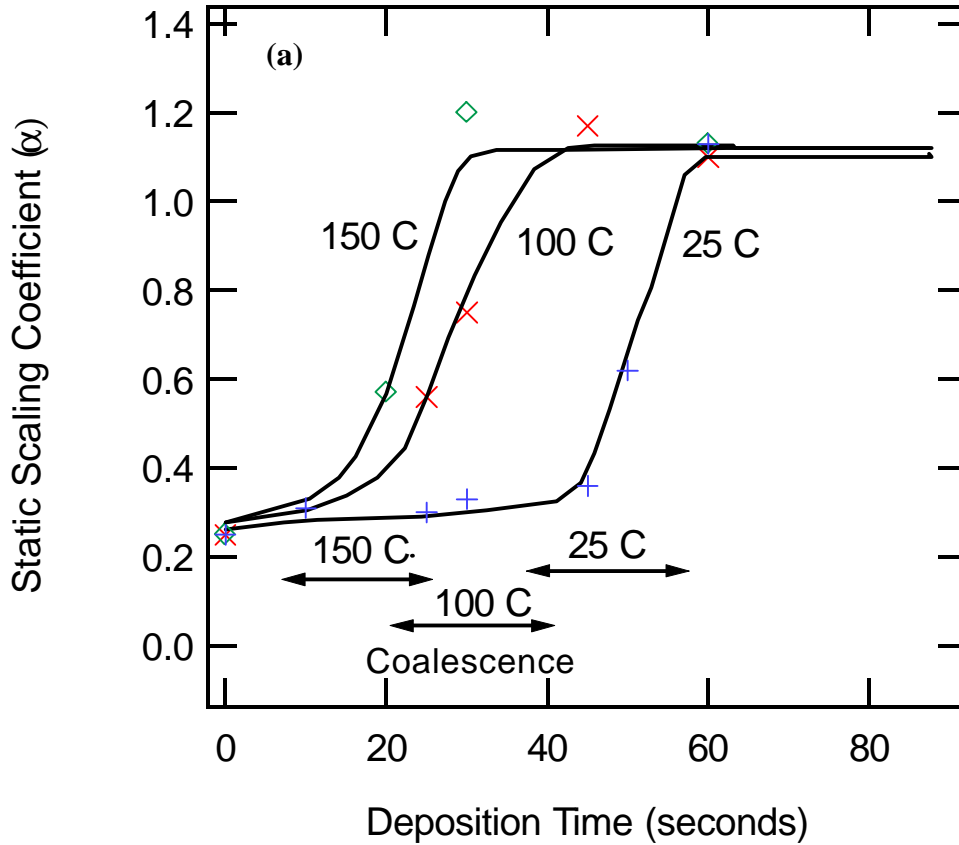


Fig. 2.7(a): Dependence of static scaling coefficient on deposition time and temperature for a-Si films deposited on c-Si substrates.  $\alpha$  increases with deposition time until it saturates at  $\alpha=1$ . The increase occurs more rapidly as temperature increases. Coalescence was determined by direct qualitative analysis of AFM images. A similar trend occurs for films grown on both c-Si and glass. The curves are guides for the eye.

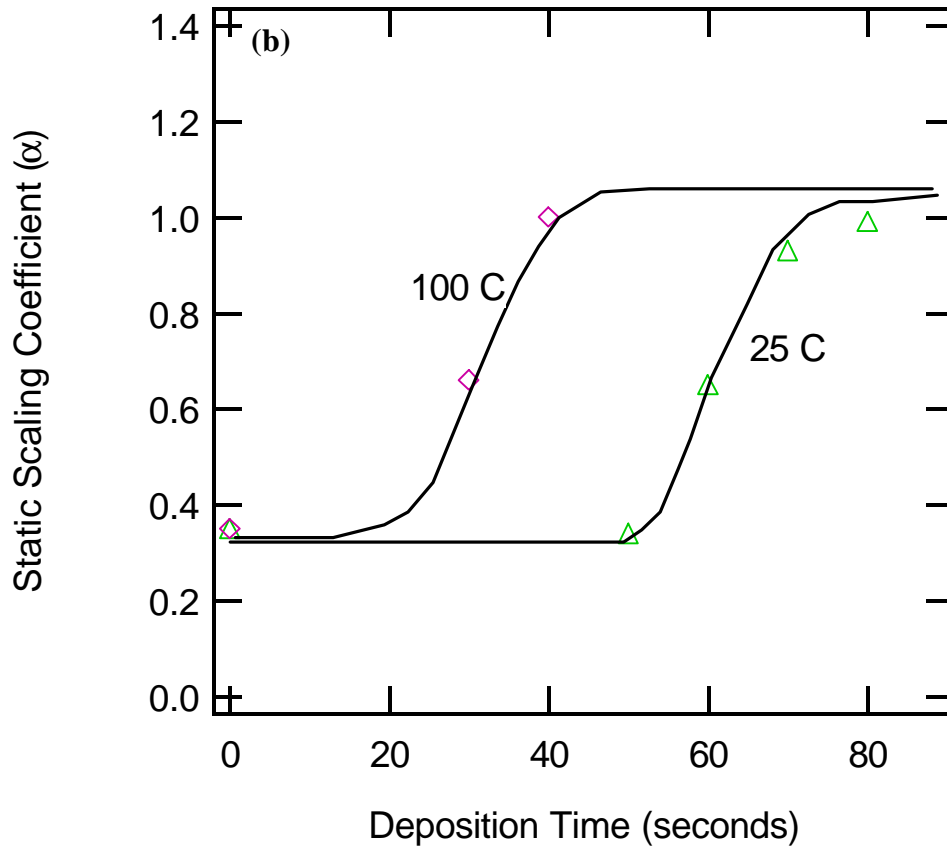


Fig. 2.7(b): Dependence of static scaling coefficient on deposition time and temperature for a-Si films deposited on glass substrates.  $\alpha$  increases with deposition time until it saturates at  $\alpha=1$ . The increase occurs more rapidly as temperature increases. Coalescence was determined by direct qualitative analysis of AFM images. A similar trend occurs for films grown on both c-Si and glass. The curves are guides for the eye.

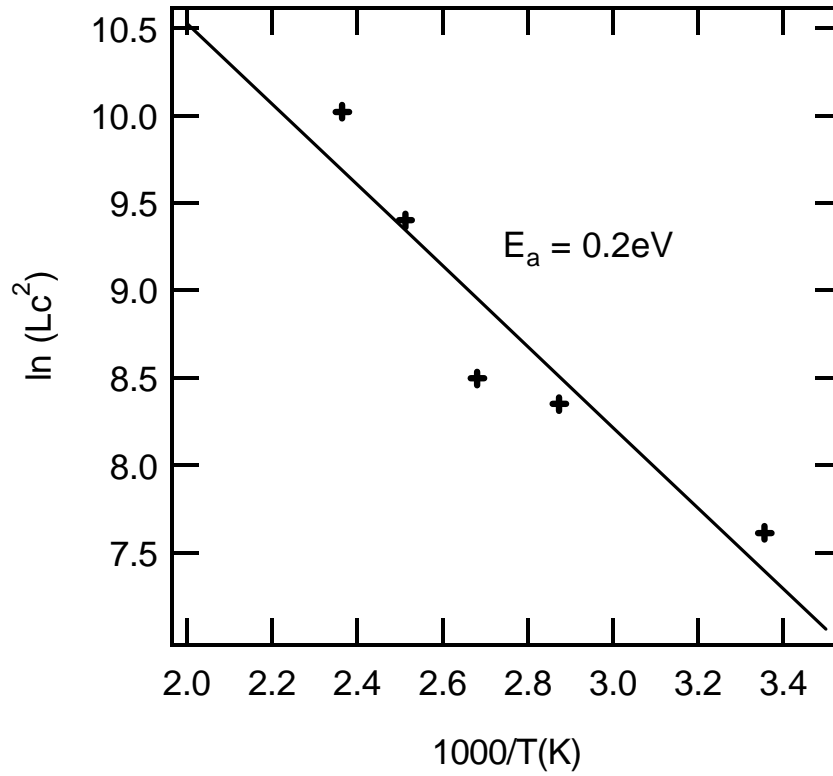


Fig. 2.8: Arrhenius plot of  $L_c^2$  for samples deposited for 20 minutes. The linear slope indicates a thermally activated diffusion process with an activation energy of  $E_a = 0.2\text{eV}$ .

*Chapter 3 is a reprint of a manuscript that appeared in Applied Physics Letters 80 (13)  
pp. 2356-2358, 2002.*

## **CHAPTER 3**

### **3 EFFECT OF HYDROGEN ON ADSORBED PRECURSOR DIFFUSION KINETICS DURING HYDROGENATED AMORPHOUS SILICON DEPOSITION**

by: Kevin R. Bray, Atul Gupta, and Gregory N. Parsons

*Department of Chemical Engineering, North Carolina State University, Raleigh, NC  
27695-7905*

#### **ABSTRACT**

Fractal analysis of the surface topography is used to study the effects of hydrogen dilution on the surface transport kinetics during the plasma deposition of hydrogenated amorphous silicon. Images obtained from atomic force microscopy are examined using dimensional fractal analysis, and surface diffusion lengths of growth precursors are

estimated from the measured correlation lengths. The addition of small amounts of hydrogen ( $\text{H}_2/\text{SiH}_4$  ratios  $<10/1$ ) during deposition leads to a decrease in the diffusion length, but larger hydrogen dilutions result in increased diffusion length. Moreover, the measured surface diffusion activation barrier is reduced from 0.20 eV for deposition from pure  $\text{SiH}_4$  to 0.13 eV with high hydrogen dilution. Results are consistent with recent models for precursor surface transport during low-temperature deposition, and give insight into critical processes for low-temperature silicon crystallization.

### 3.1 INTRODUCTION

Plasma deposition of hydrogenated amorphous silicon (a-Si:H) results in very smooth, conformal surfaces and non-thermally activated growth rates over temperatures ranging from  $<25^{\circ}$  to  $400^{\circ}\text{C}$  [1-4]. Typical models for a-Si:H growth presume that radical precursors generated in the gas phase adsorb and diffuse on the surface with low thermal barriers, giving rise to the observed smooth conformal surface coverage [2, 3, 5]. The evolution of surface roughness as a function of process conditions during film growth can be used to characterize transport processes on a-Si:H surfaces [6-8] and analyze kinetics of adsorbed precursor diffusion [9-11]. Experimental characterization of precursor diffusion is important because it can be used to evaluate and expand models of film growth, which are important to optimize and improve material quality. Moreover, because silicon plasma deposition involves only two elements (Si and H), it is an important model system to help advance understanding of low temperature activated film growth processes in general.

Critical parameters from the surface roughness evolution include the static and dynamic scaling coefficients,  $\alpha$  and  $\beta$ , and the lateral correlation length,  $L_c$ , and measurement of these parameters allow surface transport mechanisms, including viscous flow, evaporation/condensation, bulk diffusion, and surface diffusion, to be differentiated and identified. For self-similar surface structure, the lateral correlation length is related to the distance over which a connection in surface roughness extends, and  $L_c$  is related to the precursor diffusion length. Therefore, under correct conditions, the effect of deposition temperature on  $L_c$  gives insight into precursor transport kinetics [3, 6, 8, 11].

### 3.2 EXPERIMENTAL METHOD

In this article, the lateral correlation length is determined as a function of hydrogen dilution for amorphous silicon films deposited by plasma enhanced chemical vapor deposition (plasma CVD) from mixtures of silane, helium and hydrogen using temperature between 25°C and 350°C in two different reactor systems [12, 13]. Surface topography of the deposited films was characterized by atomic force microscopy, and frequency and dimensional analyses were used to extract correlation length from the topography data.

### 3.3 RESULTS

Results of dimensional analysis is shown in Figure 3.1, where the root-mean-square (rms) roughness is plotted vs. length scale for 1000Å thick amorphous silicon films deposited with SiH<sub>4</sub>/He/H<sub>2</sub> ratios of approximately: (a) 1/50/0; (b) 1/100/0; (c) 1/50/50; and (d) 1/150/50. For each sample the roughness increases with measurement length, then saturates at a value  $\sigma_{\text{sat}}$ . The lateral correlation length,  $L_c$ , is the distance at which the surface roughness first reaches its saturation value, and is ~50 nm for samples deposited without hydrogen, and is larger (~ 80 nm) for samples deposited with hydrogen under these conditions. The scaling analysis result in  $\alpha = 1$  and  $\beta = 0.26$  for films deposited with only SiH<sub>4</sub> and He, and  $\alpha = 0.7$  and  $\beta = 0.22$  for films deposited with

additional H<sub>2</sub> dilution. The difference in the scaling coefficients indicates a distinct difference in surface transport with hydrogen dilution, but the scaling parameters for all conditions studied are consistent with surface diffusion dominating surface transport [14]. It is important to note that not all conditions for silicon plasma deposition lead to surface transport dominated by diffusion. For example, parameters obtained from films deposited with argon dilution show non-self-similar scaling, so transport mechanisms cannot be simply evaluated [11].

The lateral correlation length was measured for films deposited at several H<sub>2</sub>/SiH<sub>4</sub> ratios at various temperatures, and the results are shown in Figure 3.2. For all temperatures studied, as the H<sub>2</sub>/SiH<sub>4</sub> ratio increases from 0 – 10, the correlation length is observed to decrease slightly. As the H<sub>2</sub>/SiH<sub>4</sub> ratio increases further, there is a rapid increase in the correlation length, which then saturates at a constant value. It was speculated that the observed change in lateral correlation length with hydrogen dilution could be simply due to gas phase dilution and a decrease in precursor flux. To test this possibility, the effect of gas dilution on L<sub>c</sub> was measured using helium/silane mixtures. The data in Figure 3.1 shows that as He dilution increases from 50/1 to 100/1 (samples a and b), the correlation length increases slightly, consistent with a small dilution effect. However, sample (c) with a 50/50 He/H<sub>2</sub> ratio has the same relative silane concentration as sample (b), but a significant increase in L<sub>c</sub> is observed. Similarly, when the helium flow is again increased from 50 to 150 sccm, only a small change in L<sub>c</sub> is observed. These results indicate that the changes in correlation length are primarily due to hydrogen and not due to changes in relative precursor flux to the surface.

The correlation length was measured for a series of a-Si:H films deposited over a range of substrate temperature (25 - 350°C), and the diffusion activation barrier ( $E_a$ ) was estimated from an Arrhenius plot of  $L_c^2$  vs.  $1/T$ . Figure 3.3 shows  $L_c^2$  vs.  $1/T$  for a set of films deposited with pure  $\text{SiH}_4$ , a set deposited with  $\text{SiH}_4/\text{He}$ , and two sets deposited with  $\text{SiH}_4/\text{He}/\text{H}_2$  mixtures. The data shows the same surface diffusion activation barrier (0.20 eV) for films grown with pure  $\text{SiH}_4$  and  $\text{SiH}_4/\text{He}$  mixtures. These two sets of films were deposited in different reactor systems, and the similarity in the two data sets indicates the robustness of the analysis. When  $\text{H}_2$  is added to the  $\text{SiH}_4/\text{He}$  mixture, an interesting trend in  $E_a$  is observed. For small amounts of  $\text{H}_2$ , ( $\text{H}_2/\text{SiH}_4 \sim 10$ )  $E_a$  remains at 0.20 eV, but for larger amounts of  $\text{H}_2$  a marked decrease in  $E_a$  to 0.13 eV is observed.

### 3.4 DISCUSSION

We can understand the trends in correlation length, adsorbed precursor diffusion length, and diffusion activation energy as follows. The diffusion distance is generally a function of the species residence time on the surface, the distance per “hopping” step, and the energetic barrier to hopping. When relatively small amounts of hydrogen are used, the precursor diffusion length is observed to decrease, and the activation energy is not significantly affected. This reduction in the diffusion length is attributed to the reduced residence time of the growth precursors on the surface due to additional flux of incident H radicals that increases the direct abstraction of adsorbed silyl precursors from the surface. Under larger flux conditions, however, the diffusion length is observed to increase, and the barrier for diffusion is observed to decrease. The decrease in  $E_a$  and

increase in  $L_c$  are ascribed to a change in dominant surface hydride bonding. Hydrogen exposure will remove higher surface hydrides by abstraction, and promote more mono-hydride surface bonding. It has been proposed that the monohydride surface presents a smaller barrier for precursor diffusion as compared to di- and tri-hydride bonded regions [15]. This surface hydrogen dependent transport model is fully consistent with widely known experimental results describing the growth rate [16, 17], bonded hydrogen distribution [18, 19], surface reaction probabilities [16], and with predicted trends in diffusion activation barriers based on a detailed kinetic analysis of dominant reaction processes that occur during deposition [15].

### **3.5 CONCLUSIONS**

We believe that results presented here have important implications for understanding silicon deposition, as well as crystallization during plasma CVD. While it is possible that the observed reduction in precursor diffusion barrier upon hydrogen dilution results from a transition from amorphous to micro-crystalline structure, it is important to note that the explanation presented above does not specifically rely on surface crystallization. In this picture therefore, the increase in precursor diffusion length upon hydrogen dilution could occur before significant crystallization of the growth surface. This means that the increased surface diffusion length could be a condition that promotes crystallization, rather than a resulting product of the crystallized surface structure.

### 3.6 ACKNOWLEDGEMENTS

This work was supported under NSF Grants CTS-9624612 and 0072784.

### 3.7 APPENDIX

Previous work has also looked at the effects of hydrogen dilution during a-Si:H deposition. Below we review these results in relation to our work.

The increase in  $L_c$  with hydrogen dilution is consistent with the increase in the surface diffusion length with increasing hydrogen dilution indirectly observed in other studies [20-22]. Ellipsometry measurements of a-Si:H deposited using conventional PECVD showed films deposited with increased hydrogen dilution had lower surface roughness, which was attributed to increased surface diffusion lengths [20]. The effect of hydrogen dilution was also studied by depositing a-Si:H and  $\mu\text{c-Si:H}$  on rough substrates using dc reactive magnetron sputtering and observing the surface roughness decrease with increasing film thickness [21]. The roughness decreased more rapidly with increasing hydrogen dilution, indicating an increase in the surface diffusion. The crystalline volume fraction of microcrystalline silicon has been observed to increase with increasing hydrogen dilution [1]. This increase has been ascribed to increased diffusion lengths. The effect of hydrogen on silicon nucleation and coalescence was investigated by using Auger electron spectroscopy to observe the Si and Ga fractions during  $\mu\text{c-Si}$  deposition onto GaAs substrates [22]. The Ga signal goes to zero at the coalescence

point. The coalescence is observed more rapidly with hydrogen dilution, indicating enhanced precursor diffusion.

A study using attenuated total reflection Fourier transform infrared (ATR-FTIR) spectroscopy [19] has shown that the surface coverage during a-Si:H growth changes from predominantly di- and trihydrides to predominantly monohydride with a 20/1  $H_2/SiH_4$  dilution ratio during deposition. The observed increase in the diffusion length with high hydrogen dilution may be an effect of a change in the surface diffusion barrier due to the change in the hydride surface coverage.

### 3.8 REFERENCES

- [1] A. Matsuda, *Journal of Non-Crystalline Solids*, **59-60**, 767 (1983).
- [2] J. Perrin, M. Shiratani, P. Kae-Nune, H. Videlot, J. Jolly, and J. Guillon, *Journal of Vacuum Science and Technology A*, **16**, 278 (1998).
- [3] J. Robertson, *Journal of Applied Physics*, **87**, 2608 (2000).
- [4] A. Matsuda, *Plasma Physics and Controlled Fusion*, **39**, 431 (1997).
- [5] G. Ganguly and A. Matsuda, *Journal of Non-Crystalline Solids*, **164-166**, 31 (1993).
- [6] D.M. Tanenbaum, A.L. Laracuate, and A. Gallagher, *Physical Review B*, **56**, 4243 (1997).
- [7] M. Kondo, T. Ohe, K. Saito, T. Nishimiya, and A. Matsuda, *Journal of Non-Crystalline Solids*, **227-230**, 890 (1998).
- [8] W.M. Tong, E.J. Snyder, and R.S. Williams, *Surface Science*, **277**, L63 (1992).
- [9] L. Bardotti, C.R. Stoldt, C.J. Jenks, M.C. Bartlet, J.W. Evans, and P.A. Thiel, *Physical Review B*, **57**, 12544 (1998).
- [10] B. Reinker, M. Moske, and K. Samwer, *Physical Review B*, **56**, 9887 (1997).
- [11] K.R. Bray and G.N. Parsons, *Physical Review B*, **65**, 035311 (2002).
- [12] E. Srinivasan, D.A. Lloyd, and G.N. Parsons, *Journal of Vacuum Science and Technology A*, **15**, 77 (1997).
- [13] C.S. Yang, W.W. Read, C. Arthur, E. Srinivasan, and G.N. Parsons, *IEEE Electron Device Letters*, **19**, 180 (1998).
- [14] A.L. Barabasi and H.E. Stanley, *Fractal Concepts in Surface Growth* (Cambridge UP, Cambridge, 1995).

- [15] A. Gupta, K.R. Bray, and G.N. Parsons, submitted for publication.
- [16] A. Matsuda and T. Goto, Materials Research Society Symposium Proceedings, **164**, 3 (1990).
- [17] M.C.M. van de Sanden, W.M.M. Kessels, R.J. Severens, and D.C. Schram, Plasma Physics and Controlled Fusion, **41**, A365 (1999).
- [18] W.M.M. Kessels, A.H.M. Smets, D.C. Marra, E.S. Aydil, D.C. Schram, and M.C.M. van de Sanden, Thin Solid Films, **383**, 154 (2001).
- [19] D.C. Marra, E.A. Edelberg, R.L. Naone, and E.S. Aydil, Applied Surface Science, **133**, 148 (1998).
- [20] H. Fujiwara, Y. Toyoshima, M. Kondo, and A. Matsuda, Journal of Non-Crystalline Solids, **266-269**, 38 (2000).
- [21] J.E. Gerbi and J.R. Abelson, Journal of Applied Physics, **89**, 1463 (2001).
- [22] A. Matsuda, Thin Solid Films, **337**, 1 (1999).

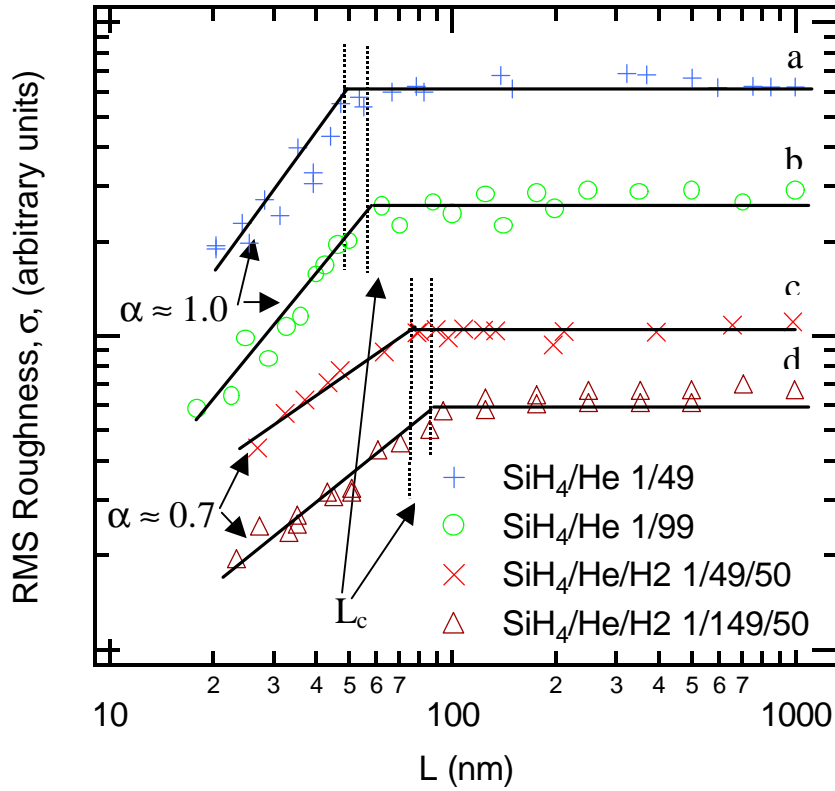


Fig. 3.1: Fractal analysis of 1000Å a-Si:H films deposited with varying helium and hydrogen dilutions. a)  $\text{SiH}_4/\text{He}$  1/49, b)  $\text{SiH}_4/\text{He}$  1/99, c)  $\text{SiH}_4/\text{He}/\text{H}_2$  1/49/50, d)  $\text{SiH}_4/\text{He}/\text{H}_2$  1/149/50. The correlation length,  $L_c$ , where the RMS roughness saturates with length, increases with hydrogen dilution. The curves are offset for clarity. Lines are guides for the eye.

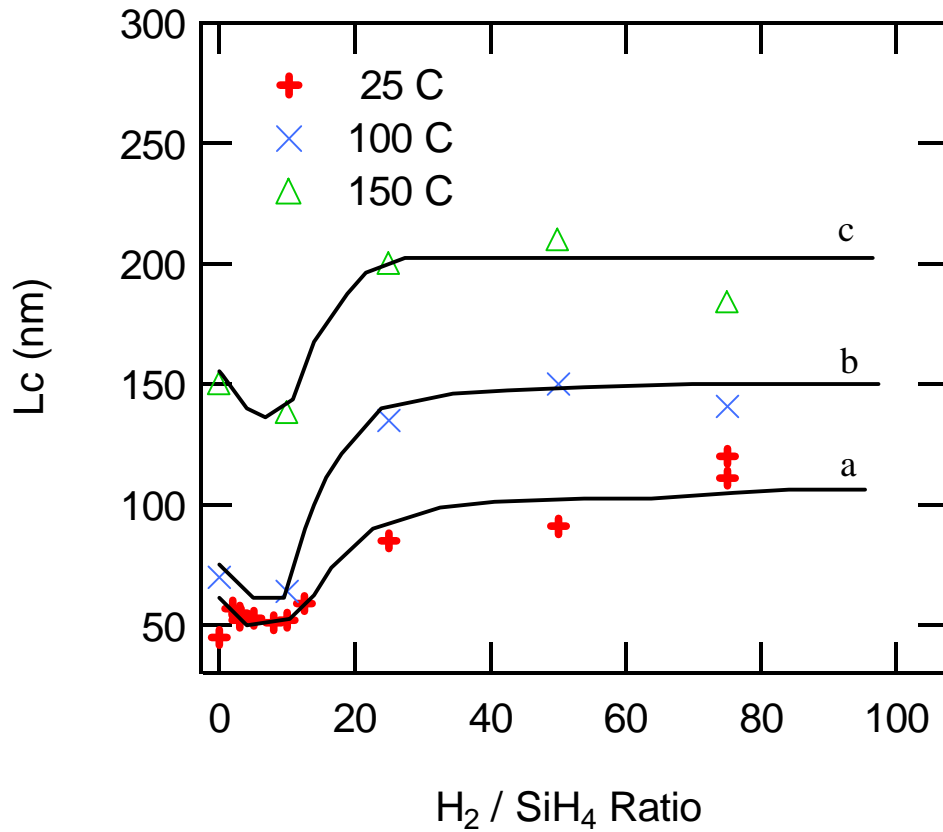


Fig. 3.2: The correlation length,  $L_c$  vs. the  $H_2/SiH_4$  ratio.  $L_c$  remains constant with low  $H_2$  dilutions, then increases with high hydrogen dilutions for films deposited at a) 25°C, b) 100°C, and c) 150°C. The lines are guides for the eye.

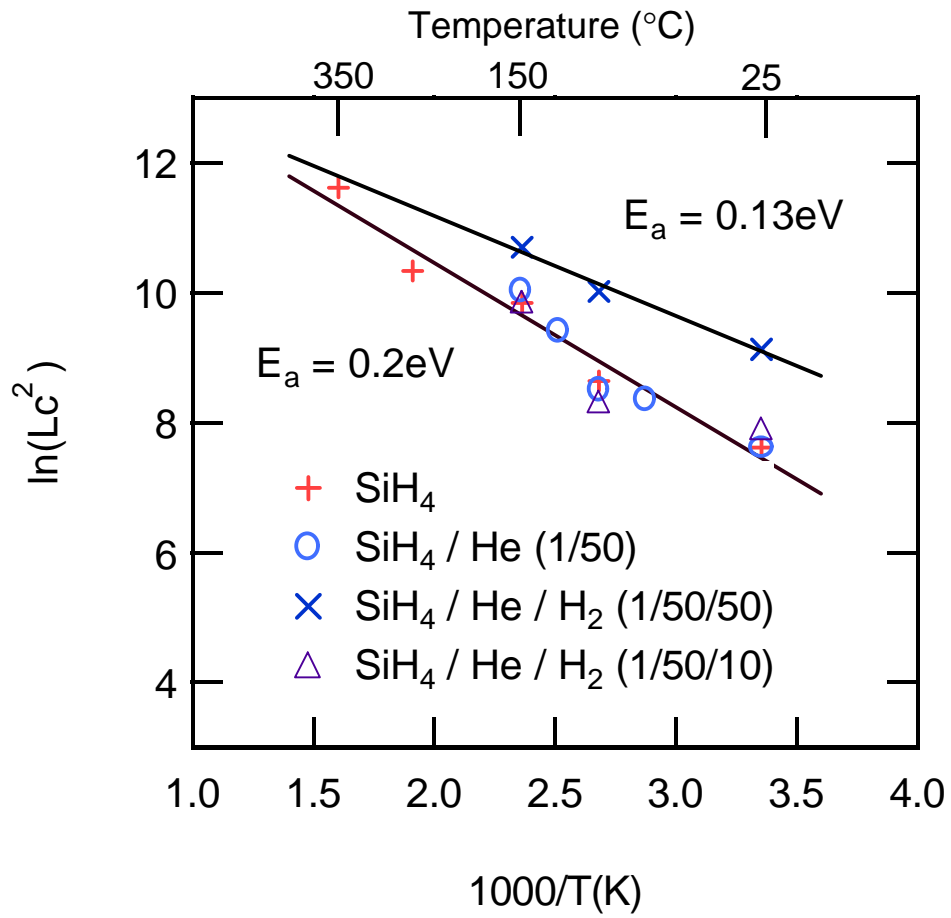


Fig. 3.3: Arrhenius plots of  $\ln(L_c^2)$  vs.  $1/T$  for a-Si:H films deposited from  $\text{SiH}_4$  (from reactor two),  $\text{SiH}_4/\text{He}$  and  $\text{SiH}_4/\text{He}/\text{H}_2$  mixtures (from reactor one).

*Chapter 4 is a draft of a manuscript to be submitted for publication.*

## **CHAPTER 4**

# **4 EFFECTS OF DEPOSITION CONDITIONS ON THE SURFACE TRANSPORT KINETICS IN LOW TEMPERATURE SILICON DEPOSITION**

by: Kevin R. Bray and Gregory N. Parsons

*Department of Chemical Engineering, North Carolina State University, Raleigh NC  
27695-7905*

### **ABSTRACT**

The surface transport kinetics of plasma deposited hydrogenated amorphous silicon are investigated using topography analysis. The effects of RF power density, diluent gas, process pressure and reactor geometry are investigated. Increasing RF power density increases the correlation length, but does not change the surface diffusion barrier. Films deposited in different reactors display similar diffusion barriers. Altering the incident radical flux by varying the process pressure changes the correlation length and the diffusion barrier. Decreasing pressure increases the diffusion length. A shift in the

activation barrier at high temperatures for films deposited from  $\text{SiH}_4/\text{H}_2$  may correspond with the amorphous to microcrystalline transition but the static scaling coefficient indicates that surface diffusion is the dominant transport mechanism on both the amorphous and microcrystalline materials. These results are discussed in relation to recent models for surface transport in low-temperature amorphous silicon growth.

## 4.1. INTRODUCTION

Plasma deposition of hydrogenated amorphous silicon results in very smooth, conformal surfaces and non-thermally activated growth rates over temperatures ranging from  $<25^{\circ}$  to  $400^{\circ}\text{C}$  [1-5]. Current technology operates far from thermodynamic equilibrium where kinetic processes control film growth. Typical kinetic models for a-Si:H growth presume that radical precursors generated in the gas phase adsorb and diffuse on the surface with low thermal barriers, giving rise to the observed smooth conformal surface coverage [2, 3, 6, 7]. Surface transport parameters are not usually measured directly. Experimental macroscopic parameters (such as growth rate or step coverage) are typically compared with precursor dependent reaction models [8, 9], or are estimated through simulations [3, 6, 10-12].

A new idealized kinetic model for amorphous silicon growth has been developed based on surface hydride dependent diffusion barriers [7]. In the model, growth proceeds from  $\text{SiH}_3$  radicals in the absence of atomic hydrogen or ions. The surface diffusion properties are surface coverage dependent. The apparent surface diffusion barrier decreases as the surface coverage species change from tri-hydrides to mono-hydrides. The barrier for physisorbed radical to diffuse is higher on a tri-hydride than on a mono-hydride surface. Surface coverage can be altered by adjusting the incident radical flux or the substrate temperature. Under high flux, di- and tri-hydride species dominate the surface composition. This is due to an increase in adsorption events, effectively decreasing the reaction time available for hydrogen elimination events. With increasing temperature, hydrogen recombination reactions reduce the hydride coverage from tri-

hydride to mono-hydride species. The evolution of surface roughness as a function of process conditions during film growth can be used to characterize transport processes and analyze kinetics of adsorbed precursor diffusion [13-19]. Experimental characterization of precursor diffusion is important because it can be used to evaluate and expand models of film growth, which are important to optimize and improve material quality.

Critical parameters from the surface roughness evolution include the static and dynamic scaling coefficients,  $\alpha$  and  $\beta$ , and the lateral correlation length,  $L_c$ . Measurement of these parameters allows surface transport mechanisms, including viscous flow, evaporation/condensation, bulk diffusion, and surface diffusion, to be differentiated and identified [15, 20]. For surface diffusion dominated surface structure, the lateral correlation length is related to the distance over which a connection in surface roughness extends, and  $L_c$  is related to the precursor diffusion length. Therefore, under correct conditions, the effect of deposition temperature on  $L_c$  gives insight into precursor transport kinetics [3, 15, 16, 17, 19]. In this paper, experimental data from topography analysis is compared with predicted trends from the kinetic model.

## **4.2 EXPERIMENTAL METHOD**

### **4.2.1 Hydrogenated Amorphous Silicon Deposition**

Hydrogenated amorphous silicon was deposited using plasma enhanced chemical vapor deposition (PECVD). To study if the diffusion barriers observed were universal and not an artifact linked to the reactor system used for deposition, two reactors with different geometries and gas flow patterns were used to deposit amorphous silicon films.

Our first reactor used for amorphous silicon deposition is a capacitively coupled rf (13.56 MHz) parallel plate PECVD system with circular geometry (2.2 cm electrode separation, 28 cm diameter) and radial gas flow [21]. Amorphous silicon films were deposited with substrate temperatures ranging from 25 - 150°C at 0.6 Torr. The effect of RF power was studied by varying the power density from 5 – 50 mW/cm<sup>2</sup>. The source gas was 2% SiH<sub>4</sub> in He with a SiH<sub>4</sub>/He flowrate of 100 standard cubic centimeters per minute (sccm) was maintained. H<sub>2</sub> was added as a diluent gas.

The second reactor utilized in these experiments was a large area (1000 cm<sup>2</sup>) load-locked, parallel plate PECVD reactor with an electrode spacing of 1.6 cm [22]. A showerhead gas distribution system is used for the uniform delivery of gases into the reaction zone, resulting in uniform film growth over the electrode area. Hydrogenated amorphous silicon films were deposited from pure SiH<sub>4</sub> and SiH<sub>4</sub>/H<sub>2</sub> mixtures at substrate temperatures from 25 - 450°C, at a power density of 60 mW/cm<sup>2</sup> and pressures ranging from 0.15 - 1.2 Torr.

#### **4.2.2 Topography Analysis**

Atomic force microscopy (AFM) for surface topography analysis was conducted using a Digital Instruments Dimension 3000, with a Nanoscope IIIa controller and vibration-shielded hood. Imaging was performed in intermittent contact mode, using c-Si cantilever probes with a nominal tip radius of 5 – 10 nm. Image analysis was performed using built-in software functions to calculate the root-mean-square (rms) roughness,  $\sigma$ . Scan sizes of 200 x 200nm<sup>2</sup>, 500 x 500nm<sup>2</sup>, 1 x 1 $\mu$ m<sup>2</sup>, and 5 x 5  $\mu$ m<sup>2</sup> were measured to

insure there were no artificial effects introduced into the analysis from the scan size. The probe tip was changed as needed to maintain good images. All AFM measurements were performed under ambient conditions.

## **4.3 RESULTS AND DISCUSSION**

The surface topography was used to analyze surface diffusion lengths and activation barriers as a function of substrate temperature and process pressure, diluent gas species in different reactor configurations, and RF power density.

### **4.3.1 Temperature and Process Pressure**

The effect of temperature is investigated in Fig. 4.1(a) and (b). Figure 4.1(a) contains a plot of  $\ln(L_c^2)$  vs.  $1/T$  for films deposited at 0.4 and 1.2 Torr. At low temperatures the correlation length increases with increasing temperature, consistent with thermally activated surface diffusion. A maximum in the diffusion length is seen from 200°C to 300°C then the diffusion length decreases with temperature. The decrease in diffusion length at high temperatures has been attributed to an increase in the creation of dangling bonds on the surface through hydrogen desorption. As the dangling bond density increases diffusing species travel a shorter distance before finding a chemisorption site.

Changes in process pressure also alter the incident radical flux to the surface and are predicted to change the transport kinetics on the surface [7]. Increased pressure

increases the flux of silyl radicals to the surface. Under high flux, di- and tri-hydride species dominate the surface composition. This is due to an increase in adsorption events, effectively decreasing the reaction time available for hydrogen elimination events. Figure 4.1(b) shows a plot of the RMS roughness vs. the length scale for films deposited at 100°C with different pressures. The correlation length can be seen to increase as the pressure decreases from 1.2 Torr to 0.4 Torr. As the pressure is decreased further to 0.15 Torr, the correlation length decreases. From Fig. 4.1(a) diffusion activation barriers are extracted. The diffusion barrier increased from 0.17 eV to 0.18 eV as the pressure increased from 0.4 Torr to 1.2 Torr. The increased barrier leads to a decrease in the diffusion length.

The decrease in the correlation length at very low pressures seen in Fig. 4.1(b) may be due to a change in plasma composition in this regime. At lower pressure, the mean free path of the gas phase species is expected to increase. This will allow more hydrogen to reach the growth surface. Small increases in the hydrogen flux have been shown to decrease diffusion lengths on the surface, possibly through extraction of the diffusing physisorbed precursors [16]. At low pressures, hydrogen present in the system may take of more prominent role in the deposition process. This indicates that our kinetic model may not describe low-pressure amorphous silicon depositions in the presence of atomic hydrogen.

### 4.3.2 Diluent Gas

The influence of hydrogen dilution was next studied. Figure 4.2 shows an Arrhenius plot for films deposited with a 20/1  $H_2/SiH_4$  ratio from 25 – 150°C in the radial gas flow reactor and from 25 – 350°C the large area showerhead reactor. The correlation lengths were seen to differ slightly. This difference may be due to different growth rates in the reactors. But the activation barriers are similar and indicate that the analytical procedure used here is robust and is independent of the deposition tool. Above 150°C, a shift is seen in the diffusion length. This transition may result from a transition from amorphous to microcrystalline material. Microcrystalline silicon has been shown to coalesce more rapidly than amorphous silicon, indicating that it has a longer diffusion length [9]. Microcrystalline silicon has predominately mono-hydride surface coverage compared to di- and tri-hydride coverage for amorphous silicon [23]. Lower hydride species on the surface are consistent with the observed change in the diffusion length in Fig. 4.2.

Figure 4.3 and 4.4 show AFM images for films deposited in the showerhead reactor at 150°C and 350°C from pure  $SiH_4$  and  $H_2/SiH_4 = 20/1$  respectively. As seen in Fig. 4.3, there is little change in the RMS roughness of the films deposited from  $SiH_4$  ( $\sigma = 1.00\text{nm}$  at 150°C and  $\sigma = 1.01\text{ nm}$  at 350°C). With  $H_2$  dilution there is a much more pronounced difference in the roughness observed. In Fig. 4.4(a),  $\sigma = 2.25\text{ nm}$  for a film deposited at 150°C and in Fig. 4.4(b),  $\sigma = 9.23$  for a film deposited at 350°C. The large change in RMS roughness seen between Fig. 4.4(a) and 4.4(b) may indicate a transition

from amorphous to microcrystalline silicon. Figure 4.5 is a plot of the RMS roughness vs. the measurement length for films deposited with SiH<sub>4</sub> and H<sub>2</sub> at 25°C and 350°C. The saturated RMS roughness and the correlation length are much larger for the 350°C film than the 25°C film. But static scaling coefficient is the same for both of these films with  $\alpha = 0.7$ . These  $\alpha$  values are consistent with surface diffusion processes controlling the surface topography on both surfaces.

### 4.3.2 RF Power Density

Figure 4.6 shows the surface diffusion barrier,  $E_a$ , and the lateral correlation length,  $L_c$ , as a function of RF power density from 8 – 48 mW/cm<sup>2</sup> for amorphous silicon deposited in the radial flow reactor. The correlation length is seen to increase with increasing power density. The diffusion length,  $L_D$ , is defined as:

$$L_D = \sqrt{a^2 n_h \exp\left(\frac{-E_a}{kT}\right) t} \quad (1)$$

and is a function of the hopping distance,  $a$ , the hopping frequency,  $\nu_h$ , the diffusion barrier,  $E_a$ , the substrate temperature,  $T$ , and the surface residence time,  $\tau$ . Changes in the diffusion length observed in Fig. 4.6 could come from a change in any of these parameters. The hopping distance is defined as the lattice spacing and is expected to remain constant. Although the films are amorphous and the distance between hopping sites will vary, the average for multiple hops should be constant. The diffusion barrier remains constant with RF power density, as shown in Fig. 4.6. The surface residence time is the time available for a radical to react on the surface is defined as:

$$t = \frac{q_{phys}}{f} \quad (2)$$

where  $\theta_{phys}$  is the physisorbed radical surface coverage and  $\phi$  is the incident flux. Under steady state growth conditions both values are constant and the residence time will remain constant. The hopping frequency can influence the diffusion length. The increase in power density may increase the ion bombardment from the plasma. Studies of ion enhanced surface diffusion of germanium on silicon have shown an increase in the diffusion preexponential factor while the activation barrier remains constant [24]. Low energy ions primarily contribute to an enhancement of the surface mobility of adsorbed species [25]. Energy transfer from the ions is not sufficient to dislodge most adatoms and only provides a slight additional energy to atoms already possessing nearly sufficient energy to diffuse [24].

#### 4.4 SUMMARY AND CONCLUSION

Surface topography analysis has been used to characterize hydrogenated amorphous silicon deposited using plasma enhanced chemical vapor deposition. The effects of substrate temperature and process pressure have been investigated. The diffusion length increases with increasing temperature up to a transition temperature. Above the transition temperature, the diffusion length decreases rapidly. The trend in the diffusion length with temperature is followed at all the pressures studied. A new kinetic growth model predicts similar trends of diffusion length versus substrate temperature. The model works well between 0.4 and 1.2 Torr for a pure silane plasma. The model does not account for the presence of hydrogen or ions. Deposition under process

conditions that promote these species should not follow the model predictions, even in the pressure regime where the model is accurate for silane plasmas. At lower pressures the model also breaks down. This may be due to an increased mean free path of hydrogen in the plasma, allowing hydrogen flux to the surface to become significant. Although not yet experimentally tested, the model is also expected to depart from experimental results at high pressures. In this regime, SiH and SiH<sub>2</sub>, not included in the model, become more abundant and contribute toward film growth.

The process pressure also influences the diffusion length. The diffusion length increases with decreasing pressure. These results are consistent with a proposed surface hydride dependent kinetic growth model where the tri-hydride surface coverage increases with increasing flux. The surface diffusion activation barrier decreases with decreasing pressure, and may be responsible for the increased diffusion. At very low pressures, the diffusion length decreases, a departure from the predictions in our model. This decrease in the diffusion length may be due to the presence of atomic hydrogen from the plasma, which is not accounted for in the model.

At low power densities ( $< 50 \text{ mW/cm}^2$ ), as the power density increases, the diffusion length increases. The diffusion barrier remains constant in the power density range studied ( $5 - 50 \text{ mW/cm}^2$ ). This increase in diffusion length with a constant diffusion barrier is consistent with ion bombardment enhanced movement of mobile surface species, but does not significantly change the surface coverage. The kinetic model was developed without the influence of ion bombardment. These results indicate that low energy ion bombardment does not change the diffusion barrier by altering the

surface coverage through sputtering. A modification to include the enhanced surface diffusion induced by low energy ions would expand the capabilities of our model.

An analysis of the static scaling coefficient indicates that the surface transport mechanism does not change as films go through the amorphous to microcrystalline transition. Films deposited in the amorphous and microcrystalline regimes both exhibited similar scaling coefficients, demonstrating that surface diffusion dominates the transport on both surfaces.

#### **4.5 ACKNOWLEDGEMENTS**

This work was supported under NSF Grant No. 0072784 and DARPA.

## 4.6 REFERENCES

- [1] A. Matsuda, *Journal of Non-Crystalline Solids*, **59-60**, 767 (1983).
- [2] J. Perrin, M. Shiratani, P. Kae-Nune, H. Videlot, J. Jolly, and J. Guillon, *Journal of Vacuum Science and Technology A*, **16**, 278 (1998).
- [3] J. Robertson, *Journal of Applied Physics*, **87**, 2608 (2000).
- [4] A. Matsuda, *Plasma Physics and Controlled Fusion*, **39**, 431 (1997).
- [5] W.M.M. Kessels, A.H.M. Smets, D.C. Marra, E.S. Aydil, D.C. Schram, and M.C.M. van de Sanden, *Thin Solid Films*, **383**, 154 (2001).
- [6] G. Ganguly and A. Matsuda, *Journal of Non-Crystalline Solids*, **164-166**, 31 (1993).
- [7] A. Gupta, K.R. Bray, and G.N. Parsons, unpublished, .
- [8] K. Maeda, A. Kuroe, and I. Umezu, *Physical Review B-Condensed Matter*, **51**, 10635 (1995).
- [9] A. Matsuda, *Thin Solid Films*, **337**, 1 (1999).
- [10] M.J. Kushner, *Journal of Applied Physics*, **62**, 4763 (1987).
- [11] K.K. Gleason, K.S. Wang, M.K. Chen, and J.A. Reimer, *Journal of Applied Physics*, **61**, 2866 (1987).
- [12] R. Robertson and A. Gallagher, *Journal of Chemical Physics*, **85**, 3623 (1986).
- [13] L. Bardotti, C.R. Stoldt, C.J. Jenks, M.C. Bartlet, J.W. Evans, and P.A. Thiel, *Physical Review B*, **57**, 12544 (1998).
- [14] B. Reinker, M. Moske, and K. Samwer, *Physical Review B*, **56**, 9887 (1997).
- [15] K.R. Bray and G.N. Parsons, *Physical Review B*, **65**, 035311 (2002).
- [16] K.R. Bray, A. Gupta, and G.N. Parsons, *Applied Physics Letters*, **80**, 2356 (2002).

- [17] D.M. Tanenbaum, A.L. Laracuente, and A. Gallagher, *Physical Review B-Condensed Matter*, **56**, 4243 (1997).
- [18] M. Kondo, T. Ohe, K. Saito, T. Nishimiya, and A. Matsuda, *Journal of Non-Crystalline Solids*, **227-230**, 890 (1998).
- [19] W.M. Tong, E.J. Snyder, and R.S. Williams, *Surface Science*, **277**, L63 (1992).
- [20] W.M. Tong and R.S. Williams, *Annual Review of Physical Chemistry*, **45**, 401 (1994).
- [21] E. Srinivasan, D.A. Lloyd, and G.N. Parsons, *Journal of Vacuum Science and Technology A*, **15**, 77 (1997).
- [22] C.S. Yang, W.W. Read, C. Arthur, E. Srinivasan, and G.N. Parsons, *IEEE Electron Device Letters*, **19**, 180 (1998).
- [23] D.C. Marra, E.A. Edelberg, R.L. Naone, and E.S. Aydil, *Applied Surface Science*, **133**, 148 (1998).
- [24] R. Ditchfield and E.G. Seebauer, *Physical Review Letters*, **82**, 1185 (1999).
- [25] J. Perrin, J. Schmitt, C. Hollenstein, A. Howling, and L. Sansonnens, *Plasma Physics and Controlled Fusion*, **42**, B353 (2000).

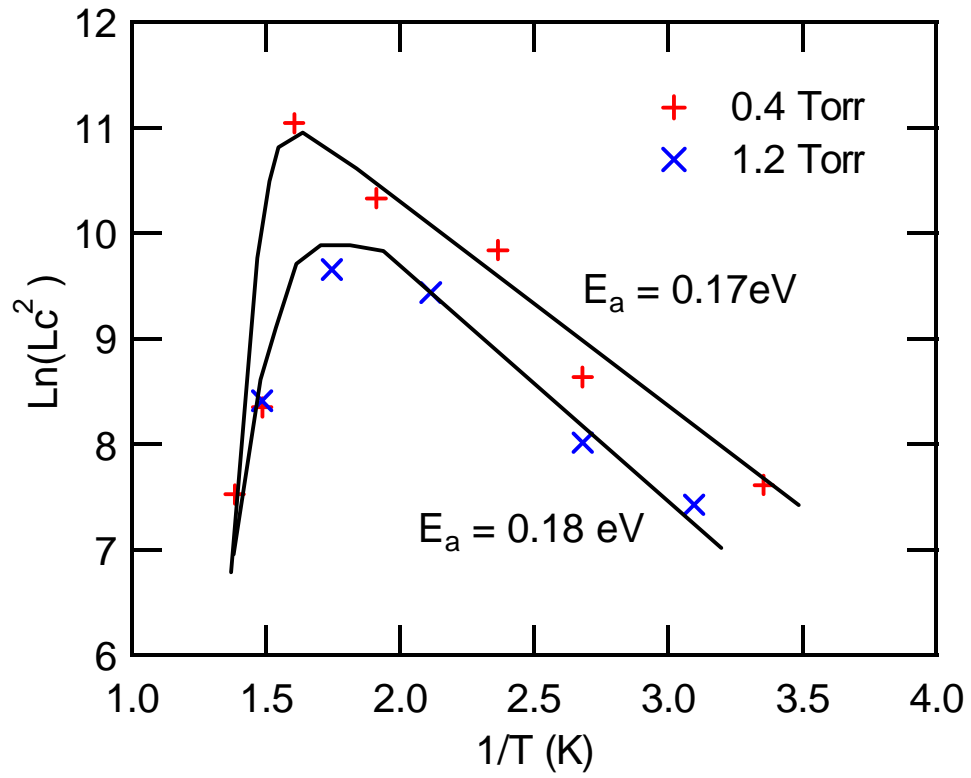


Fig. 4.1(a): Effect of Process Pressure. Arrhenius plot of  $\ln(L_c^2)$  vs.  $1/T$  at various pressures.

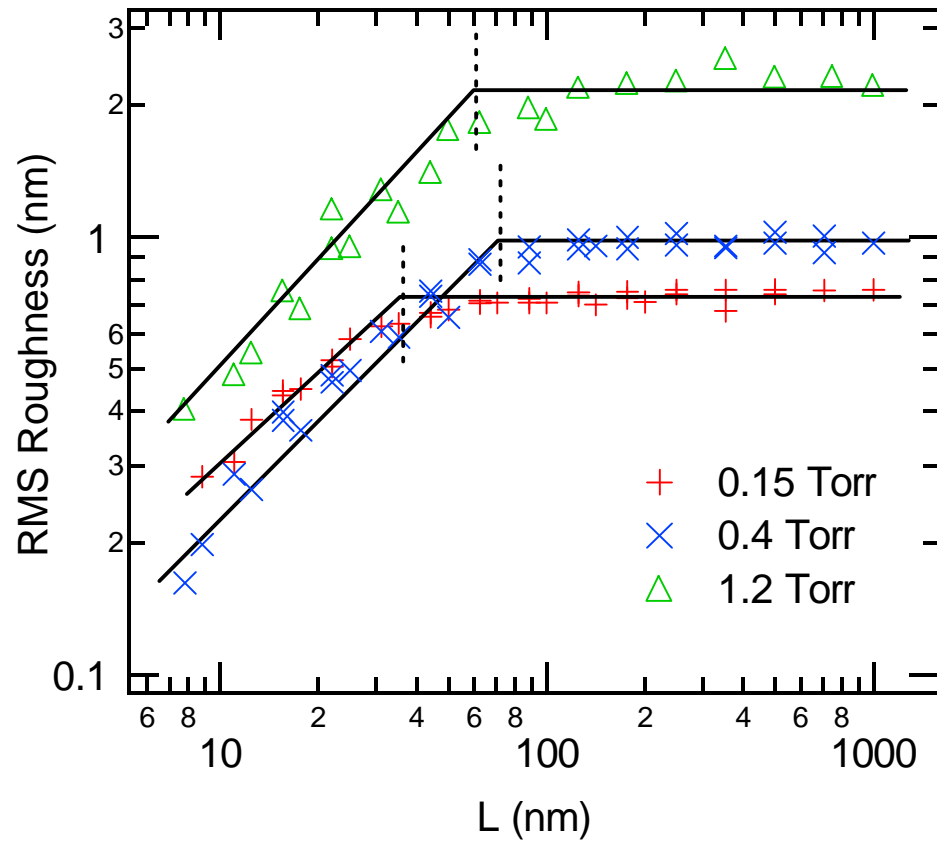


Fig. 4.1(b): Effect of Process Pressure. RMS Roughness vs. measurement length for various pressures.

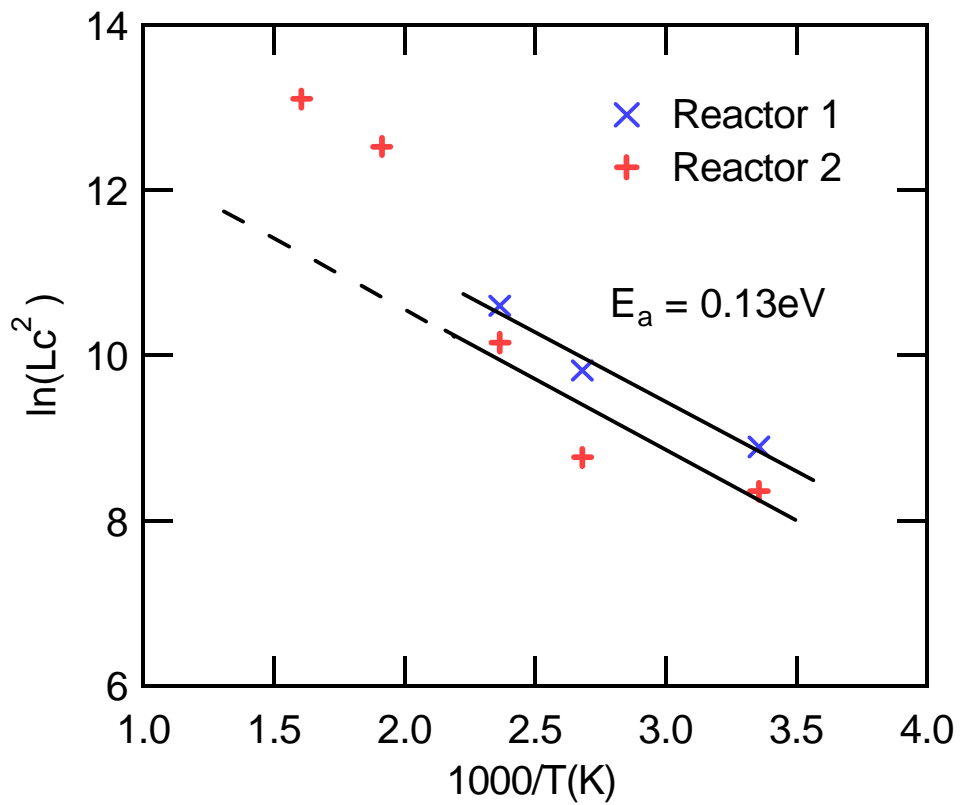


Fig. 4.2: Arrhenius plot of  $\ln(L_c^2)$  vs.  $1/T$  for films deposited from  $\text{SiH}_4/\text{H}_2$  in reactor 1 and reactor 2. Below  $150^\circ\text{C}$ , both processes show the same activation barrier. Films above  $150^\circ\text{C}$  in showerhead reactor show a shift in the activation barrier.

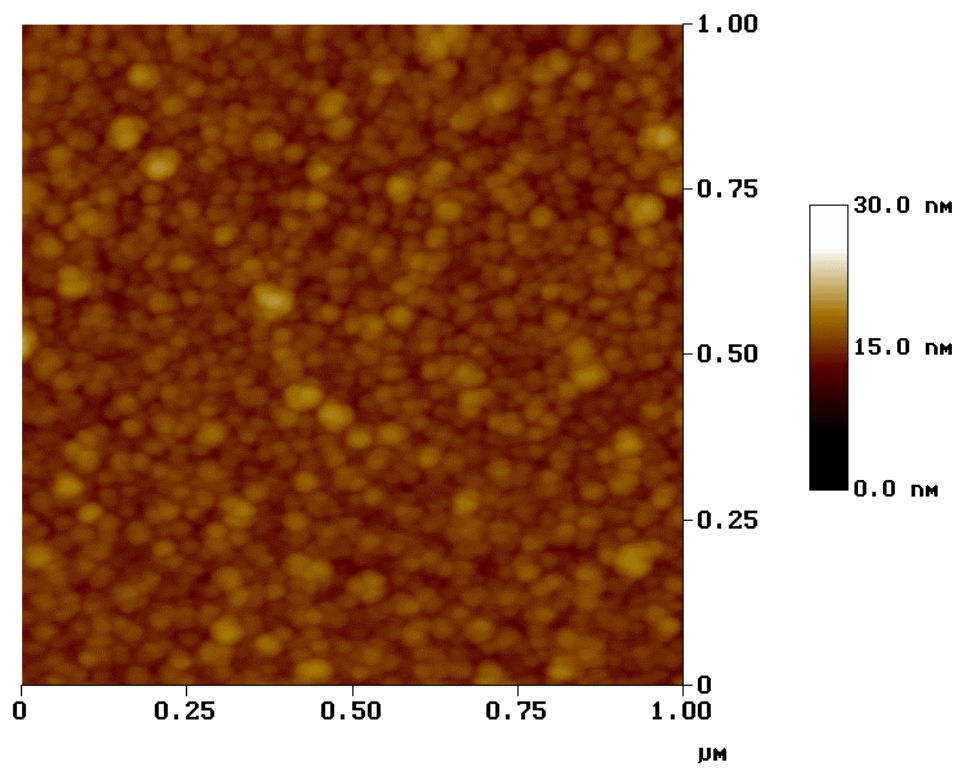


Fig. 4.3(a): Atomic force microscopy images of films deposited from pure  $\text{SiH}_4$  at  $150^\circ\text{C}$  in the showerhead reactor.

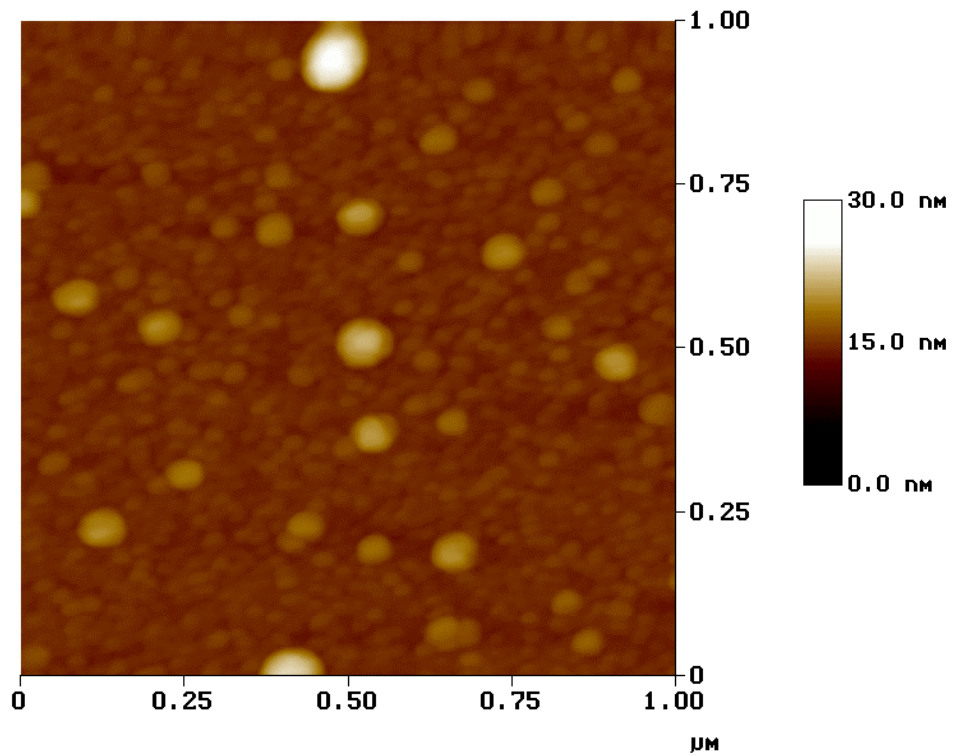


Fig. 4.3(b): Atomic force microscopy images of films deposited from pure  $\text{SiH}_4$  at  $350^\circ\text{C}$  in the showerhead reactor.

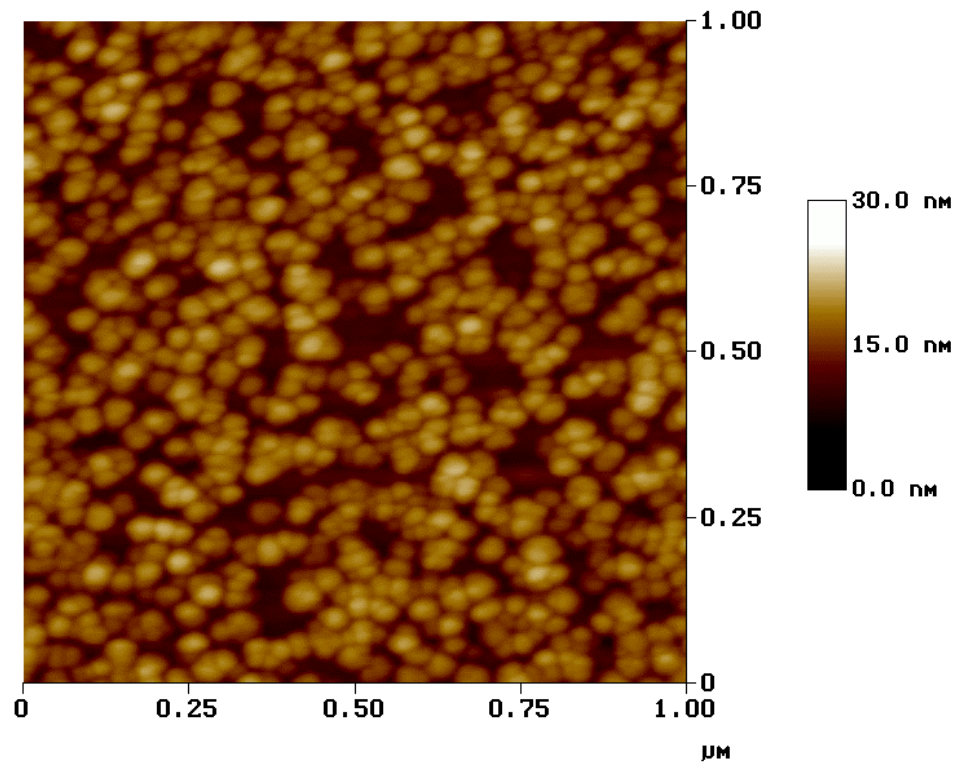


Fig. 4.4(a): Atomic force microscopy images of films deposited from  $\text{SiH}_4/\text{H}_2$  at  $150^\circ\text{C}$  in the showerhead reactor.

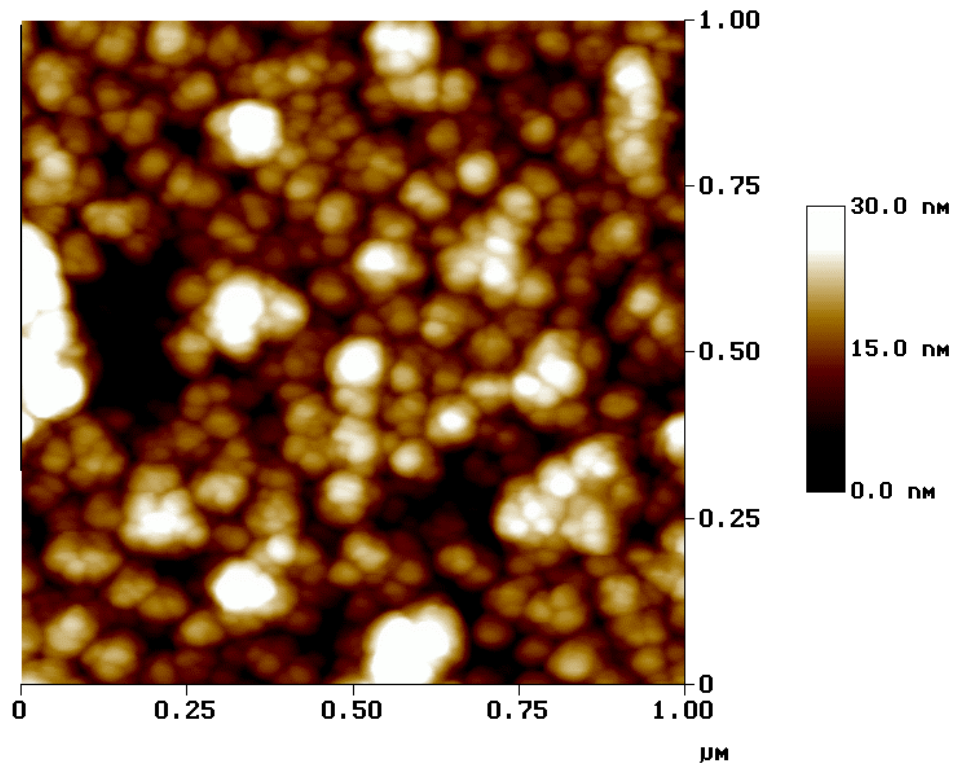


Fig. 4.4(b): Atomic force microscopy images of films deposited from  $\text{SiH}_4/\text{H}_2$  at  $350^\circ\text{C}$  in the showerhead reactor.

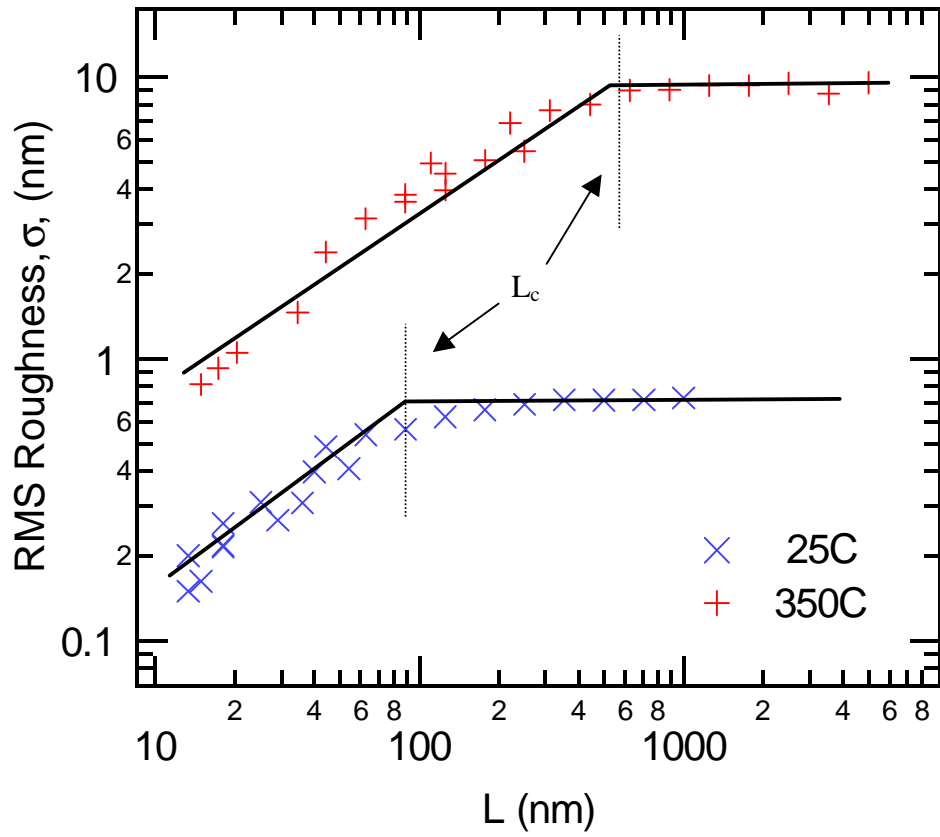


Fig. 4.5: RMS Roughness vs. measurement length for films deposited from  $\text{SiH}_4/\text{H}_2$  at 25°C and 350°C. Both films exhibit a static scaling coefficient of  $\alpha = 0.7$ , indicating the same transport mechanism dominates the growth process at both temperatures.

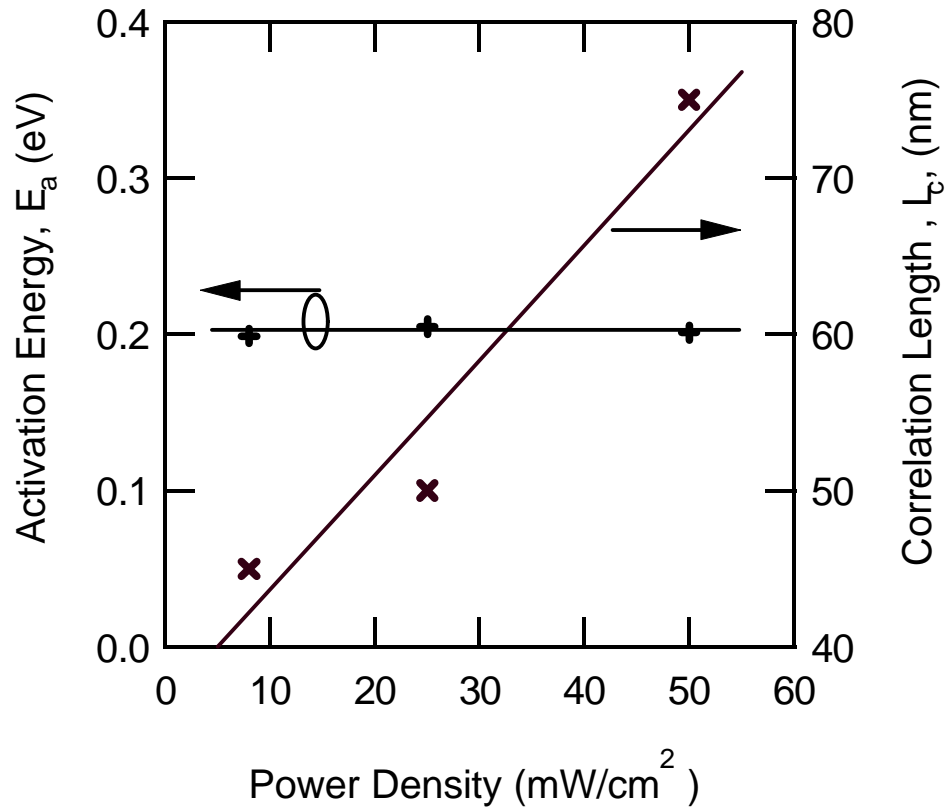


Fig. 4.6: Effect of RF Power Density. Activation barrier ( $E_a$ ) and Correlation Length ( $L_c$ ) vs. Power Density.  $L_c$  increases with increasing power, while  $E_a$  remains constant. The lines are guides to the eye.

*Chapter 5 is a draft of a manuscript to be submitted for publication.*

## **CHAPTER 5**

# **5 SUBSTRATE TEMPERATURE DEPENDENCE OF THE DYNAMIC SCALING COEFFICIENT DURING PLASMA DEPOSITION OF SILICON**

by: Kevin R. Bray and Gregory N. Parsons

*Department of Chemical Engineering, North Carolina State University, Raleigh NC  
27695-7905*

### **ABSTRACT**

Dynamic scaling has been used to characterize growth processes active during thin film deposition. Analysis of scaling parameters can be used to identify transport mechanisms active during growth and to extract kinetic information about transport pathways. Both the static and dynamic scaling coefficients reveal important information about the film growth. In this article, the dynamic scaling coefficient,  $\beta$ , is examined as a function of

substrate temperature for plasma deposited hydrogenated amorphous silicon. Analysis of images obtained by atomic force microscopy of surface topography is used to determine the dynamic scaling coefficient.  $\beta$  is found to be constant with temperature, with a value of  $\beta = 0.33$  over the range of 25°C to 300°C. These results are discussed in relation to a recent kinetic model of low temperature amorphous silicon growth.

## 5.1 INTRODUCTION

Hydrogenated amorphous silicon (a-Si:H) can be deposited as smooth, conformal films over a wide temperature range using plasma enhanced chemical vapor deposition (PECVD). The growth rate is non-thermally activated over a wide temperature range (<25 °C to < 400°C) [1-4]. These properties have motivated investigation into the growth mechanism and surface transport characteristics of a-Si:H. Analysis of the roughness evolution with film thickness and process conditions has been used to study the surface transport mechanisms that are active during PECVD deposition process [5-10].

Growth models based on thermodynamic properties apply only in the equilibrium limit. Current technological processes operate far from equilibrium, where kinetic processes dominate. Dynamic scaling [11, 12] gives insight into the kinetic processes dominating surface mechanisms. This approach produces the parameters,  $\alpha$ , the static scaling coefficient,  $\beta$ , the dynamic scaling coefficient and  $L_c$ , the lateral correlation length. The static scaling coefficient correlates how the surface roughness changes with the lateral area and the dynamic scaling coefficient describes how the surface roughness changes with film thickness or deposition time [5, 12]. Dimensional fractal analysis can be used to extract the scaling parameters. Dimensional analysis involves determining the root-mean-square (RMS) surface roughness ( $\sigma$ ) at various length scales ( $L$ ) and deposition times ( $t$ ), then obtaining scaling coefficients [5, 12, 13] using  $\sigma \sim L^\alpha$  and  $\sigma_{\text{sat}} \sim t^\beta$ , which are related to transport on the surface. Each transport mechanism leaves distinct imprints on the topography that are recognizable through fractal analyses [12].

Continuum models including linear and non-linear terms in the equations of motion are used to analyze surface roughness data to determine scaling coefficients under different conditions. Matching the experimentally determined scaling exponents with continuum growth models then identifies the primary transport mechanisms. Scaling coefficients for surfaces formed during random, stochastic growth  $\alpha$  is undefined and  $\beta = 0.5$  [11]. For the linear continuum model with surface transport dominated by surface diffusion, the scaling coefficients are expected to attain values of  $\alpha = 1$  and  $\beta = 0.25$  [11, 12, 14]. When nonlinear terms are included, scaling coefficients of  $\alpha = 0.67$  and  $\beta = 0.2$  are expected for diffusion [11]. For transport by evaporation and condensation [12], expected values are  $\alpha = 0$  and  $\beta = 0$ .

There are several studies involving the kinetic smoothing mechanisms of hydrogenated amorphous silicon deposited using plasma deposition [5-10]. Typically,  $\alpha$  is measured between 0.8 – 1 and  $\beta$  between 0.2 – 0.33, consistent with self-similar geometry and transport by surface diffusion. Other deposition processes have also been studied for amorphous silicon deposition. These differing techniques produce differing values for  $\beta$ . Sputter deposition of amorphous silicon produces a dynamic scaling coefficient of  $\beta = 0.41$  [15], similar to sputter deposition of gold on silicon which results in  $\beta = 0.40 - 0.42$  [16]. Thermal evaporation of amorphous silicon generates a value of  $\beta = 0.1$  [17]. There is general consensus that surface diffusion is smoothing the plasma deposited amorphous silicon films [5, 7-10]. Values of  $\beta$  lower than 0.5 are indicative of surface smoothing during growth [7, 9].

Several studies of dynamic scaling coefficients have produced coefficients that do not fit any of the transport models [7, 9, 10, 15, 17, 18]. There are different reasons why

this could occur. Two separate processes might be competing on the surface. In this case, the scaling coefficients would be a crossover between the two predicted values. The theoretical coefficients that match most closely to the experimental results are assumed to dominate. Tanenbaum et. al. believe chemical potential-driven precursor diffusion is occurring on the surface during their experiments although the scaling coefficients measured are lower than predictions for surface diffusion [10]. Another possibility is the analysis is not applicable to the growth process being studied. Dynamic scaling does not apply to deposition under all conditions [5]. Switching the diluent gas from helium to argon for a-Si:H deposition caused a change in the scaling properties of the film, indicating the surface processes were distinctly different. This may be due to ion bombardment which is not accounted for in the continuum models used to predict the scaling coefficients.

Two different interpretations of the amorphous silicon growth process have developed from the dynamic scaling analysis. First, from our previous work, we have concluded that smoothing during amorphous silicon growth proceeds through surface diffusion of a physisorbed precursor state [5, 19]. Second, Smets et. al. propose that smoothening occurs through the diffusion of a chemisorbed species, similar to mechanisms found in molecular beam epitaxy (MBE) [7, 18]. In our previous work, the static and dynamic scaling coefficients were extracted from roughness data and shown to be consistent with surface diffusion [5]. Experiments focused on the temperature dependence of the lateral correlation length, and used this parameter to extract diffusion barriers from the scaling data [5, 19]. The correlation length is a measure of distance across a surface that roughness correlations persist [5, 12]. The correlation length

increased with temperature with a low barrier. These results have been related to the diffusion of adsorbed precursor species across the surface with a low diffusion barrier [5]. The physisorbed configuration has not been identified specifically, although the ‘three-centered’ bond configuration suggested in earlier models does not exist [20]. A recent kinetic model for amorphous silicon growth has been constructed and it correlates closely with observed experimental trends [21].

Work by Smets et. al. [7] has focused on the temperature dependence of  $\beta$  and have used this parameter to determine growth kinetics. Their interpretation of their results is predicated on the assumption that the random diffusion of physisorbed radicals leads to random hydrogen abstraction from the surface to create dangling bond. These random dangling bonds cannot lead to the smooth surfaces observed in amorphous silicon growth [22]. Therefore a chemisorbed species is responsible for smoothening during film growth. Films deposited using an expanding thermal plasma show that  $\beta$  decreases with increasing substrate temperature [7]. This data is fit to a model for film growth and activation barriers are extracted from the model. The model resulted in an activation energy of 0.7 eV for a free atom and a binding energy per bond of 0.3 eV [7]. Similar models have been developed for MBE growth [11, 23]. A high diffusion barrier represses diffusion at low temperatures and the deposition appears random with  $\beta = 0.5$ . As the temperature increases, weakly bound species begin to diffuse, lowering  $\beta$ . At sufficiently high temperatures,  $\beta$  reaches the value for surface diffusion. At even higher temperatures, the desorption energy can be overcome, and evaporation/condensation occurs on the surface with  $\beta = 0$ .

In this work, we calculate the dynamic scaling coefficient over a wide range of substrate temperatures and compare our results with the work of Smets et. al.

## **5.2 EXPERIMENTAL METHOD**

In this article, the dynamic scaling coefficient is determined from dimensional analysis of amorphous silicon films deposited at temperatures ranging from 25°C to 400°C. Films were deposited by plasma enhanced chemical vapor deposition from mixtures of silane and helium and pure silane in two different reactor systems [24, 25]. The shortest times analyzed were 1 minute for 25°C, and 30 seconds for > 100°C. Amorphous silicon deposited at these times has coalesced [5]. Roughness measurements of thinner uncoalesced films do not represent true saturated roughness values and should not be used in determining  $\beta$  [5]. Surface topography of the deposited films was characterized by atomic force microscopy. AFM scan sizes of 1  $\mu\text{m}$  x 1  $\mu\text{m}$  were used to obtain the saturated RMS roughness values. All AFM measurements were performed under ambient conditions.

## **5.3 RESULTS AND DISCUSSION**

Results of the dimensional analysis are shown in Fig. 5.1, where the saturated RMS roughness is plotted vs. deposition time for a-Si:H films deposited from 25°C to 400°C. The dynamic scaling coefficient can be extracted from these plots. Figure 5.2(a) is a plot of the dynamic scaling coefficient vs. substrate temperature for the coefficients

extracted from Fig. 5.1 and other films deposited using PECVD in the literature.  $\beta$  is approximately constant with substrate temperature. From Fig. 5.1, it can be shown that the static scaling coefficient remains constant to 300°C with a value of  $0.33 \pm 0.02$ . Between 300°C to 400°C,  $\beta$  increases sharply. This temperature corresponds to a rapid decrease in the correlation length due to thermal hydrogen desorption on the surface [21, 26]. The decrease in hydrogen coverage leads to a decrease in diffusion on the surface [21]. A similar increase in  $\beta$  with hydrogen desorption has been observed previously [9]. The result that  $\beta$  is independent of temperature and previous measurements that  $\alpha$  is independent of temperature [5] suggest that the growth mechanism for a-Si:H is temperature independent until the H<sub>2</sub> desorption temperature. The change observed in  $\beta$  at 400°C is consistent with a different growth process above the H<sub>2</sub> desorption temperature.

There are differences between this data and the work of Smets et. al. [7]. Figure 5.2(b) show a plot of  $\beta$  vs. substrate temperature reported in Ref. [7]. The dynamic scaling coefficient is seen to decrease with increasing temperature. The a-Si:H deposition tools were different in the two processes. Our experiments show consistency between two differently configured capacitively coupled direct plasma systems [19], but growth in other non-direct plasmas systems may not follow the same transport mechanisms. Differences in plasma power, electrode spacing and process pressures are known to change the gas composition in plasma processing [3, 27-29]. In reference [7], an expanding thermal plasma (ETP) was used. A remote thermal argon/hydrogen plasma was generated and the silane precursor was injected into the plasma. The substrate was located ~35 cm from the silane injection point. Ion contribution to the growth was

estimated between 6 – 9%. Spectroscopic ellipsometry was used to measure film roughness and  $\beta$  was calculated for each sample instead of a fit from a series of samples. The presence of Ar and H<sub>2</sub> in the plasma may also have altered the deposition process. Switching from helium to argon dilution during a-Si:H deposition was shown to change the surface transport characteristics and alter the scaling coefficients [5]. Hydrogen dilution has also been shown to change the kinetics of a-Si:H growth [19]. Although a remote plasma was utilized, some effects from the process gases may have influenced the measurements. The process gases may have also effected our measurements. Increased ion bombardment has been seen to increase the correlation length, although the scaling coefficients and diffusion barriers remain constant [26].

The measurement technique is another variable that is different between our work and Smets et. al. Our  $\beta$  values were measured using ex-situ AFM to calculate roughness for a time series of depositions. Smets used in-situ ellipsometry to measure roughnesses evolution of individual samples. To avoid nucleation effects on the roughness, only roughness data for films thicker than 100 nm was used by Smets et. al. to determine  $\beta$  [18]. This generally resulted in less than one order of magnitude in thickness utilized for the fit. This small data range may lead to variations in the measurements. We utilized approximately two orders of magnitude in thickness in our measurements.

The growth rates in Ref [7] may also contribute to the different  $\beta$  values observed. High growth rates are used and this is expected to lead more tri-hydride bonding on the surface. Our kinetic model for amorphous silicon growth proposes that it is more difficult for incoming silicon radical to diffuse on a tri-hydride surface compared to a mono-hydride surface [21]. Increasing growth rates also decrease the reaction time for

mobile species on the surface and at high growth rates may result in short diffusion lengths. This suggests that the deposition process observed in Ref [7] may not be the same as we are observing in our experiments.

## **5.4 CONCLUSIONS**

We believe the results presented have important implications for understanding and describing plasma deposited amorphous silicon. In our direct plasma CVD configurations, the dynamic scaling coefficient is constant with substrate temperature. This result is consistent with the diffusion of weakly bound physisorbed radicals on the surface controlling the surface topography. Growth conditions such as deposition rate, diluent gases, and plasma characteristics and process conditions such as chamber configuration may change the transport regime on the surface during growth. Novel plasma configurations that differ from traditional direct plasma deposition may also result in changes in the surface transport during growth.

## **5.5 ACKNOWLEDGEMENTS**

This work was supported under NSF Grant No. 0072784 and DARPA.

## 5.6 REFERENCES

- [1] A. Matsuda, *Journal of Non-Crystalline Solids*, **59-60**, 767 (1983).
- [2] A. Matsuda, *Plasma Physics and Controlled Fusion*, **39**, 431 (1997).
- [3] J. Perrin, M. Shiratani, P. Kae-Nune, H. Videlot, J. Jolly, and J. Guillon, *Journal of Vacuum Science and Technology A*, **16**, 278 (1998).
- [4] J. Robertson, *Journal of Applied Physics*, **87**, 2608 (2000).
- [5] K.R. Bray and G.N. Parsons, *Physical Review B*, **65**, 035311 (2002).
- [6] A.J. Flewitt, J. Robertson, and W.I. Milne, *Journal of Applied Physics*, **85**, 8032 (1999).
- [7] A.H.M. Smets, D.C. Schram, and M.C.M. van de Sanden, *Materials Research Society Symposium Proceedings*, **609**, A7.6.1 (2000).
- [8] K. Ikuta, Y. Toyoshima, S. Yamasaki, A. Matsuda, and K. Tanaka, *Material Research Society Symposium Proceedings*, **420**, 413 (1996).
- [9] M. Kondo, T. Ohe, K. Saito, T. Nishimiya, and A. Matsuda, *Journal of Non-Crystalline Solids*, **227-230**, 890 (1998).
- [10] D.M. Tanenbaum, A.L. Laracuente, and A. Gallagher, *Physical Review B-Condensed Matter*, **56**, 4243 (1997).
- [11] A.L. Barabasi and H.E. Stanley, *Fractal Concepts in Surface Growth* (Cambridge UP, Cambridge, 1995).
- [12] W.M. Tong and R.S. Williams, *Annual Review of Physical Chemistry*, **45**, 401 (1994).

- [13] P. Meakin, *Fractals, scaling and growth far from equilibrium*. (Cambridge UP, Cambridge, 1998).
- [14] W.U. Schmidt, R.C. Alkire, and A.A. Gewirth, *Journal of the Electrochemical Society*, **143**, 3122 (1996).
- [15] T. Karabacak, Y.-P. Zhao, G.-C. Wang, and T.-M. Lu, *Physical Review B*, **64**, 085323 (2001).
- [16] H. You, R.P. Chiarello, H.K. Kim, and K.G. Vandervoort, *Physical Review Letters*, **70**, 2900 (1993).
- [17] M. Lutt, J.P. Schlomka, M. Tolan, J. Stettner, O.H. Seeck, and W. Press, *Physical Review B-Condensed Matter*, **56**, 4085 (1997).
- [18] M.C.M. van de Sanden, A.H.M. Smets, and W.M.M. Kessels, *Materials Research Symposium Proceedings*, **715**, A15.1 (2002).
- [19] K.R. Bray, A. Gupta, and G.N. Parsons, *Applied Physics Letters*, **80**, 2356 (2002).
- [20] A. Gupta, H. Yang, and G.N. Parsons, *Surface Science*, **496**, 307 (2002).
- [21] A. Gupta, K.R. Bray, and G.N. Parsons, unpublished.
- [22] W.M.M. Kessels, A.H.M. Smets, D.C. Marra, E.S. Aydil, D.C. Schram, and M.C.M. van de Sanden, *Thin Solid Films*, **383**, 154 (2001).
- [23] P.I. Tamborenea and S. Das Sarma, *Physical Review E*, **48**, 2575 (1993).
- [24] E. Srinivasan, D.A. Lloyd, and G.N. Parsons, *Journal of Vacuum Science and Technology A*, **15**, 77 (1997).
- [25] C.S. Yang, W.W. Read, C. Arthur, E. Srinivasan, and G.N. Parsons, *Ieee Electron Device Letters*, **19**, 180 (1998).
- [26] K.R. Bray and G.N. Parsons, unpublished.

- [27] O. Leroy, G. Gousset, L.L. Alves, J. Perrin, and J. Jolly, *Plasma Sources Science & Technology*, **7**, 348 (1998).
- [28] E.A.G. Hamers, A.F.I. Morral, C. Niikura, R. Brenot, and P.R.I. Cabarrocas, *Journal of Applied Physics*, **88**, 3674 (2000).
- [29] S. Ramalingam, D. Maroudas, and E.S. Aydil, *Journal of Applied Physics*, **86**, 2872 (1999).

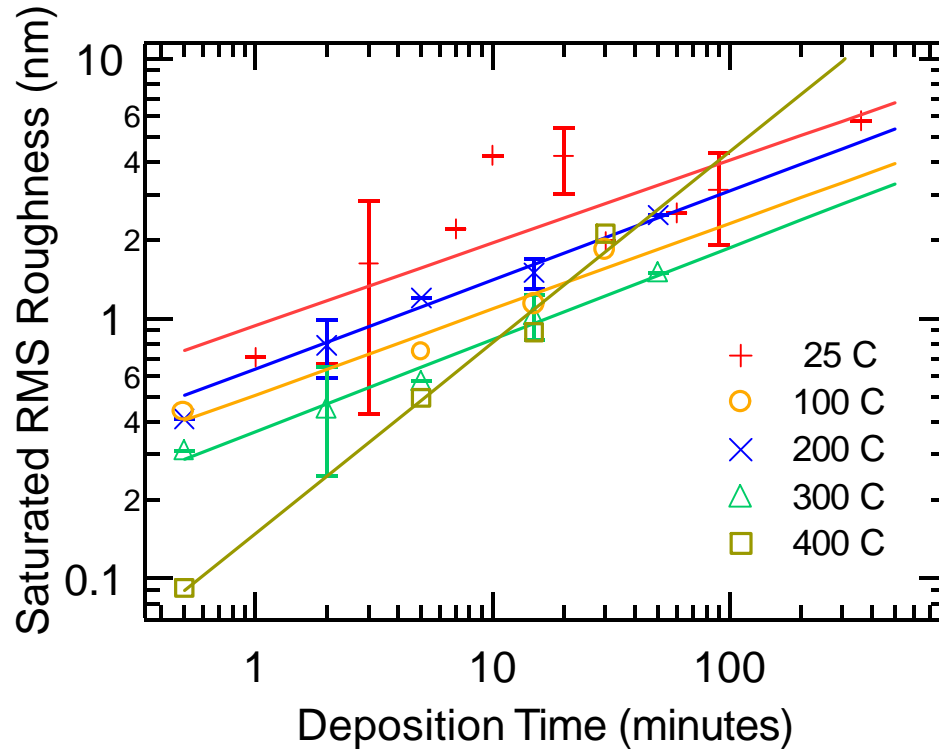


Fig. 5.1. Saturated RMS Roughness vs. deposition time for films deposited from 25°C to 300°C. Dynamic scaling coefficient,  $\beta$ , is extracted from a best fit of the data.

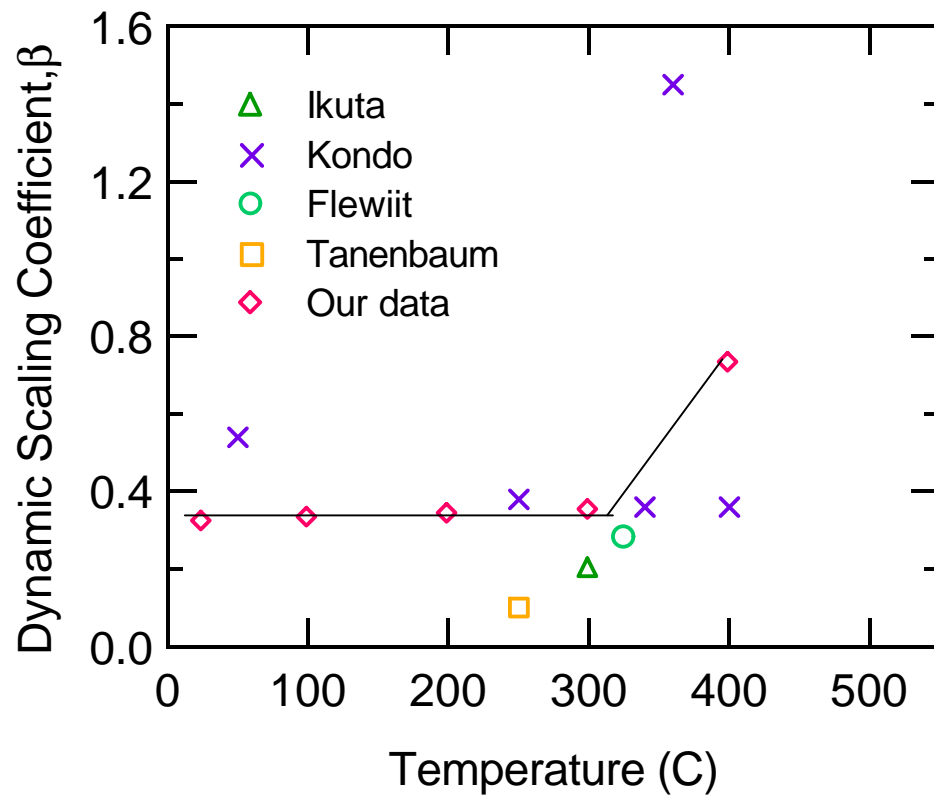


Fig. 5.2(a): Dynamic scaling coefficient,  $\beta$ , vs. substrate temperature. Includes data from Figure 5.1 and previously published data from the literature for RFPECVD amorphous silicon deposition. The line is a guide to the eye.

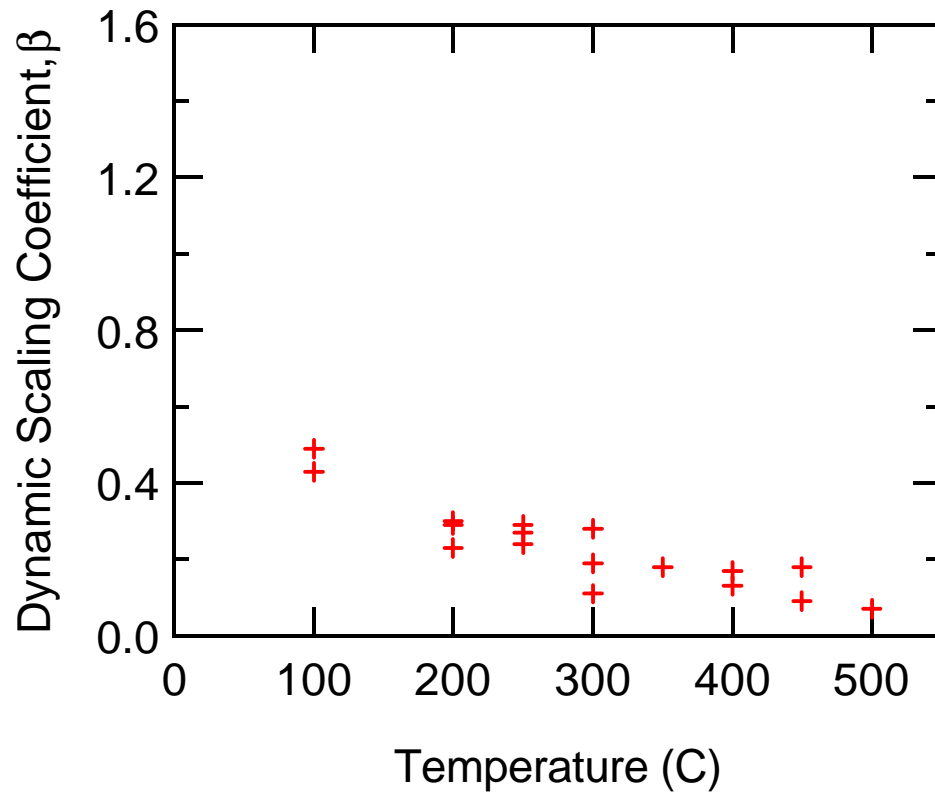


Fig 5.2(b): Dynamic scaling coefficient,  $\beta$ , vs. substrate temperature from Ref. [7] for expanding thermal plasma deposition of amorphous silicon.

*Chapter 6 is a draft of a manuscript to be submitted for publication.*

## **CHAPTER 6**

# **A SURFACE HYDRIDE-DEPENDENT PRECURSOR DIFFUSION MODEL FOR LOW TEMPERATURE AMORPHOUS SILICON DEPOSITION**

Atul Gupta, Kevin R. Bray and Gregory N. Parsons

Department of Chemical Engineering, North Carolina State University, Raleigh, NC  
27695-7905

### **ABSTRACT**

A quantitative kinetic model for low temperature hydrogenated amorphous silicon film deposition is presented. The model includes a new valence balance approach used in combination with site balance equations to describe Si-Si bond formation on the growth surface. The model describes precursor physisorption, diffusion, as well as direct chemisorption and insertion into Si-Si bonds as a function of surface temperature and radical flux. Several macroscopic parameters, including precursor surface reaction

probabilities, film growth rate, and surface precursor diffusion length are calculated, and values agree reasonably with available experimental results. A novel feature of the model is the hypothesis that the kinetic barrier to surface silyl diffusion depends on the local structure of the hydrogenated surface, where the transport barrier for silyl diffusion on a monohydride terminated surface is smaller than that for transport on di- and tri-hydride terminated surface regions. The model results in an apparent activation energy of  $\sim 0.2\text{eV}$  for precursor surface diffusion under typical growth rate conditions ( $\sim 1\text{\AA}/\text{s}$ ), consistent with experimental results. This model therefore provides a means for silicon network formation not present in most other models. That is, Si-Si bond formation can proceed between two neighboring silicon hydrides, and  $\sim 90\%$  of these bonds will not be affected by further surface reaction and will remain in the film.

**Keywords:** Growth mechanism, Surface composition, Network formation, Morphology evolution, Diffusion length, Surface reactions

## 6.1 INTRODUCTION

A fundamental understanding of the growth processes that control film properties such as defect densities, topology evolution and crystallite fraction is critical for optimizing plasma activated processes such as plasma enhanced chemical vapor deposition (PECVD), reactive ion etching (RIE) and plasma surface treatment of different materials. Here we focus on the plasma deposition of hydrogenated amorphous silicon (a-Si:H) films deposited using silane/hydrogen mixtures, used for several important applications in photo-voltaic devices and thin film transistors (TFTs) [1]. The mechanisms controlling defect generation, crystallization and topology evolution during low temperature (<400°C) deposition of a-Si films and the effect of process variables as temperature and radical fluxes are discussed in terms of a new quantitative kinetic growth model that explains a broad range of experimental observations.

The primary step towards developing a growth model is to identify the important radicals/species generated in the plasma as well as the surface transport process that control film deposition. For device quality (i.e., low defect density) a-Si:H films deposited from Silane(SiH<sub>4</sub>)/Hydrogen(H<sub>2</sub>) gas mixtures it is believed that the silyl radical (SiH<sub>3</sub>) is the primary growth precursor [2, 3], although it is known that other species may contribute toward a-Si:H growth depending on plasma conditions (RF power density, pressure, electrode spacing) [4-7]. SiH<sub>3</sub> is an important part of the growth and is considered to have a high surface mobility, contributing to the observed conformal

smooth surfaces. An enhanced understanding of idealized a-Si:H growth from SiH<sub>3</sub> will improve our ability to understand more complicated growth mechanisms.

Hence the deposition parameters described in this article are limited to the conditions where silyl radicals are the dominant growth precursors. Recent experiments monitoring the surface topology evolution using Atomic Force Microscopy (AFM) of plasma deposited a-Si:H films indicate that surface diffusion of the physisorbed precursors dominates film growth [8, 9]. Gallagher et al [10], Perrin et al [3], Ganguly and Matsuda et al [11-14] have proposed growth models based on dominant surface diffusion of physisorbed precursors. These models were later modified by Guizot et al [15] and Maeda et al [16] to further explain hydrogen dilution and network formation effects respectively. The surface diffusion growth models involve physisorption of the growth precursors, which may then diffuse around on the surface and get chemisorbed upon reaching a dangling bond site on the surface. The dangling bonds in turn are created via a two-step growth process wherein the physisorbed radicals first abstract a surface hydrogen atom creating a dangling bond onto which other precursor radicals may chemisorb. While this picture is quite simplistic, there is much debate over dominant reaction mechanisms as well as the physisorption state of the radicals. The physisorption of the SiH<sub>3</sub> radical precursors on H-terminated Si sites is often proposed to proceed through a three-centered Si –H–Si linkage [4, 17]. In this model, this three-center bond structure needs to be sufficiently stable for the physisorbed silyl radical to achieve reasonable surface coverage at temperatures near 200°C, but is also sufficiently weak to allow the silyl radical to diffuse with a relatively small activation barrier (~0.2 eV) on the surface. However, recent *ab-initio* and molecular dynamics simulations indicate that the

3-center bond may not be the most “stable” configuration for the physisorbed precursor [7, 18] and suggest that the precursor radical physisorbs on the surface in some other configuration that enables bonding and transport that follow the observed surface diffusion kinetics. In addition to the debate over a “stable” physisorbed state, other reactions have been identified as possible important growth pathways. Specifically, von Keudell et al. have reported experimental evidence for direct insertion of the  $\text{SiH}_3$  radicals into strained Si-Si bonds [19] using *in-situ* IR measurements of the interactions between  $\text{SiH}_3$  radicals and a deuterated (a-Si:D) film. Also, Dewarrat and Robertson [Dewarrat, 2001 #37] have recently suggested an alternate mechanism for silyl adsorption, involving a displaced surface hydride and formation of a weakly adsorbed radical.

Recent developments in experimental surface analysis techniques have enabled direct measurements of the surface species present during the growth. Yamasaki et al [20-22] have been able to measure the surface dangling bond concentrations during a-Si:H deposition using time-resolved Electron Spin Resonance techniques, and report a monotonic increase in the surface dangling bond density with deposition temperature. Based on these observations, Robertson further argued that the film properties (especially Hydrogen elimination from the films) might be determined by bulk processes rather than surface reactions [23]. However van de Sanden et al [24] have pointed out that direct abstraction reactions by silyl and H radicals may provide other pathways for  $\text{H}_2$  elimination and still have the deposition process dominated by surface reactions. It is therefore imperative to understand how the surface composition changes under various deposition conditions.

Marra et al [25] and later Kessels et al [26] have measured the distribution of the mono-, di- and tri-hydride sites on the growing amorphous silicon surface using *in-situ* Attenuated Total Reflection Fourier Transform Infrared Spectroscopy (ATR-FTIR). These changes in the surface composition and site distribution with deposition temperature may be key to understanding the hydrogen elimination processes as well as the dominant growth mechanisms. Another limitation in models developed to date arises from the fact that these models use only site balances where the sites are distinguished based on the number of Si-H bonds or dangling bonds on a particular surface Si atom. With this type of surface site balance it is difficult to explain the formation of a network comprising of Si-Si bonds which is critically important in understanding the transformation from amorphous silicon to microcrystalline regime. Maeda et al have tried to address this issue [16] but their model is based on the bulk SiH and SiH<sub>2</sub> groups rather than the surface concentrations of these hydrides.

The kinetic model described in the following section is different from previous models in the following key aspects: i) it specifically includes silyl insertion; ii) it presents a new valence balance approach (in conjunction with the site balance equations) to explain the network formation on the surface and to quantify bond-specific reactions (e.g., the insertion of SiH<sub>3</sub> radicals in strained Si-Si bonds); iii) it includes silyl physisorption, but it is independent of the detailed structure of the adsorption state; and iv) it maintains consistency with surface diffusion models by presenting a diffusion activation barrier that depends on surface mono-, di- and tri-hydride composition. Using this model, we are able to understand various aspects (defect densities, network

formation, surface distribution of hydrides and topology evolution) of the films grown under different deposition conditions.

The valence balance approach is presented in Section 6.2.1. Section 6.2.2 presents key surface reactions involving radicals and active surface sites, and a reaction scheme is developed. The steady state site balance equations are presented in Section 6.2.3, and the predicted results obtained from the model are compared with known experiments in Section 6.2.4. In Section 6.3 important macroscopic growth parameters are extracted from the microscopic reaction rates developed in Section 6.2, and these parameters are compared with available experimental results.

## **6.2 KINETIC MODEL**

### **6.2.1 Valence Balance for the Surface Atoms**

Most earlier kinetic models have assumed the growth surface of a-Si:H films to be comprised of different types of surface sites. These sites include dangling bonds, surface hydrides (mono-, di- and tri-hydrides), and physisorbed precursors. The drawback in such a description of the surface is that each of the surface sites is limited to having just one type of bond and consequently some surface reactions that involve precursor reactions with specific types of bonds cannot be adequately accounted for. Such reactions are referred as “bond-specific” reactions and could include for example, the insertion of radicals into Si-Si bonds present on the surface. Bond-specific reactions may be accounted for through a “valence” or bond balance equation for the surface atoms. In

the valence balance, each surface Si atom makes one bond to a bulk silicon atom (Si atom in the layer below the surface layer) and three other bonds. These other bonds may be dangling bonds, Si-H bonds, Si-Si bonds, or any combination of the three.

The valence balance for the surface atoms is developed as follows: Assume that there are  $N$  tetrahedrally coordinated Si atoms on the surface (per unit area) prior to the start of the deposition with a total of  $4N$  bonds. These  $4N$  bonds are comprised of dangling bonds ( $N_d$ ), Si-H bonds ( $N_h$ ) and Si-Si bonds ( $N_{Si}$ ). The Si-Si bonds may either be to bulk Si atoms (denoted as  $N_b$ ) or could be between two surface Si atoms (denoted as  $N_s$ ). Each Si atom on the surface has to form at least one Si-Si bond with the bulk Si atoms to be considered a contiguous part of the film (hence  $N_b = N$ ). This reduces the number of “available” valences by  $N$ . Also the surface Si-Si bonds ( $N_s$ ) share two valences of the surface atoms and therefore need to be counted twice in the bond-balance. It is expected that under many conditions, for example significant di-hydride coverage, that silicon surface atoms will have on average more than one Si-Si bond. It is presumed here that the presence of a dangling bond on an atom dominates the energetics and kinetics of that surface atom, rendering the other surface bonds on that atom effectively unreactive. In other words, each dangling bond effectively counts as 3 surface valences. As a simplified example, the model assume that if a silyl approaches a dangling bond site where the Si atom has one dangling bond, one Si-H bond, and two Si-Si bonds, the probability of silyl insertion into the Si-Si bond, or silyl abstraction of the H atom, is zero because of the relative high reactivity of the dangling bond.

The valence balance is therefore written:

$$3N = 3N_0 + N_h + 2N_5 \quad (1)$$

During the deposition, there are physisorbed radicals (surface coverage =  $N_4$ ) on the surface that mask some of the surface atoms from the direct impact of the incident radicals. Each physisorbed silyl radical is assumed to mask exactly one Si atom on the surface (hence a loss of 4 available bonds) but it also makes a weak bond with the surface that may undergo other reactions (an addition of 1 available bond), therefore resulting in a net reduction of  $3N_4$  bonds on the surface. This modifies the bond balance as:

$$3N = 3N_0 + N_h + 2N_5 + 3N_4 \quad (2)$$

which upon normalizing with respect to the total number of valences ( $4N$ ) gives:

$$0.75q_0 + q_h + 2q_5 + 0.75q_4 = 0.75 \quad (3)$$

Here  $q_0$  and  $q_4$  are the fractional site coverages for the dangling bonds and physisorbed radicals respectively (defined as  $N_0/N$  and  $N_4/N$  respectively) while  $q_h$  and  $q_5$  are the surface Si-H and Si-Si bond fractions (defined as  $N_h/4N$  and  $N_5/4N$  respectively). The total number of variables needed to be solved for in this valence balance approach is limited to the 4 different types of bonds on the surface (dangling bonds, Si-H bonds, Si-Si bonds and weak bonds between the physisorbed radicals and surface atoms). If the bond-balance approach is to be used independently, all reactions need to be described in terms of interactions between different bonds and not as interactions of precursors with different surface sites. This is possible only if all like bonds were equivalent in terms of chemical reactivity and all reactions were site independent, which implies that the

location of the various bonds on the surface does not influence the probability of any of the surface reactions. However, some of the surface reactions are site-specific (i.e. they depend on the particular location of bonds on the surface sites). For example the recombination of hydrides (an important hydrogen elimination step) requires two Si-H bonds to be present on neighboring surface silicon atoms. Description of such surface reactions requires a “site balance” approach that accounts for different surface sites involved in the reactions. Hence in order to describe all types of surface interactions, whether they are bond-specific like the insertion of radicals into Si-Si bonds, or site-specific like the recombination of surface hydrides, a combination of both the “site balance” and “valence balance” approaches must be used.

### 6.2.2 Overall Site Balance Equation for the Surface Atoms

The overall site balance equation is developed to describe the site-specific surface reactions. Various types of sites may be present on the growth surface, these include mono-, di- and tri-hydrides; dangling bond sites and physisorbed radicals. In addition to dangling bonds and the physisorbed radical sites on the surface (fractional site densities =  $q_0$  and  $q_4$  respectively), the silicon atoms may be bonded as mono-, di- or tri- hydrides with fractional site densities of  $q_1$ ,  $q_2$  and  $q_3$  respectively. These fractional coverages are constrained so that the sum of all fractional site coverages equals unity.

$$q_0 + q_1 + q_2 + q_3 + q_4 = 1 \quad (4)$$

Thus there are a total of 7 variables ( $q_0$ ,  $q_h$ ,  $q_1$ ,  $q_2$ ,  $q_3$ ,  $q_4$  and  $q_5$ ) in the two constraint equations (the valence and the site balance equations (3) and (4)) that need to be solved for simultaneously. The total hydrogen content on the surface ( $q_h$ ) is further related to the mono, di- and tri-hydride fractions designated as  $q_1$ ,  $q_2$ , and  $q_3$  (=site density/total sites,  $N$ ) respectively as follows:

$$0.25q_1 + 0.5q_2 + 0.75q_3 = q_h \quad (5)$$

This equation states that if, for example, the surface is completely covered by tri-hydride units, i.e.  $q_3 = 1$ , then  $q_h = 0.75$  corresponding to each of the Si atoms on the surface having three out of four available bonds as Si-H bonds (the remaining bond being a network Si-Si bond that binds the units to the underlying layer). In order to get the remaining site balances, the individual surface reactions leading to creation and consumption of the different surface sites need to be identified and quantified. The important surface reactions influencing the surface coverage of different sites during silicon deposition and the resulting site balance equations for the dangling bonds, physisorbed radicals, mono- and di-hydride site balances are discussed in the next two subsections.

### 6.2.3 Surface Reactions

This model focuses on deposition conditions that are known to result in good quality a-Si:H films from activated deposition processes where the incident radical flux is comprised primarily of silyl radicals. Surface reactions may occur either directly

between the incident radicals and surface bonds/sites (through Eley-Rideal, E-R, mechanisms) or between different species on the surface (Langmuir-Hinshelwood, L-H, mechanisms). The reactions involving the incoming radicals are quantified as the product of: 1) a reaction probability; 2) the radical flux  $\mathbf{f}_{\text{Si}}$ , defined as the flux of  $\text{SiH}_3$  radicals per unit surface site density ( $\mathbf{f}_{\text{Si}} = \text{radicals per surface site, per second}$ ); and 3) the fractional surface coverage of the species involved,  $\mathbf{q}_x$  (where  $x = 0, 1, 2, 3, 4$  or  $5$ ). The L-H type surface reactions are expressed as a product of: 1) the reaction rate constant,  $\mathbf{u}_n$  (listed on Table 1); and 2) the product of the fractional surface coverage of the relevant species,  $\mathbf{q}_x$  and  $\mathbf{q}_y$  (where  $x, y = 0, 1, 2, 3, 4$  or  $5$ ). The individual surface reaction rate constants,  $\mathbf{u}_n$ , are expressed in terms of an Arrhenius expression with a pre-exponential frequency factor  $A_n$  and an activation energy term,  $E_n$ . The values of  $A_n$  are chosen as  $k_B T/h$  (as predicted by the transition state theory) for these reactions (where  $k_B$  is the Boltzmann constant,  $h$  is Planck's constant, and  $T$  is the substrate temperature in Kelvin). The values for  $E_n$  are taken from experimental and theoretical reports in the literature wherever available and are described and tabulated below along with the individual surface reactions.

Table 6.1(a) enlists the reactions considered, the corresponding rate parameters, and the rate expressions used in the model. First consider the possible reactions for the incident silyl radicals as shown in Reactions A-D (Table 6.1). Molecular dynamics simulations predict that the silyl radicals impinging on the surface with the dangling bond pointed towards the surface are more likely to participate in reactions than in other configurations [7]. In this configuration, the incident  $\text{SiH}_3$  radicals may directly

chemisorb on a dangling bond (Reaction A) forming a surface tri-hydride. This elementary addition reaction is barrier free and is assigned a probability of  $s_0=0.25$  corresponding to the approximate fraction surface area of a dangling bond on a  $\text{SiH}_3$  radical. The silyl radical is also presumed to physisorb easily on the surface, resulting in a net addition to the number of physisorbed radicals on the surface (Reaction B), but a detailed bond configuration is not presumed, nor is it critical for the model presented here. Again the probability for this reaction is primarily determined by the orientation of the dangling bond (db) on the incoming  $\text{SiH}_3$  radical [4] and is designated as  $s_1$ , also set equal to 0.25. The impinging  $\text{SiH}_3$  radicals may also land upon a physisorbed radical (Reaction C). The result is formation of  $\text{Si}_2\text{H}_6$  molecule that goes back in the gas phase making another hydride site available on the surface. We assign a probability of  $s_2 \sim 0.1$  ( $=0.25 \times 0.4$ ) to this reaction since the dangling bond on the incident radical has to point towards the physisorbed radical ( $\sim 0.25$ ) and can only attack the surface bond of the physisorbed radical from the sides, i.e. fractional area  $\sim 0.4$ . We assume that this reaction has no kinetic barrier. Because they are barrier free, the kinetic rates for reactions A-C are simply taken as the product of the silyl radical flux,  $f_{\text{Si}}$ , the surface site density, and the corresponding reaction probability ( $s_0$ ,  $s_1$ , or  $s_2$ ). Finally the silyl radical may directly abstract a surface H thus creating a dangling bond on the surface (Reaction D) through an Eley-Rideal mechanism. Molecular dynamics (MD) and ab-initio calculations have been used to determine the barrier for this reaction [18, 27-30]. Comparisons between MD of a silicon surface and density function theory (DFT) using a small cluster with the B3LYP functional and the 6-31G basis set showed close agreement between two methods [27]. However, a comparison between several ab-initio methods showed a spread in the

activation barrier from ~0.1 to 0.8eV using DFT and configurational interaction (CI) calculations respectively [18]. Each method has strengths and limitations, with the DFT calculations giving a lower bound and the CI calculations giving an upper bound for the actual barrier value [18]. The model calculation was performed with a H abstraction reaction probability,  $u_{a1}$ , of 0.25 for two values of H abstraction barrier:  $E_a(\text{abs})=0.4\text{eV}$ , which is an average of the DFT and CI ab-initio calculations [18], and  $E_a(\text{abs})=0.1\text{eV}$  commonly found from DFT. It is important to note that all Si-H bonds (present on either a mono-, di-, or tri-hydride site) are considered to have equivalent chemical reactivity towards hydrogen abstraction.

Once the silyl radical gets into a stable physisorbed state on the surface, there are several possible surface reactions. For example, it can simply desorb from the surface - Reaction E, or it can abstract a hydrogen atom from a neighboring hydride and leave the surface as  $\text{SiH}_4$  (Reaction F) thus creating a db on the surface. It could also hop onto another surface site, including hopping onto a dangling bond (Reaction G) or from one hydride to another (Reaction H).

When a physisorbed radical hops onto a nearby dangling bond and chemisorbs (Reaction G), two hydrides are produced on the surface (one where the silyl was physisorbed and the other replacing the db site where it chemisorbs). The radical hopping from one hydride onto another surface hydride (Reaction H) represents a critical step in the surface diffusion model since hopping on the surface is the primary pathway for redistributing deposited material on the surface. It has also been proposed that dangling bond diffusion to surface valleys is also an important step in obtaining smooth surface [26, 31-33]. Dangling bond diffusion has been invoked to account for non-

random surface growth because it has been presumed that dangling bond creation (and hence addition of silyl to a dangling bond site) is dominated by random H abstraction by H or SiH<sub>3</sub> through a direct Eley-Rideal process. Note that our model hypothesizes that the silyl diffusion is not completely random on the surface (it is favored on a monohydride surface). Therefore, dangling bond diffusion is not required to achieve non-random growth.

The activation barrier for silyl desorption has been estimated to be between 0.45eV and 0.9eV [4]. A value of 0.7eV was used here. The barrier for desorption is expected to be larger than the barrier for abstraction or hopping in order for the precursor to have a sufficient residence time on the surface to diffuse and find the optimal chemisorption site.

The apparent barrier for the hopping reaction has been measured using surface roughness evolution to be ~0.2eV [9] (note that similar values were also assumed in previous kinetic models by Perrin and Robertson [4, 17]). We believe that the hopping rate of the physisorbed radicals depends on the type of surface hydrides and hence will be different for diffusion on mono-, di- and tri-hydride sites. Different diffusion barriers are expected on different surfaces because of several factors, including: a) steric hindrance effects of extra H atoms present on the higher hydrides; and b) different binding energies for the physisorbed radicals on different hydrides, including for example, stronger dipole interactions for silyl on di- or tri-hydride surfaces. Also, the higher hydrides present a more corrugated surface at the atomic level and hence may hinder the diffusion of the physisorbed radical. This hypothesis is in agreement with the theoretical ab-initio and molecular dynamics calculations that show no Si-H-Si bound state for the silyl radical on

mono-hydride terminated surface [7, 18] suggesting a lower barrier for surface diffusion on these sites as compared with higher hydrides and with experimental measurements of the diffusion barrier which shows a decrease in the barrier under deposition conditions which promote monohydride surface coverage [34]. We assign a value of 0.2 and 0.3 eV to the hopping activation barriers on mono-hydrides, and di- or tri-hydrides respectively. For hopping onto a dangling bond, the barrier is chosen to be 0.3 eV (same as the barrier for hopping on higher hydrides). These values were assigned to be compatible the measured apparent barrier, and to be consistent with surface diffusion-dominated growth. The larger barrier on higher hydride surfaces is also consistent with recent calculations that suggest a “rolling” diffusion mechanism for physisorbed silyl [28]. The affect and importance of different transport barriers on different hydrogenated surfaces is discussed in detail in Section 6.4.1.3 below.

Two neighboring physisorbed radicals may recombine and desorb as  $\text{Si}_2\text{H}_6$  (Reaction I). The barrier for this reaction (0.7eV) is taken to be the same as that for desorption of an isolated radical on the surface. This mechanism is expected to contribute significantly only in the case of high physisorbed radical surface coverages on account of the 2<sup>nd</sup> order reaction rate and is not dominant in the temperature range (0 - 600 °C) considered in this study.

Recombination reactions between different surface hydrides provide an important pathway for removal of surface hydrogen and network formation through the creation of surface Si-Si bonds. Two adjacent hydrides can undergo dissociative recombination to release molecular  $\text{H}_2$ , (Reaction J) and result in the formation of surface Si-Si bonds that may or may not be strained depending on the particular configuration of the participating

hydrides. These thermally activated recombination reactions are primarily responsible for the changes in the distribution of surface hydrides under different deposition conditions. Higher hydrides are more likely to undergo the recombination reactions due to the presence of fewer number of Si-Si bonds. The presence of these rigid Si-Si bonds (as compared to the Si-H bonds) restricts the rearrangement of the surface atoms and therefore the higher hydrides have lower activation barriers towards the recombination reactions. Various recombination reactions (in order of increasing activation barriers) are tri-tri( $E_{33}$ ), tri-di( $E_{32}$ ), di-di( $E_{22}$ ), tri-mono( $E_{31}$ ), di-mono( $E_{21}$ ), and mono-mono( $E_{11}$ ). Although the exact barriers for these reactions are unknown, Guizot et al estimated values from 1.3 to 2.8eV based on  $H_2$  desorption measurements taken on crystal silicon [15]. Work by Kessels et al has fit the bulk hydrogen content to a model and extracted a barrier of  $\sim 0.15$ eV for  $H_2$  elimination [35]. Further calculations for the decomposition of  $SiH_3$  to  $SiH_2$  produced an activation barrier of  $\sim 0.21$ eV [26]. The large difference in these barrier values has been attributed to bond energy released through the formation of Si-Si bonds which is then available to lower the desorption energy [24]. This energy lowering by formation of Si-Si bonds is expected to proceed readily on the amorphous surface, but will occur to a lesser extent on the crystalline surface in the experiment of Guizot et al. We therefore choose the respective barriers as  $E_{33} \sim 0.20$ eV,  $E_{32} \sim 0.25$ eV,  $E_{22} \sim 0.3$ eV,  $E_{31} \sim 0.35$ eV,  $E_{21} \sim 0.45$ eV, and  $E_{11} \sim 0.6$ eV. The surface Si-Si bonds created as a result of these recombination reactions play a critical role in network formation and growth processes particularly under conditions where insertion reactions are significant. These surface Si-Si bonds may react directly with the impinging silyl radicals as well as the diffusing precursors on the surface as schematically shown in Reactions K-L. During a-

Si:H growth, there is a distribution of slightly different bond lengths and angles that result in a distribution of weak and strong Si-Si bonds. The radicals will likely be able to insert into only a fraction of the surface Si-Si bonds. Although the distribution of weak and strong bonds is expected to change with temperature, for simplicity we assume that only a small constant fraction ( $f = 0.1$ ) of the surface Si-Si bonds have strain energy above a threshold value that facilitates the insertion reactions. The choice of this value is somewhat arbitrary but the trends predicted by our model do not change significantly by the value chosen. This effectively renders ~90% of the surface Si-Si bonds to be stable to surface reaction, similar to “network” Si-Si bonds. This model therefore provides a means for silicon network formation not present in most other models. That is, Si-Si bond formation can proceed between two neighboring silicon hydrides, and ~90% of these bonds will not be affected by further surface reaction and will remain in the film. Finally, the surface hydrides may also recombine dissociatively at elevated temperatures resulting in two adjacent dangling bonds (for example, if the Si atoms are too far apart to form a Si-Si bond) as shown as Reaction M. The energetics of this reaction have been studied extensively at high temperatures and the barriers are reported to be between 1.8-2.5 eV [36] and therefore we assign a value of 1.9eV to the barrier for this reaction.

#### **6.2.4 Site Balance Equations for Various Surface Species**

Having identified the key surface reactions in a-Si:H deposition, four additional independent equations required to solve for the individual coverages of the different

surface species can be derived from the surface site balances for the dangling bonds ( $q_0$ ), physisorbed radicals ( $q_4$ ), mono-hydrides ( $q_1$ ) and the di-hydride species ( $q_2$ ). Note that the surface hydrogen concentration can be determined from the hydride distribution as  $q_h = 0.25 q_1 + 0.50 q_2 + 0.75 q_3$ . The surface coverage of the different species ( $q_0$ ,  $q_4$ ,  $q_1$  and  $q_2$ ) is expressed in terms of a set of coupled non-linear time-dependent differential equations ( $dq_i/dt$ ) that account for the generation and consumption of these different sites. If we assume a steady state growth, these differential equations reduce to a set of non-linear algebraic equations (since at steady state  $dq_i/dt = 0$ ). The individual steady state site balances for  $q_0$ ,  $q_4$ ,  $q_1$  and  $q_2$  are developed next.

#### 6.2.4.1 Dangling bond balance

Dangling bonds can be created by several distinct mechanisms: i) H abstraction reactions (from mono, di and tri-hydrides) by incident  $\text{SiH}_3$  radicals (Reaction D); ii) H abstraction by physisorbed radicals (Reaction F); iii) insertion of incident silyl radicals into strained Si-Si bonds (Reaction K); iv) insertion of physisorbed radicals (Reaction L); and v) desorptive recombination of hydrides (Reaction M). Dangling bonds are in turn consumed through addition (chemisorption) reactions A and G. Hence the steady state balance for the dangling bonds is given as:

$$\begin{aligned} n_{a1} f_{Si} q_{HT} + n_{a3} q_4 q_{HT} + (n_{i1} f_{Si} + n_{i3} q_4) f q_5 + 2n_{r1} q_{HT} q_{HT} \\ - s_0 f_{Si} q_0 - n_h q_0 q_4 = 0 \end{aligned} \quad (6)$$

where  $q_{HT}$  is the sum of all surface hydrides  $q_{HT} = q_1 + q_2 + q_3$ , and

$$n_h = \frac{(n_{h1} q_1 + n_{h2} q_2 + n_{h3} q_3)}{(q_1 + q_2 + q_3)}$$

is the effective hopping frequency of a physisorbed silyl on the surface hydrides.

#### 6.2.4.2 Physisorbed Radical Balance

The physisorbed radical site balance involves creation through physisorption of incident SiH<sub>3</sub> radicals on the surface (Reaction B), and removal through; i) abstraction by incident SiH<sub>3</sub> (Reaction C); ii) abstraction of surface H (Reaction F); iii) thermal desorption (Reaction E); iv) recombinative desorption of radicals (Reaction D); v) insertion into strained bonds (Reaction L); and vi) hopping onto a dangling bond (Reaction G):

$$s_1 \mathbf{f}_{Si} \mathbf{q}_{HT} - s_2 \mathbf{f}_{Si} \mathbf{q}_4 - s_4 \mathbf{f}_H \mathbf{q}_4 - \mathbf{n}_{a3} \mathbf{q}_4 \mathbf{q}_{HT} - \mathbf{n}_{d1} \mathbf{q}_4 - 2\mathbf{n}_{d2} \mathbf{q}_4 \mathbf{q}_4 - \mathbf{n}_{i3} \mathbf{q}_4 \mathbf{f} \mathbf{q}_5 - \mathbf{n}_h \mathbf{q}_0 \mathbf{q}_4 = 0 \quad (7)$$

#### 6.2.4.3 Surface Mono-hydride Balance

The mono-hydride sites are created through disproportionation reactions between higher hydrides, specifically two di-hydrides may recombine to form two mono-hydrides (plus a Si-Si bond and an H<sub>2</sub>) (Reaction J<sub>22</sub>), or di-hydride and tri-hydride may recombine to form a mono- and a di-hydride (Reaction J<sub>23</sub>). Some of the disproportionation reactions may also consume the mono-hydrides and produce Si-Si and H<sub>2</sub>, such as recombination of a mono- with a tri-hydride (Reaction J<sub>13</sub>) or recombination of two mono-hydrides (Reaction J<sub>11</sub>). Since physisorbed radicals are presumed to “mask” surface hydrides, further reactions between physisorbed radicals and the surface can lead to a net increase in available surface hydrides. For example, desorption of a physisorbed radical from a mono-hydride site (Reaction E) produces an mono-hydride available for further reaction. Likewise, whenever a radical physisorbed on a mono-hydride is

consumed through reaction with a neighbor, the monohydride under the physisorbed radical becomes available for further reaction. Examples include Eley-Rideal abstraction of another physisorbed radical (Reaction C), Langmuir-Hinshelwood abstraction of H from a neighboring hydride (Reaction F), and hopping of the physisorbed radicals (Reaction G). This results in the following site balance equations for the mono-hydrides:

$$\begin{aligned}
 & s_2 f_{Si} q_4 \frac{q_1}{q_{HT}} - s_1 f_{Si} q_1 - n_{a1} f_{Si} q_1 - n_{a3} q_4 q_1 + n_{d1} q_4 \frac{q_1}{q_{HT}} + n_{p23} q_2 q_3 \\
 & + 2n_{p22} q_2 q_2 - n_{p13} q_1 q_3 - 2n_{p11} q_1 q_1 - n_{r1} q_1 q_{HT} + n_{h1} q_4 q_4 \frac{q_1}{q_{HT}} = 0
 \end{aligned} \tag{8}$$

#### 6.2.4.4 Surface Di-hydride Balance

Di-hydrides are created through disproportionation of tri-hydrides and through removal of physisorbed radicals from di-hydride sites. Two di-hydrides are created upon disproportionation reactions between two tri-hydrides (Reaction J<sub>33</sub>). Likewise, one di-hydride is created when a tri- and a mono hydride react (Reaction J<sub>13</sub>). Several mechanisms can result in di-hydride consumption. Two di-hydrides are consumed during disproportionation of two di-hydrides (Reaction J<sub>22</sub>), and one di-hydride is consumed upon reaction between a di- and mono-hydride (Reaction J<sub>12</sub>). As discussed above for the mono-hydride case, abstraction, desorption or hopping of a physisorbed radical from a di-hydride site makes that site available for further reactions. This results in the following site balance equation for the di-hydrides:

$$\begin{aligned}
& s_2 \mathbf{f}_{Si} \mathbf{q}_4 \frac{\mathbf{q}_2}{\mathbf{q}_{HT}} - s_1 \mathbf{f}_{Si} \mathbf{q}_2 - n_{a1} \mathbf{f}_{Si} \mathbf{q}_2 - n_{a3} \mathbf{q}_4 \mathbf{q}_2 + n_{d1} \mathbf{q}_4 \frac{\mathbf{q}_2}{\mathbf{q}_{HT}} + 2n_{p33} \mathbf{q}_3 \mathbf{q}_3 \\
& - 2n_{p22} \mathbf{q}_2 \mathbf{q}_2 + n_{p13} \mathbf{q}_1 \mathbf{q}_3 - n_{p12} \mathbf{q}_1 \mathbf{q}_2 - n_{r1} \mathbf{q}_2 \mathbf{q}_{HT} + n_{h2} \mathbf{q}_o \mathbf{q}_4 \frac{\mathbf{q}_2}{\mathbf{q}_{HT}} = 0
\end{aligned} \tag{9}$$

Equations (3) through (9) form a complete set of 7 independent non-linear algebraic equations that may be solved simultaneously for the 7 independent variables ( $\mathbf{q}_0$ ,  $\mathbf{q}_1$ ,  $\mathbf{q}_2$ ,  $\mathbf{q}_3$ ,  $\mathbf{q}_h$ ,  $\mathbf{q}_4$ , and  $\mathbf{q}_5$ ) as a function of temperature and incoming radical flux. Note that we do not need to write the site balance for tri-hydride sites as it results in a dependent equation that may be deduced from a linear combination of the equations (6) through (9) presented above since  $d\mathbf{q}_3/dt = -d\mathbf{q}_0/dt - d\mathbf{q}_4/dt - d\mathbf{q}_1/dt - d\mathbf{q}_2/dt$  (as a consequence of the site balance equation (4)).

### 6.3 RESULTS

The steady state surface site coverages as well as the surface Si-Si and Si-H bond fractions were obtained through a numerical solution of the seven non-linear algebraic equations (equations 3-9) for deposition temperatures between 0 to 600°C and a barrier for H by silyl,  $E_a(\text{abs})=0.4$  eV, for several values of incident radical flux ( $\mathbf{f}_{Si} = 1, 10, 100$  and  $400 \text{ s}^{-1}$ ). A flux of  $1.0 \text{ s}^{-1}$  corresponds to approximately  $0.3 \text{ \AA/s}$ . The same calculation was carried out with  $E_a(\text{abs})=0.1$  eV for a flux of  $10 \text{ s}^{-1}$ . Results for the individual surface coverage fractions at steady state under different growth conditions are shown in Figures 6.1 through 6.5. We first present the effect of temperature on surface

composition under a typical growth rate condition ( $f_{\text{Si}} = 10 \text{ s}^{-1}$ , or  $\sim 3 \text{ \AA}/\text{sec}$ ) for  $E_a(\text{abs}) = 0.4 \text{ eV}$ , and then discuss the effect of flux and  $E_a(\text{abs})$  on determined parameters.

### 6.3.1 Effect of Temperature

Figure 6.1(b) shows the fractional coverage of surface mono- di- and tri- hydrides at deposition temperatures between 0-600°C for a radical flux of  $10 \text{ s}^{-1}$ . At low temperature ( $< 100^\circ\text{C}$ ), the model indicates that the surface remains almost entirely covered with tri-hydrides. As expected, as temperature increases, the coverage changes to di-hydride and then mono-hydride, until  $\sim 470^\circ\text{C}$  where the hydrogen begins to desorb rapidly. This is consistent with the in-situ infrared measurements of the surface hydride distribution reported by Marra et al [25] and Kessels et al [26].

The total surface hydrogen coverage vs. temperature is shown in Figure 6.2. For less than  $400^\circ\text{C}$ , the coverage decreases monotonically with increasing temperature, then a sharper decrease is observed, consistent with the well known decrease in bulk H content with increasing temperature [24]. The relationship between bulk and surface hydrogen is not expected to be simple because there are other processes in the near surface region and film bulk that result in H elimination. Various mechanisms have been proposed for surface hydrogen elimination during growth. Kessels et al. proposed that surface reactions are sufficient to control bulk hydrogen content [26] while Robertson proposed that lower thermodynamic solubility limit of H in the bulk results in a net out-diffusion of H from the bulk to the surface [23]. Bulk H content is expected to be lower than that

calculated from the steady-state surface hydride coverage. The model presented in this article does not explicitly present or explain a relationship between the surface and the bulk hydrogen content. It is expected, however, that under kinetically limited growth conditions, the bulk H content will follow a trend similar to the surface H content as a function of deposition temperature and film growth rate.

The steady state surface coverage of dangling bonds gives insight into the quality of the deposited film since the dangling bonds provide chemisorption sites that are essential for film growth. The effect of temperature on the surface db coverage with substrate temperature is shown in Figure 6.3(a). Curves a-d show the effect of flux with  $E_a(\text{abs})=0.4$ , and curve e corresponds to flux of  $10\text{s}^{-1}$  with  $E_a(\text{abs})=0.1\text{eV}$ . For  $E_a(\text{abs})=0.4\text{eV}$ , as temperature increases from  $0^\circ\text{C}$  to  $\sim 400^\circ\text{C}$ , the dangling bond coverage increases from  $\sim 0.1\%$  to  $\sim 1\text{-}2\%$ , reflecting an increase in hydrogen abstraction, then increases significantly at higher temperatures, due primarily to direct desorption. The transition occurs at a temperature that depends on the flux of incoming radicals, and will be discussed below. This trend in the surface dangling bond density with temperature is consistent with *in-situ* Electron Spin Resonance (ESR) measurements reported by Yamasaki et al. [20, 21]. Previous models [12] have suggested that the dangling bond density should first decrease then increase with increasing temperature. However, both the experimental data and the model presented here show only an increase in db density with increasing temperature. The smaller value of  $E_a(\text{abs})$  results in a significantly higher dangling bond surface coverage ( $\sim 50\%$ ), nearly independent of temperature.

The individual pathways for the creation and removal of dangling bonds have also been investigated. Figure 6.3(b) shows the contribution of each term in equation (6) towards dangling bond creation for  $E_a(\text{abs})=0.4$  and Figure 6.3(c) shows dangling bond removal mechanisms. As seen in Fig. 6.3(b), below  $400^\circ\text{C}$  the primary creation of dangling bonds comes through the indirect pathway of radical physisorption leading to hydrogen extraction. Above  $400^\circ\text{C}$ , hydrogen recombination dominates the process. As expected, for  $E_a(\text{abs})=0.1\text{eV}$  direct abstraction becomes more important, but physisorbed abstraction still dominates at flux of  $10\text{s}^{-1}$ . Figure 6.3(c) shows that at low temperatures, the dangling bonds removal proceeds through the chemisorption of diffusing physisorbed radicals, while at high temperature, direct chemisorption of the impinging radicals dominates. For  $E_a(\text{abs})=0.1\text{eV}$ , dangling bond removal by direct chemisorption dominates chemisorption by physisorbed radicals over all temperature ranges. Dangling bond removal is equivalent to film growth discussed in relation to Figure 6.7 below.

Figure 6.4 shows the physisorbed radical coverage calculated as a function of surface temperature. The radical coverage decreases monotonically with increasing growth temperatures, with a rapid decrease at higher temperatures. This indicates that physisorbed radical density decreases with increasing db density. However, for  $E_a(\text{abs})=0.4\text{eV}$  and a flux of  $10\text{s}^{-1}$  the physisorbed radical density decreased by a factor of  $10^5$  as temperature is raised from 0 to  $400^\circ\text{C}$ , whereas the db density increases by only a factor of 10. This difference is attributed to thermally activated processes involving physisorbed radicals that do not involve dangling bonds, including surface diffusion, desorption, and recombination.

The model also enables a prediction of the surface Si-Si bond fraction, and model results are shown in Figure 6.5. The Si-Si bond density will be important, for example, to understand the amorphous to polycrystalline silicon transition in growth, since conditions that favor Si-Si surface bond formation will likely promote crystallite formation. For  $E_a(\text{abs})=0.4\text{eV}$  and flux =  $10\text{s}^{-1}$  the model predicts that the Si-Si bond fraction reaches a maximum value of  $\sim 20\%$  at  $\sim 450^\circ\text{C}$ . The maximum is attributed to a change in the dominant film growth process from a surface diffusion limited at low deposition temperatures, to flux limited (i.e. direct chemisorption dominated) at higher temperatures. This observed trend in Si-Si bond density with temperature correlates well with the well-known experimental trend of crystallization fraction with increasing deposition temperature, where crystalline fraction increases with temperature, then drops to zero above  $400^\circ\text{C}$  [37]. When the smaller value of  $E_a(\text{abs})=0.1\text{eV}$  is used, a smaller density of surface Si-Si bonds is observed.

### **6.3.2 Effect of Incident Precursor Flux on Surface Composition**

The growth rate of the films is determined by the flux of incident silyl radicals and has a strong impact on the surface composition. The predicted effect of flux on surface hydride composition is shown in Figure 6.1(a-d) for  $E_a(\text{ads})=0.4\text{eV}$ . Decreasing flux from  $10\text{s}^{-1}$  to  $1.0\text{s}^{-1}$  results in an increase in the monohydride fraction at moderate temperatures ( $150^\circ\text{-}350^\circ\text{C}$ ). At higher flux, the di- and tri-hydrides dominate the surface hydrogen coverage. Figure 6.2 shows the related increase in surface hydrogen coverage

with increasing flux at all temperatures analyzed. This increase in surface hydrogen with increasing flux is primarily due to increased flux of H in the  $\text{SiH}_3$  radical, and a shorter time between adsorption events, leading effectively to a shorter reaction time available for hydrogen elimination reactions, such as recombination. At high temperatures, H removal is due primarily to  $\text{H}_2$  desorption, and in Figure 6.2 a sudden decrease in H coverage is observed as temperature increases. Figure 6.2 also shows that this “transition temperature” increases with increasing silyl flux. The increase in the transition temperature reflects a decrease in the net radical desorption rate as flux increases.

Figure 6.3(a) shows the effect of silyl flux on dangling bond density for  $E_a(\text{abs})=0.4\text{eV}$ . For low to moderate temperatures ( $<350^\circ\text{C}$ ) the dangling bond density is independent of silyl flux. This indicates that in this temperature range, the creation of dangling bonds is dominated by L-H type reactions that involve only surface species and do not involve incident radicals. A significant effect of flux is predicted for temperatures above  $\sim 400^\circ\text{C}$ . The reduction in db density with increasing radical flux at temperatures between  $400^\circ$  and  $550^\circ\text{C}$  is attributed to H desorption dominating silyl chemisorption at low flux (leading to increase in db density), whereas silyl flux dominates H desorption at high silyl flux (helping to maintain a smaller db density). As will be discussed below, this result is consistent with measurements of growth rate vs temperature during high-rate silicon deposition [24], where the deposition rate is found to be independent of temperature even to temperatures as high as  $500^\circ\text{C}$ .

The effect of flux on physisorbed radical density is shown in Figure 6.4 for  $E_a(\text{abs})=0.4\text{eV}$ . Increasing flux leads to a larger physisorbed radical density over the

entire temperature range. As will be shown in the following section, an increase in surface radical density results in an increased growth rate. The effect of flux on physisorbed radical density, therefore, is consistent with the observed increase in film growth rate with increasing radical flux, independent of temperature. This is also consistent with chemisorption being the dominant contributor to film growth.

The effect of increasing precursor flux on calculated fractional concentration of Si-Si bonds is shown in Figure 6.5. At temperatures less than  $\sim 400^\circ\text{C}$ , a larger radical flux leads to a decrease in the Si-Si bond fraction. This is also consistent with well known experimental results that show that lower growth rates help achieve a larger crystallite size and fraction in deposited micro- and poly-silicon.

## 6.4 MACROSCOPIC PARAMETERS

### 6.4.1 Determining the Macroscopic Parameters Characterizing Film Growth

Once the steady state surface coverage of various individual species (i.e., dangling bonds, surface hydrides, physisorbed radicals and strained bonds) is determined for a particular set of process parameters, such as the substrate temperature and silyl flux, various macroscopic measurable parameters can be estimated. Macroscopic parameters of interest include: 1) the steady state film growth rate ( $R_G$ ); 2) the overall surface reaction probability for incident radicals ( $b$ ); and 3) the incorporation probability for incident radicals ( $s$ ). Values for  $b$  and  $s$  have been measured experimentally [13, 38] and are useful to check the validity of the model. The effect of process conditions on growth

rate is also well known and can be determined by this model. The apparent characteristic diffusion length ( $L_d$ ) of the physisorbed radicals, and the apparent thermal activation barrier for surface diffusion ( $E_a$ ) are also important parameters that can be extracted from the model. Values for both parameters have recently been obtained using silicon surface topology evolution during film growth [9].

#### 6.4.1.1 Growth Rate

The net growth rate,  $R_G$  (in Å/sec), is calculated from the rates of all the reactions that result in the formation of a Si-Si bond between a precursor and the surface Si atoms, where the addition of a Si-Si bonds extends the surface by  $\sim 1$  Si-Si bond length ( $a$  2.4Å):

$$R_G = a \cdot (s_0 f_{Si} q_0 + n_{i1} f_{Si} f q_5 + n_h q_0 q_4 + n_{i3} q_4 f q_5) \quad (11)$$

The first two terms result from direct chemisorption (on a surface dangling bond) and direct insertion (into strained Si-Si bonds) of impinging SiH<sub>3</sub> radicals. The third and fourth terms describe Si-Si bonds formed by chemisorption or insertion of a physisorbed SiH<sub>3</sub> precursor. The etching of the surface by incident radicals can also occur, but etching is only significant in the case of high hydrogen dilution, and/or when the surface coverage of the tri-hydrides is significant (i.e., at very low temperatures), and is therefore negligible for the conditions described in this study.

#### 6.4.1.2 Overall Reaction Probability ( $\mathbf{b}$ ) and Incorporation Probability ( $s$ )

The overall reaction probabilities for incident silyl radicals are shown schematically in Figure 6.6. Pathway ‘a’ represents the incident silyl flux and all other

reaction probabilities are normalized with respect to this flux ( $a=1= b + d + e + f$ ). The other pathways are defined as follows: 'b' is made up of 'b<sub>1</sub>', reflection of SiH<sub>3</sub>, and 'b<sub>2</sub>', direct H abstraction by SiH<sub>3</sub>; 'c' is physisorption of silyl radicals; 'd' is direct incorporation of silyl radicals through chemisorption or insertion (with probability  $s_a$ ); and 'e' is made up of 'e<sub>1</sub>', recombination of two physisorbed silyl radicals as Si<sub>2</sub>H<sub>6</sub>, 'e<sub>2</sub>', desorption of physisorbed silyl radical as SiH<sub>3</sub>, and 'e<sub>3</sub>', H abstraction by physisorbed silyl radicals. The parameter 'f' is incorporation of physisorbed radical through chemisorption or insertion (probability  $s_b$ ). Then  $b= b_1 + b_2$ ;  $e= e_1 + e_2 + e_3$ ;  $\gamma= b_2 + e_1 + e_3$ ;  $s = (s_a + s_b) = d + f$ ; and  $\beta = s + \gamma$ . The probability that the radical returns back into the gas phase, either by direct reflection or physisorption then desorption, is  $1-\mathbf{b} = (b_1 + e_2)$ . If the radical does not reflect from the surface (pathway 'b<sub>1</sub>') or physisorb then desorb (pathway 'e<sub>2</sub>'), it must react with the surface with probability  $\mathbf{b}$ , either through either direct reactions (pathways 'b<sub>2</sub>' or 'd') or by physisorbing, diffusing and reacting (pathways 'e<sub>1</sub>', 'e<sub>3</sub>', or 'f'). Reaction pathways 'd' and 'f' lead to incorporation of radicals into the film, and pathways 'b<sub>2</sub>', 'e<sub>1</sub>', and 'e<sub>3</sub>' result in the radical being released from the surface after reacting. The probability of direct incorporation of the silyl radical through pathway 'd' is  $s_a$ , and the probability of indirect incorporation through pathway 'f' is  $s_b$ . The radical could also return to the gas phase after reacting on the surface with probability  $\mathbf{g}$ . The term  $\mathbf{g}$  includes direct abstraction of H from the surface (pathway 'b<sub>2</sub>'), abstraction of H by a physisorbed radical (pathway 'e<sub>3</sub>') and the recombination of two physisorbed radicals to form Si<sub>2</sub>H<sub>6</sub> (pathway 'e<sub>1</sub>'). The overall incorporation (or

“sticking”) probability,  $s$ , is the fraction of impinging atoms that end up in the film (either through pathway ‘d’ or ‘f’ and is therefore given as a sum of  $s_a$  and  $s_b$ .

The incorporation probability,  $s$ , of the radicals includes reactions that lead to a net incorporation of the impinging radical, as shown in equation (12). Reactions leading to incorporation include direct chemisorption (Reaction A) and direct insertion (Reaction K), as well as chemisorption (Reaction G) and insertion (Reaction L) of the physisorbed radicals. The first two terms in equation (12) correspond to direct incorporation pathways (and the sticking probability  $s_a$ ), while the 3<sup>rd</sup> term corresponds to the product of physisorption probability of an incident silyl radical and the probability that the physisorbed radical will get incorporated in the film.

$$s = s_0 \mathbf{q}_0 + \mathbf{u}_{i1} f \mathbf{q}_5 + s_1 \mathbf{q}_{HT} \frac{\mathbf{u}_h \mathbf{q}_0 + \mathbf{u}_{i3} f \mathbf{q}_5}{\mathbf{u}_{a3} \mathbf{q}_{HT} + \mathbf{u}_{d1} + \mathbf{u}_h \mathbf{q}_0 + \mathbf{u}_{d2} \mathbf{q}_4 + \mathbf{u}_{i3} f \mathbf{q}_5 + s_2 \mathbf{f}_{Si}} \quad (12)$$

The overall reaction probability,  $\mathbf{b}$ , includes all the reaction pathways through which the SiH<sub>3</sub> precursor may react with the surface. This includes direct reactions between the surface and the impinging SiH<sub>3</sub> radicals, as well as reactions between the surface and physisorbed SiH<sub>3</sub>:

$$\mathbf{b} = s_0 \mathbf{q}_0 + \mathbf{u}_{i1} f \mathbf{q}_5 + \mathbf{u}_{a1} \mathbf{q}_{HT} + s_1 \mathbf{q}_{HT} \frac{\mathbf{u}_{a3} \mathbf{q}_{HT} + \mathbf{u}_h \mathbf{q}_0 + \mathbf{u}_{d2} \mathbf{q}_4 + \mathbf{u}_{i3} f \mathbf{q}_5 + s_2 \mathbf{f}_{Si}}{\mathbf{u}_{a3} \mathbf{q}_{HT} + \mathbf{u}_{d1} + \mathbf{u}_h \mathbf{q}_0 + \mathbf{u}_{d2} \mathbf{q}_4 + \mathbf{u}_{i3} f \mathbf{q}_5 + s_2 \mathbf{f}_{Si}} \quad (13)$$

Here the reaction probability of the physisorbed radicals (4<sup>th</sup> term in equation (13)) is derived from the fraction of physisorbed radicals ( $s_1 \cdot q_{HT}$ ) that react with the surface. Pertinent surface reactions involving physisorbed radicals include chemisorption (Reaction G), abstraction (Reaction F), insertion (Reaction L), recombination with another physisorbed radical (Reaction I), and direct abstraction through incident radicals (Reaction C).

#### 6.4.1.3 Characteristic Diffusion Length, and Apparent Activation Energy

The characteristic diffusion length of the physisorbed precursors is estimated from the RMS displacement of the physisorbed radicals on the mono-hydride sites. This diffusion length is related to the average number of hops,  $N$ , that a physisorbed radical makes on the surface before undergoing any reaction that may remove it from the physisorbed state, and the distance covered in each hop,  $d$ .  $N$  is simply calculated as the ratio of the hopping rate of the physisorbed radical from one surface site to another to the sum total of all other reactions it may participate in.

Using the “random-walk” model [39] for surface diffusion of this physisorbed radical, and assuming the average distance per hop,  $d$ , remains constant, the diffusion length may be estimated as  $L_D = d \cdot \sqrt{N}$ . The distance per hop is estimated to be  $\sim 3.7 \text{ \AA}$ . This is determined from the average distance between Si atoms on the surface,  $d = \sqrt{1/N_{Si}}$ , where  $N_{Si}$  is the surface density of Si atoms, taken to be between  $6.9 \times 10^{14}$  atoms/cm<sup>2</sup> for the Si(100) surface and  $7.8 \times 10^{14}$  atoms/cm<sup>2</sup> for the Si(111) surface.  $L_d$  is then written as:

$$L_d = d \cdot \sqrt{\frac{\mathbf{u}_h \mathbf{q}_1}{\mathbf{u}_{a3} \mathbf{q}_{HT} + \mathbf{u}_d + \mathbf{u}_h \mathbf{q}_0 + \mathbf{u}_{d2} \mathbf{q}_4 + \mathbf{u}_{i3} f \mathbf{q}_5 + s_2 \mathbf{f}_{Si}}} \quad (14)$$

The behavior of diffusion length with temperature is governed by the ratio of effective hopping rate on hydrides to the sum of abstraction, desorption and chemisorption of the physisorbed radicals. To model surface diffusion, and achieve the experimentally observed trends in step coverage, the barrier for hopping on hydrides is typically taken to be smaller than the barriers for abstraction and desorption. This means that as temperature increases, the rate of radical removal (by abstraction and desorption) increases more rapidly than the diffusion rate, leading to a decrease in the average diffusion distance and an apparent physisorbed radical diffusion barrier (related to the difference,  $E_{h,eff} - E_a - E_d - E_h$ ) that is negative. Since experimental data indicates that  $L_d$  increases with temperature [9], and the barrier for hopping must remain smaller than for precursor removal, a different model for surface diffusion is needed. One possible modification to previous models that is reasonable and is consistent with the observed experiments, involves assuming that the surface diffusion proceeds more easily on some parts of the surface than on others. Specifically, if the barrier for surface diffusion is smaller on mono-hydride terminated surface regions than it is on di- or tri-hydrides, then diffusion rate is expected to increase as the surface coverage changes from tri- and di-hydrides at low temperature to predominantly mono-hydride at higher temperatures. This still enables surface diffusion to dominate over desorption and abstraction under typical growth temperatures.

In the model presented here, it is hypothesized that the rate of surface hopping will depend on the nature of the hydrides covering the growth surface. We believe that it is possible that the barrier to surface diffusion will be smaller for surface diffusion of a physisorbed radical onto a mono-hydride site as compared to a di-hydride or tri-hydride site. This assumption is reflected in our choice of diffusion barriers of 0.3eV for the radical diffusion onto tri-or di-hydrides and 0.2eV onto mono- hydride terminated silicon atoms. This difference in diffusion barrier energies is possible, for example, if the physisorbed radical binds strongly to di- and tri-hydrides inhibiting further diffusion. It could also result from the nature and structure of the physisorbed state itself. Recent theoretical results[7, 18] suggest that silyl does not physisorb with a bond-centered hydrogen atom as is often assumed. Therefore, other configurations for the physisorbed radical that strongly favor adsorption onto the mono-hydride surface could be envisioned. An example of such a state has recently been proposed [28], where adsorption involves movement of the surface-bound hydrogen atom into a neighboring Si-Si bond. This movement would be significantly inhibited on a di- or tri-hydride site, effectively creating a large kinetic barrier to physisorption on those surface sites.

As described below, the assumption of different diffusion barriers on different surfaces leads to a hopping distance that can increase or decrease with increasing surface temperature, depending on process conditions. Using the diffusion length data, the apparent activation energy for diffusion can be determined from a plot of  $\ln(L_d^2)$  vs.  $1/T$ , where the data is fit to a straight line over a finite temperature range.

## 6.4.2 Comparison with Experiments

In this section, values for macroscopic parameters described above are obtained from the kinetic model and are compared with experiments. The film growth rate,  $R_G$ , determined from equation 11 is plotted under different incident radical flux and substrate temperature conditions in Figure 6.7(a) for  $E_a(\text{ads})=0.4\text{eV}$ . The deposition rate remains constant at lower to intermediate temperatures (below 350-450°C and then rapidly increases to a higher saturation value at high temperatures (>400-450°C). The temperature associated with the rise in growth increases with increasing incident flux,  $f_{Si}$ . This is consistent with Matsuda et al's [13] observation of an increase in the growth rate above 400°C for films deposited at low deposition rate in a low radical flux regime,  $f_{Si} \sim 10\text{s}^{-1}$ . Under higher flux conditions, van de Sanden et al. [24] showed that the growth rate was constant with substrate temperature for temperatures as high as 500°C. Both of these observations are consistent with the model results shown in Figure 6.7(a). A plot is also shown for  $E_a(\text{ads})=0.1\text{eV}$  for a flux of  $10\text{s}^{-1}$ , indicating that the growth rate is not strongly affected by this change in abstraction barrier parameter, however, the primary mechanism for growth is strongly dependent on this parameter as shown next.

The growth rate results also enable us to suggest which growth processes contribute most significantly as a function of temperature and radical flux. Equation 11 is the sum of four distinct mechanisms for silyl incorporation into the growing film: 1) direct chemisorption into dangling bonds; 2) direct insertion into strained Si-Si bonds; 3) radical physisorption, diffusion, and chemisorption onto dangling bonds; and 4) radical

physisorption, diffusion, and insertion into strained Si-Si bonds. The contribution of each of these individual terms is plotted vs. substrate temperature for a flux of  $10\text{s}^{-1}$  in Figure 6.7(b) for  $E_a(\text{abs})=0.4\text{eV}$  and in Figure 6.7(c) for  $E_a(\text{abs})=0.1\text{eV}$ . Figure 6.7(b) shows that in the model presented here with  $E_a(\text{abs})=0.4\text{eV}$ , silyl physisorption, diffusion, and subsequent chemisorption onto a dangling bond site dominates over other growth mechanisms for temperatures up to  $500^\circ\text{C}$ . The physisorbed radical chemisorption flux is determined from the product of temperature dependent dangling bond surface density,  $q_0$ , the rate of hopping onto dangling bonds,  $v_h$ , and the physisorbed radical surface density,  $q_4$ . The temperature independent deposition rate is observed primarily because as temperature increases, the physisorbed radical density decreases, but the rate of physisorbed radical hopping and chemisorption increases to maintain the radical incorporation rate. The importance of surface diffusion in low temperature silicon growth is consistent with studies of topology evolution in these materials [9].

As shown in Figure 6.7(c), when  $E_a(\text{abs})=0.1\text{eV}$  is used, direct chemisorption of precursors contributes much more to growth than chemisorption of physisorbed precursors. Chemisorbed species typically do not diffuse easily at low temperature, so if the abstraction barrier is this small, then some mechanism must be included to account for significant surface transport of physisorbed species to achieve the widely observed smooth surface coverage.

Closely related to the growth rate of the films are the macroscopic reaction probabilities  $b$  and  $s$  (shown in Figure 6.8). The model results indicate that the overall reaction probability  $b$  remains constant  $\sim 0.25$  in the entire range of substrate temperatures

considered (-100 to 600°C) and does not vary with the changes in the surface coverages of the various surface species considered. The sticking probability  $s$ , on the other hand is observed to depend on the deposition conditions and follows the same general trends as the growth rate. The sticking probability increases from a constant value of  $\sim 0.12$  (temperature between 0 to  $\sim$ transition temperature) to  $\sim 0.24$  (above the transition temperature) when  $E_a(\text{abs})=0.4\text{eV}$ . Similar trends are found (curve e) for  $E_a(\text{abs})=0.1\text{eV}$ . Typically, amorphous silicon films show smooth surface texture and conformal coverage of steps and trenches, and measurement of profile shapes can be used to determine the overall reaction probability,  $\beta$ , as well as the sticking probability,  $s$ , and hence the ratio  $s/\beta$  [13]. Under low to moderate growth rates, the value of the ratio  $s/\beta$  is measured to be  $\sim 0.4$  at  $T < 350^\circ\text{C}$ , and increases to  $\sim 1$  above  $450^\circ\text{C}$  [13]. The change is generally ascribed to the substantial increase in the dangling bond density created through increased recombination reactions at higher temperatures. Under these low to moderate growth rate conditions, the values of  $b \sim 0.26$  and  $s \sim 0.11$  are observed experimentally to be independent of temperature between 25 and  $\sim 400^\circ\text{C}$ , and above  $400^\circ\text{C}$   $b$  continues to be constant and  $s$  increases, following the same trend with temperature in Figure 6.8.

Another important parameter is the diffusion length of the physisorbed radical on the growth surface. Figure 6.9(a) shows the model output for the effect of deposition conditions (temperature and incident radical flux) on the surface diffusion length of the physisorbed precursors for  $E_a(\text{abs})=0.4\text{eV}$ . For a flux of  $10 \text{ sec}^{-1}$ , the diffusion length is observed to increase with temperature up to  $\sim 200^\circ\text{C}$ , then decrease. The hypothesis of a surface-dependent diffusion barrier is included in the model, and results in the trends

observed in Figure 6.9(a). It also results in reasonable values for the apparent diffusion activation barrier as discussed below.

The trends in diffusion length with temperature are described as follows. The initial increase in the diffusion length at low temperatures results from an increase in the mono-hydride sites on the surface that have a lower barrier for surface diffusion. At moderate temperatures ( $200^{\circ}\text{C} < T < 400^{\circ}\text{C}$  for flux  $\sim 1\text{s}^{-1}$ ) where there are more mono-hydrides on the surface, there is a gradual decline in  $L_d$  due to increased abstraction and desorption reaction rates, similar to previous models. As temperature continues to increase, a rapid decline in  $L_d$  results from an increase in the dangling bond density on the surface, which shortens the residence time and diffusion length of the radicals on the surface.

Increasing the radical flux at temperatures below  $400^{\circ}\text{C}$  results in a decrease in the precursor surface diffusion length. This results primarily from an increase in abstraction of physisorbed precursors by the larger flux of incident radicals. It is well documented that low deposition rates (i.e. low incident radical flux) promotes network formation and, under sufficient hydrogen radical flux, formation of crystallites. The transition from amorphous to micro- or poly-crystalline growth can then be attributed to a larger diffusion length for the physisorbed radicals (and a smaller apparent diffusion barrier), consistent with many previous models of microcrystalline growth.

The apparent barrier to physisorbed radical surface diffusion is determined from the plot shown in Figure 6.9(b) for several values of incident radical flux with  $E_a(\text{abs})=0.4\text{eV}$ . The apparent barrier increases from  $\sim 0.15\text{eV}$  under very low deposition rate ( $\sim 0.3\text{\AA}/\text{s}$ ) to  $\sim 0.35\text{eV}$  at high deposition rate ( $\sim 100\text{\AA}/\text{s}$ ). This change in the apparent

barrier is a direct result of the changes in the surface hydride distribution under different deposition conditions. Under very low radical fluxes, the surface is predominantly covered by mono-hydride sites on which the radicals can diffuse rapidly (hence the large diffusion length and the lower apparent barrier) while under high flux conditions the higher hydrides are present in a significant fraction that results in a smaller diffusion length and a higher barrier.

The calculated diffusion length and apparent diffusion activation energy for  $E_a(\text{abs})=0.1\text{eV}$  are shown in Figure 6.9(c) and (d). Using the diffusion mechanisms and parameters given in Table 6.1, we find that the average diffusion length at typical growth temperatures is reduced by a factor of 10 compared to calculations done with  $E_a(\text{abs})=0.4\text{eV}$ . The apparent diffusion barrier is also much larger ( $>0.6\text{eV}$ ), consistent with transport limited by the large density of dangling bonds. We conclude that if the value for  $E_a(\text{abs})$  is close to  $0.1\text{eV}$  as is concluded by several calculations, then other mechanisms for fast diffusion of chemisorbed species must be developed to understand the smooth surface morphology widely observed in low temperature amorphous silicon growth.

It is important to note that the agreement between experimental values of diffusion activation barrier and the apparent activation energy found from the model plot in Figure 6.9(b) for  $E_a(\text{abs})=0.4\text{eV}$  is not conclusive evidence for the proposed surface diffusion mechanisms and parameters. However, the model demonstrates physical self-consistency, which is required for any viable set of parameters and physical mechanisms.

## 6.5 CONCLUSIONS

A newly developed valence balance approach in combination with the site balance is used in a kinetic model for low temperature silicon film deposition. The valence balance accounts for surface Si-Si bonds, which enables a quantitative analysis of radical precursor insertion into Si-Si bonds, and the rate of Si-Si bond formation. The model enables the number density of surface silicon atoms bound to one, two, or three hydrogen atoms, as well as the surface density of dangling bonds and physisorbed radicals to be calculated as a function of temperature and precursor flux under steady state growth conditions. We find that experimental data is consistent with our hypothesis that precursor diffusion on the surface is thermally activated, where the precursor surface diffusion rate depends on the nature of the surface physisorption site. If the diffusion rate for precursors physisorbed on di- and tri-hydride sites is impeded relative to those on mono-hydride sites, then at low temperatures, the diffusion length increases with increasing temperature due to an increase in the fractional surface coverage of silicon mono-hydride sites. The calculated trends in growth rate, surface reaction probability, overall sticking probability, and precursor diffusion length vs. deposition temperature and precursor flux are all consistent with available experimental results, when the kinetic barrier for H abstraction by silyl,  $E_a(\text{abs}) = 0.4\text{eV}$  is used. A smaller kinetic barrier of  $E_a(\text{abs}) = 0.1\text{eV}$  determined from several calculations leads to non-physical kinetic barriers for surface diffusion.

## **6.6 ACKNOWLEDGEMENTS**

Funding from the NSF through grant numbers 9624612 and 0072784 is acknowledged.

## 6.7 REFERENCES

- [1] R. Crandall and W. Luft, *Progress in Photovoltaics*, **3**, 315 (1995).
- [2] J.R. Abelson, *Applied Physics a-Materials Science & Processing*, **56**, 493 (1993).
- [3] J. Perrin, *Journal of Non-Crystalline Solids*, **137**, 639 (1991).
- [4] J. Perrin, M. Shiratani, P. Kae-Nune, H. Videlot, J. Jolly, and J. Guillon, *Journal of Vacuum Science & Technology A*, **16**, 278 (1998).
- [5] O. Leroy, G. Gousset, L.L. Alves, J. Perrin, and J. Jolly, *Plasma Sources Science & Technology*, **7**, 348 (1998).
- [6] E.A.G. Hamers, A.F.I. Morral, C. Niikura, R. Brenot, and P.R.I. Cabarrocas, *Journal of Applied Physics*, **88**, 3674 (2000).
- [7] S. Ramalingam, D. Maroudas, and E.S. Aydil, *Journal of Applied Physics*, **86**, 2872 (1999).
- [8] J.E. Gerbi and J.R. Abelson, *Journal of Applied Physics*, **89**, 1463 (2001).
- [9] K.R. Bray and G.N. Parsons, *Physical Review B*, **65**, 035311 (2002).
- [10] A. Gallagher, *Journal of Applied Physics*, **60**, 1369 (1986).
- [11] G. Ganguly and A. Matsuda, *Physical Review B-Condensed Matter*, **47**, 3661 (1993).
- [12] G. Ganguly and A. Matsuda, *Journal of Non-Crystalline Solids*, **166**, 31 (1993).
- [13] A. Matsuda and T. Goto, in *Materials Research Society Symposium Proceedings*, 1990), Vol. 164, p. 3.
- [14] A. Matsuda, *Thin Solid Films*, **337**, 1 (1999).

- [15] J.L. Guizot, K. Nomoto, and A. Matsuda, *Surface Science*, **244**, 22 (1991).
- [16] K. Maeda, A. Kuroe, and I. Umezu, *Physical Review B*, **51**, 10635 (1995).
- [17] J. Robertson and M.J. Powell, *Thin Solid Films*, **337**, 32 (1999).
- [18] A. Gupta, H. Yang, and G.N. Parsons, *Surface Science*, **496**, 307 (2002).
- [19] A. von Keudell and J.R. Abelson, *Physical Review B-Condensed Matter*, **59**, 5791 (1999).
- [20] S. Yamasaki, U.K. Das, T. Umeda, J. Isoya, and K. Tanaka, *Journal of Non-Crystalline Solids*, **266**, 529 (2000).
- [21] S. Yamasaki, T. Umeda, J. Isoya, and K. Tanaka, *Applied Physics Letters*, **70**, 1137 (1997).
- [22] S. Yamasaki, T. Umeda, J. Isoya, and K. Tanaka, *Journal of Non-Crystalline Solids*, **230**, 83 (1998).
- [23] J. Robertson, *Journal of Applied Physics*, **87**, 2608 (2000).
- [24] M.C.M. van de Sanden, W.M.M. Kessels, R.J. Severens, and D.C. Schram, *Plasma Physics and Controlled Fusion*, **41**, A365 (1999).
- [25] D.C. Marra, E.A. Edelberg, R.L. Naone, and E.S. Aydil, *Journal of Vacuum Science & Technology a-Vacuum Surfaces and Films*, **16**, 3199 (1998).
- [26] W.M.M. Kessels, A.H.M. Smets, D.C. Marra, E.S. Aydil, D.C. Schram, and M.C.M. van de Sanden, *Thin Solid Films*, **383**, 154 (2001).
- [27] S. Ramalingam, D. Maroudas, E.S. Aydil, and S.P. Walch, *Surface Science*, **418**, L8 (1998).
- [28] R. Dewarrat and J. Robertson, *Journal of Non-Crystalline Solids*, **299-302**, 48 (2002).

- [29] R. Dewarrat and J. Robertson, *Materials Research Society Symposium Proceedings*, **715**, A15.3 (2002).
- [30] K. Nakajima, K. Miyazaki, H. Koinuma, and K. Sato, *Journal of Applied Physics*, **84**, 606 (1998).
- [31] D.M. Tanenbaum, A.L. Laracuente, and A. Gallagher, *Physical Review B-Condensed Matter*, **56**, 4243 (1997).
- [32] A.H.M. Smets, D.C. Schram, and M.C.M. van de Sanden, *Materials Research Society Symposium Proceedings*, **609**, A7.6.1 (2000).
- [33] D.A. Doughty, J.R. Doyle, G.H. Lin, and A. Gallagher, *Journal of Applied Physics*, **67**, 6220 (1990).
- [34] K.R. Bray, A. Gupta, and G.N. Parsons, *Applied Physics Letters*, **80**, 2356 (2002).
- [35] W.M.M. Kessels, R.J. Severens, M.C.V. van de Sanden, and D.C. Schram, *Journal of Non-Crystalline Solids*, **230**, 133 (1998).
- [36] D.J. Doren, in *Advances in Chemical Physics, Vol 95 - Surface Properties* (John Wiley & Sons Inc, New York, 1996), Vol. 95, p. 1.
- [37] A. Matsuda, *Journal of Non-Crystalline Solids*, **59-6**, 767 (1983).
- [38] A. Matsuda, K. Nomoto, Y. Takeuchi, A. Suzuki, A. Yuuki, and J. Perrin, *Surface Science*, **210**, 114 (1990).
- [39] G.A. Somorjai, *Introduction to surface chemistry and catalysis* (Wiley, New York, 1994).

No.	Reaction	Description	Parameter		Rate
A	$\text{Si}^- + \text{SiH}_3(\text{g}) \rightarrow \text{Si}^-\text{SiH}_3$	Addition of $\text{SiH}_3$ to db	$s_0$		$s_0 \cdot \phi_{\text{Si}} \cdot \theta_0$
B	$(\text{SiH}_x) + \text{SiH}_3(\text{g}) \rightarrow (\text{SiH}_x)(\text{SiH}_3)_p$	Physisorption of $\text{SiH}_3$ on Hyd	$s_1$		$s_1 \cdot \phi_{\text{Si}} \cdot \theta_x$
C	$(\text{SiH}_x)\text{SiH}_3 + \text{SiH}_3(\text{g}) \rightarrow (\text{SiH}_x) + \text{Si}_2\text{H}_6(\text{g})$	Abstraction of Phys by $\text{SiH}_3$	$s_2$		$s_2 \cdot \phi_{\text{Si}} \cdot \theta_4$
D	$(\text{SiH}_x) + \text{SiH}_3 \rightarrow (\text{SiH}_{x-1})^- + \text{SiH}_4(\text{g})$	Abstraction of H by $\text{SiH}_3$	$\nu_{a1}$	$E_{a1}$	$\nu_{a1} \cdot \phi_{\text{Si}} \cdot \theta_x$
E	$(\text{SiH}_x)\text{SiH}_3 \rightarrow (\text{SiH}_x) + \text{SiH}_3(\text{g})$	Desorption of Phys $\text{SiH}_3$	$\nu_{d1}$	$E_{d1}$	$\nu_{d1} \cdot \theta_4$
F	$(\text{SiH}_x)\text{SiH}_3 \rightarrow (\text{SiH}_{x-1})^- + \text{SiH}_4(\text{g})$	Abstractn. of H by Phys $\text{SiH}_3$	$\nu_{a3}$	$E_{a3}$	$\nu_{a3} \cdot \theta_4 \cdot \theta_x$
G	$(\text{SiH}_x)\text{SiH}_3 + \text{Si}^- \rightarrow \text{SiH}_x + \text{SiSiH}_3$	Chemisorption of Phys $\text{SiH}_3$	$\nu_{hx}$	$E_{hx}$	$\nu_{hx} \cdot \theta_4 \cdot \theta_0$
H	$(\text{SiH}_x)\text{SiH}_3 + \text{SiH}_y \rightarrow \text{SiH}_x + (\text{SiH}_y)\text{SiH}_3$	Hopping of Phys on hyd	$\nu_{hx}$	$E_{hx}$	$\nu_{hx} \cdot \theta_4 \cdot \theta_1$
I	$2(\text{SiH}_x)\text{SiH}_3 \rightarrow 2\text{SiH}_x + \text{Si}_2\text{H}_6(\text{g})$	Desorption of 2 Phys $\text{SiH}_3$	$\nu_{d2}$	$E_{d2}$	$\nu_{d2} \cdot \theta_4 \cdot \theta_4$
J	$(\text{SiH}_x) + (\text{SiH}_y) \rightarrow (\text{SiH}_{x-1})^- (\text{SiH}_{y-1}) + \text{H}_{2(\text{g})}$	Recombination of Hydrides	$\nu_{pxy}$	$E_{pxy}$	$\nu_{pxy} \cdot \theta_x \cdot \theta_y$
K	$\text{Si}^-\text{Si} + \text{SiH}_3(\text{g}) \rightarrow \text{SiSiH}_3 + \text{Si}^-$	$\text{SiH}_3$ insertion in Si-Si	$\nu_{i1}$	$E_{i1}$	$\nu_{i1} \cdot \phi_{\text{Si}} \cdot f \cdot \theta_5$
L	$\text{Si}^-\text{Si} + \text{H}_3\text{Si}(\text{SiH}_x) \rightarrow 2\text{SiSiH}_n + \text{Si}^-$	Insertion of Phys $\text{SiH}_3$	$\nu_{i3}$	$E_{i3}$	$\nu_{i3} \cdot \theta_4 \cdot f \cdot \theta_5$
M	$(\text{SiH}_x) + (\text{SiH}_y) \rightarrow 2(\text{SiH}_z)^- + \text{H}_2(\text{g})$	Recomb of Hyd. forming db	$\nu_{r1}$	$E_{r1}$	$\nu_{r1} \cdot \theta_x \cdot \theta_y$

Table 6.1(a): List of Reactions (and the corresponding rate expressions) used in the model.

<b>Reaction</b>	<b>Parameter values</b>			
A	$s_0$	0.25		
B	$s_1$	0.25		
C	$s_2$	0.1		
D	$A_{a1}$	0.25	$E_{a1}$	0.4 eV
E	$A_{d1}$	$k_B T/h$	$E_{d1}$	0.7 eV
F	$A_{a3}$	$0.1k_B T/h$	$E_{a3}$	0.4 eV
G	$A_h$	$k_B T/h$	$E_h$	0.3eV
H <sub>1</sub>	$A_{h1}$	$k_B T/h$	$E_{h1}$	0.2eV
H <sub>2</sub>	$A_{h2}$	$k_B T/h$	$E_{h2}$	0.3 eV
H <sub>3</sub>	$A_{h3}$	$k_B T/h$	$E_{h3}$	0.3 eV
I	$A_{d2}$	$k_B T/h$	$E_{d2}$	0.7 eV
J <sub>11</sub>	$A_{p11}$	$10^{-10}k_B T/h$	$E_{p11}$	0.6 eV
J <sub>12</sub>	$A_{p12}$	$10^{-10}k_B T/h$	$E_{p12}$	0.45 eV
J <sub>13</sub>	$A_{p13}$	$10^{-10}k_B T/h$	$E_{p13}$	0.35 eV
J <sub>22</sub>	$A_{p22}$	$10^{-10}k_B T/h$	$E_{p22}$	0.3 eV
J <sub>23</sub>	$A_{p23}$	$10^{-10}k_B T/h$	$E_{p23}$	0.25 eV
J <sub>33</sub>	$A_{p33}$	$10^{-10}k_B T/h$	$E_{p33}$	0.2 eV
K	$A_{i1}/s$	0.25	$E_{i1}$	0.5 eV
L	$A_{i3}$	$k_B T/h$	$E_{i3}$	0.7 eV
M	$A_{r1}$	$k_B T/h$	$E_{r1}$	1.9 eV

Table 6.1(b): List of Reaction Rate parameters used in the model. The rate constants,  $\mathbf{u}_n$ , are given as  $A_n \exp(-E_n/k_B T)$ , here  $k_B$  is the Boltzmann's constant and  $h$  is Planck's constant.

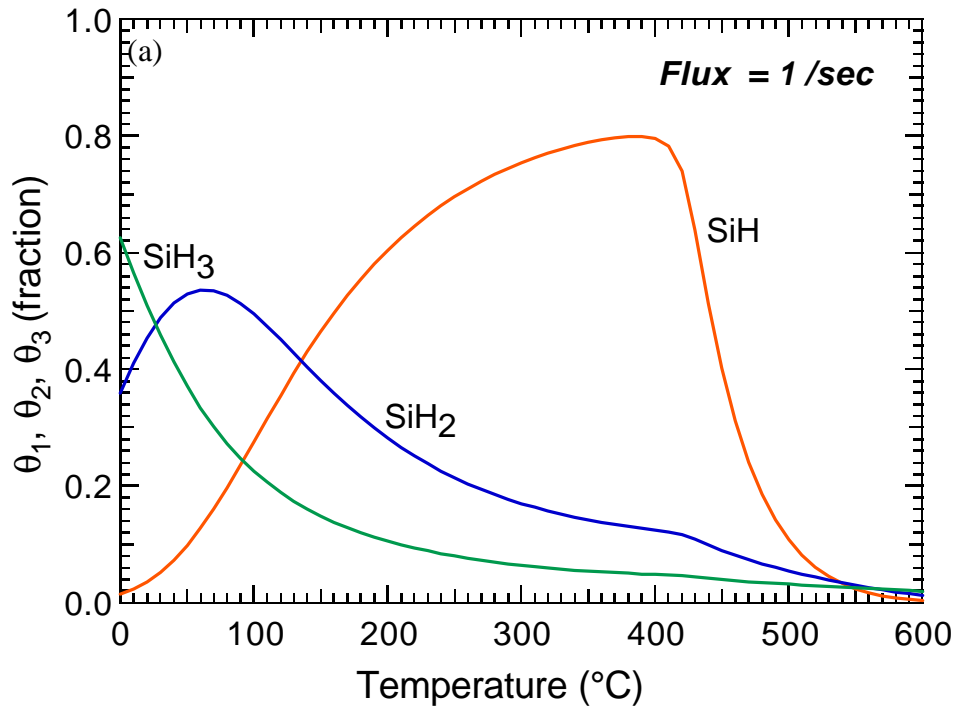


Fig. 6.1(a): Distribution of different surface hydrides vs. temperature for  $E_a(\text{abs}) = 0.4$  eV for Flux =1/sec.

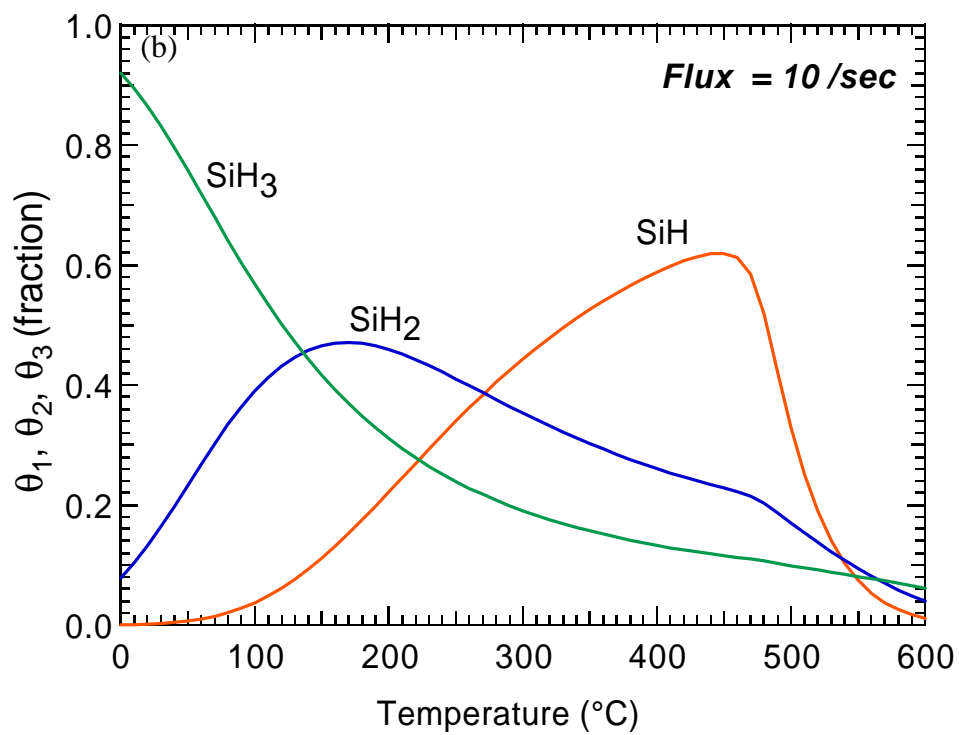


Fig. 6.1(b): Distribution of different surface hydrides vs. temperature for  $E_a(\text{abs}) = 0.4$  eV for Flux = 10/sec.

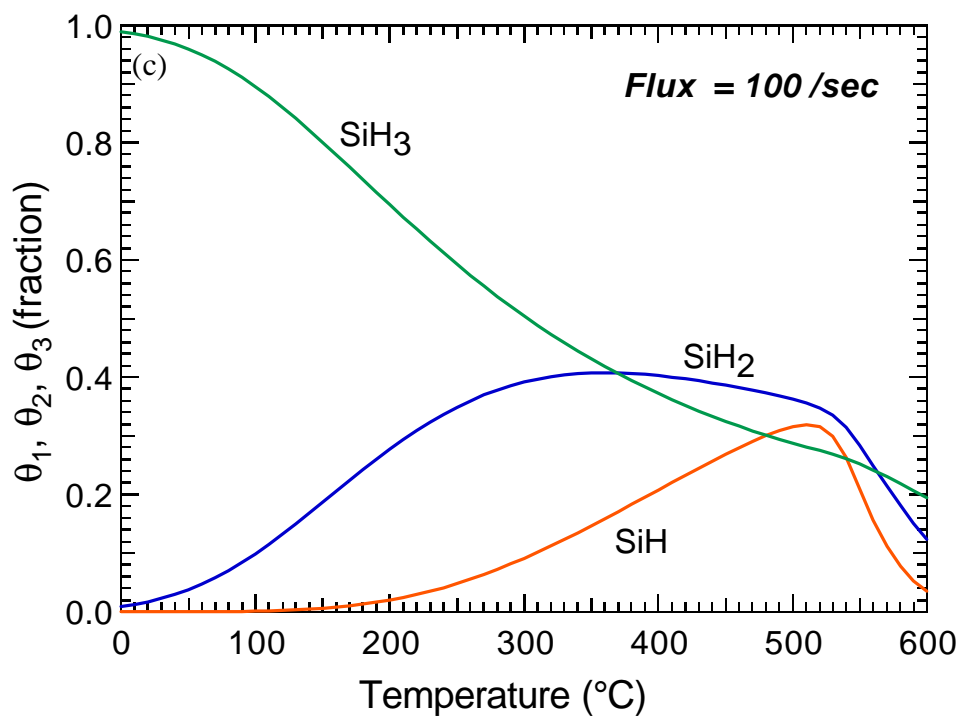


Fig. 6.1(c): Distribution of different surface hydrides vs. temperature for  $E_a(\text{abs}) = 0.4$  eV for Flux = 100/sec.

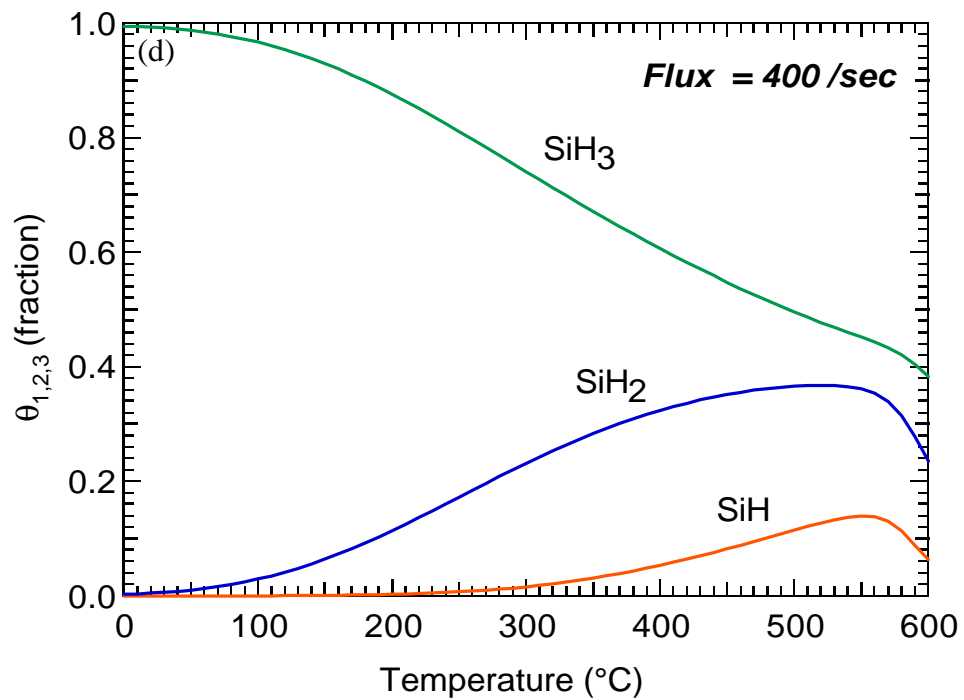


Fig. 6.1(d): Distribution of different surface hydrides vs. temperature for  $E_a(\text{abs}) = 0.4$  eV for Flux = 400/sec.

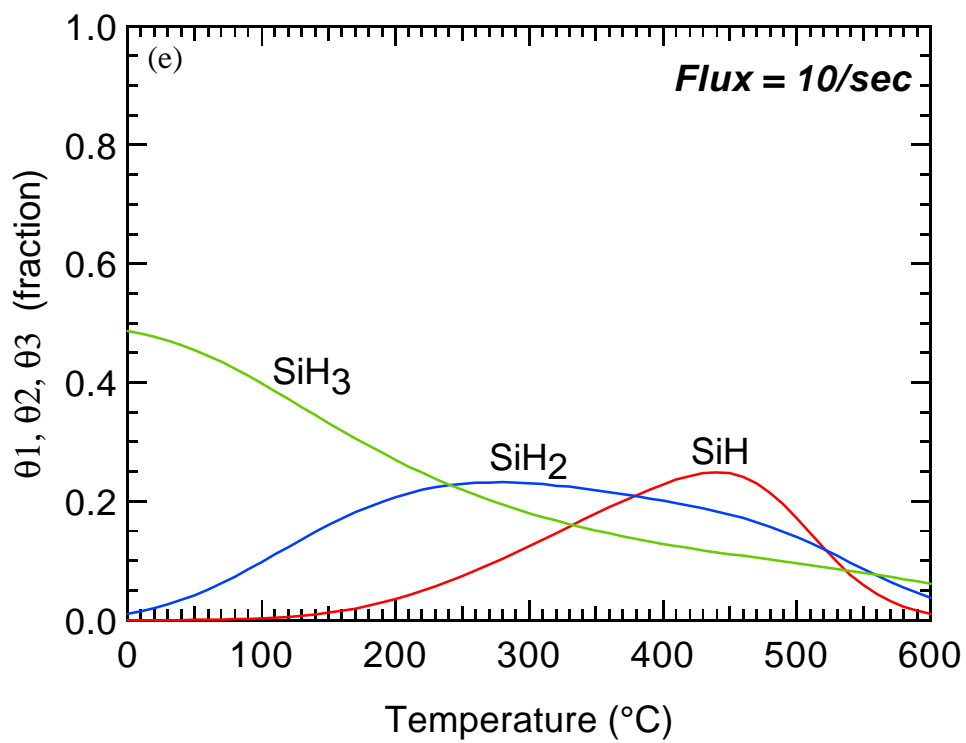


Fig. 6.1(e): Distribution of different surface hydrides vs. temperature for  $E_a(\text{abs}) = 0.1$  eV for Flux = 10/sec.

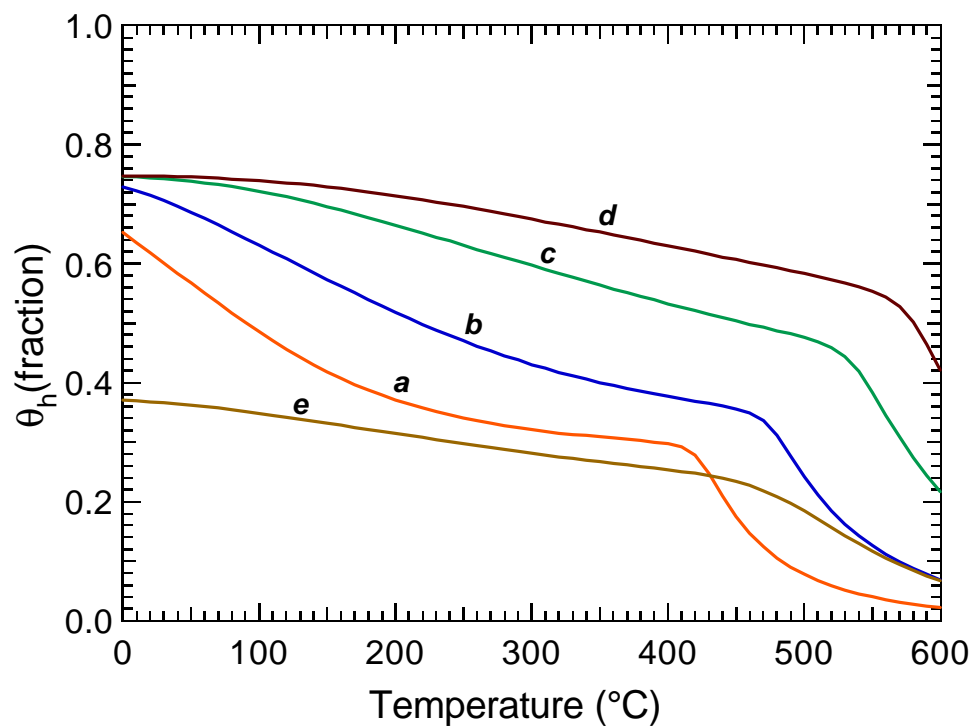


Fig. 6.2: Variation of surface layer H content with temperature for varying silyl radical flux. (a) Flux = 1/sec, (b) Flux = 10/sec, (c) Flux = 100/sec, (d) Flux = 400/sec for  $E_a(\text{abs}) = 0.4$  eV and (e) Flux = 10/sec and  $E_a(\text{abs}) = 0.1$  eV.

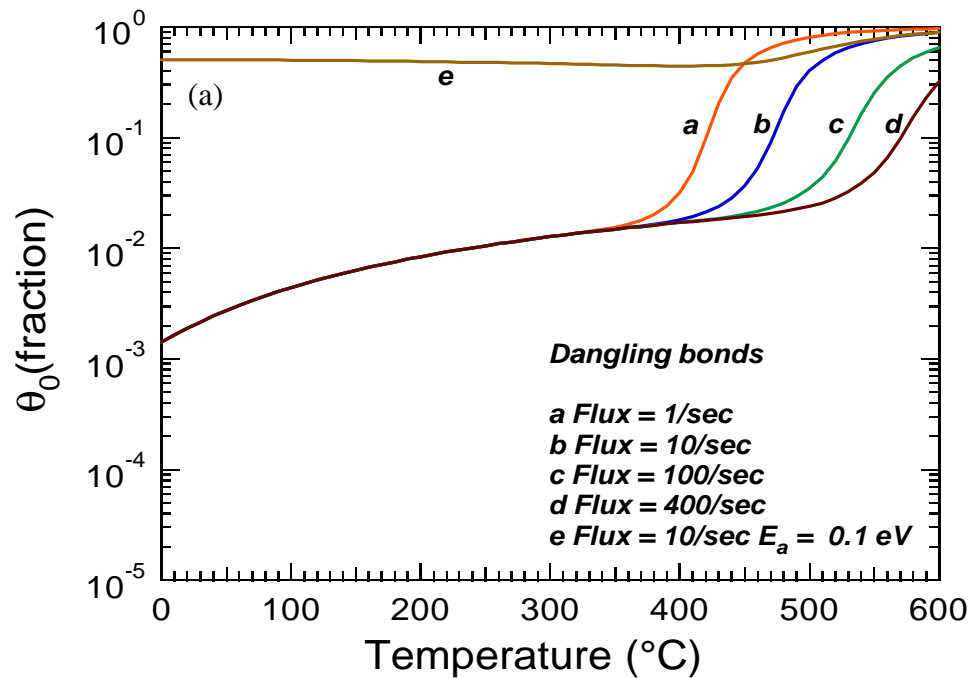


Fig. 6.3(a): Effect of temperature on the surface dangling bond concentrations. Overall surface dangling bond concentration vs. temperature for silyl radical flux (a) Flux = 1/sec, (b) Flux = 10/sec, (c) Flux = 100/sec and (d) Flux = 400/sec for  $E_a(\text{abs}) = 0.4$  eV and (e) Flux = 10/sec and  $E_a(\text{abs}) = 0.1$  eV.

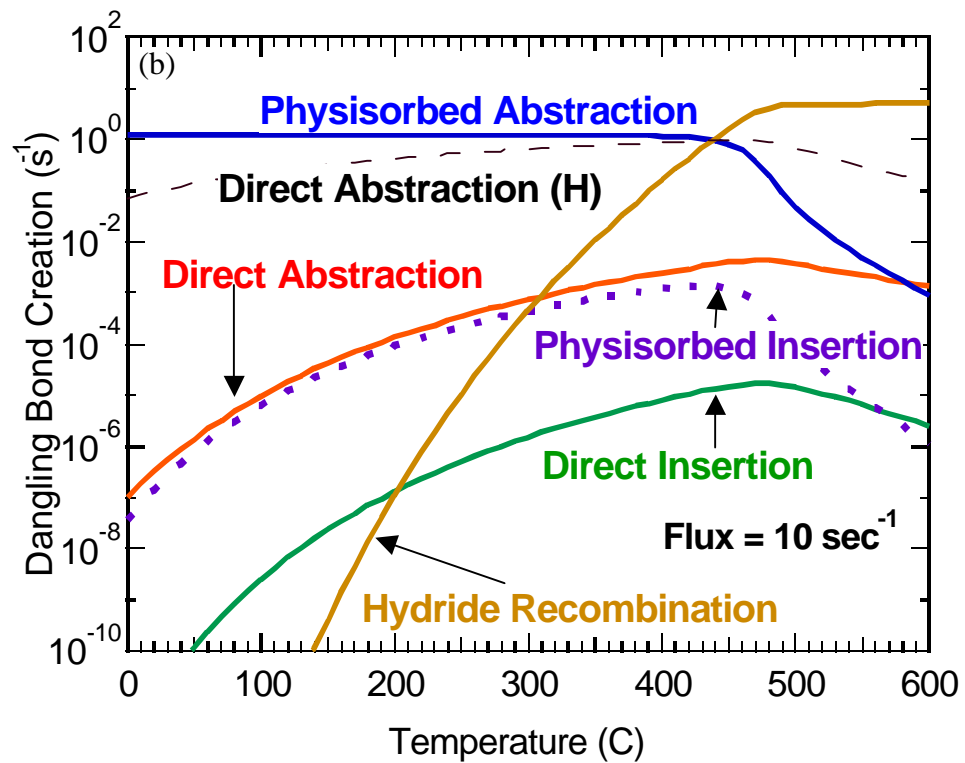


Fig. 6.3(b): Effect of temperature on the surface dangling bond concentrations.

Contribution of individual mechanisms to dangling bond creation, including creation of dangling bonds by direct H abstraction by H, assuming H flux equal to silyl flux for  $E_a(\text{abs}) = 0.4 \text{ eV}$ .

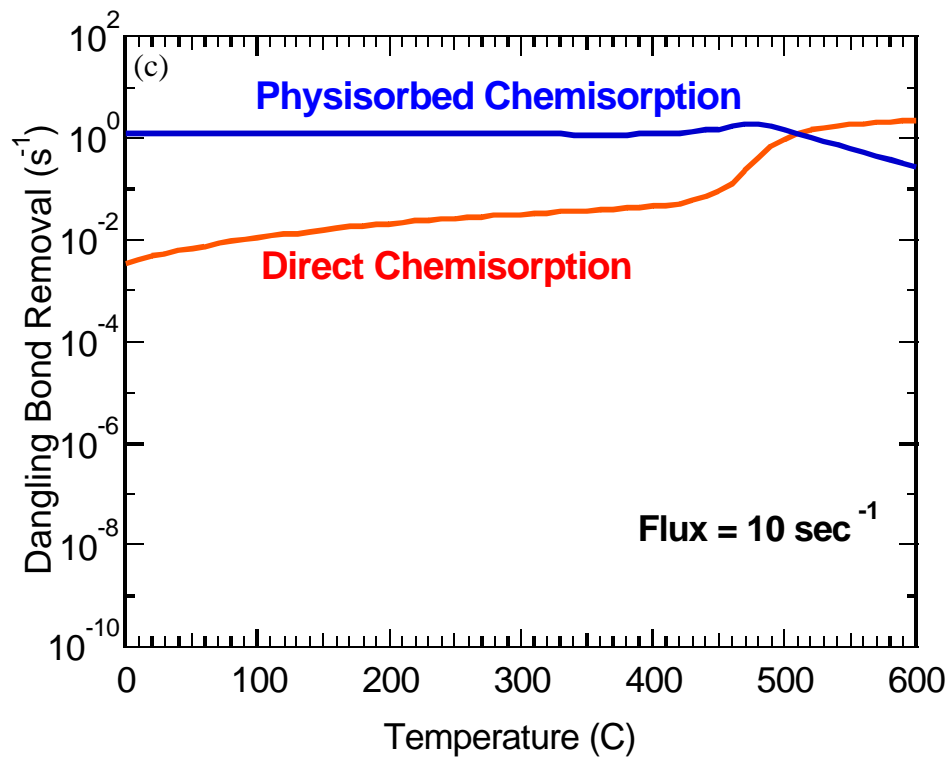


Fig. 6.3(c): Effect of temperature on the surface dangling bond concentrations.

Contribution of individual mechanisms to dangling bond removal for  $E_a(\text{abs}) = 0.4 \text{ eV}$ .

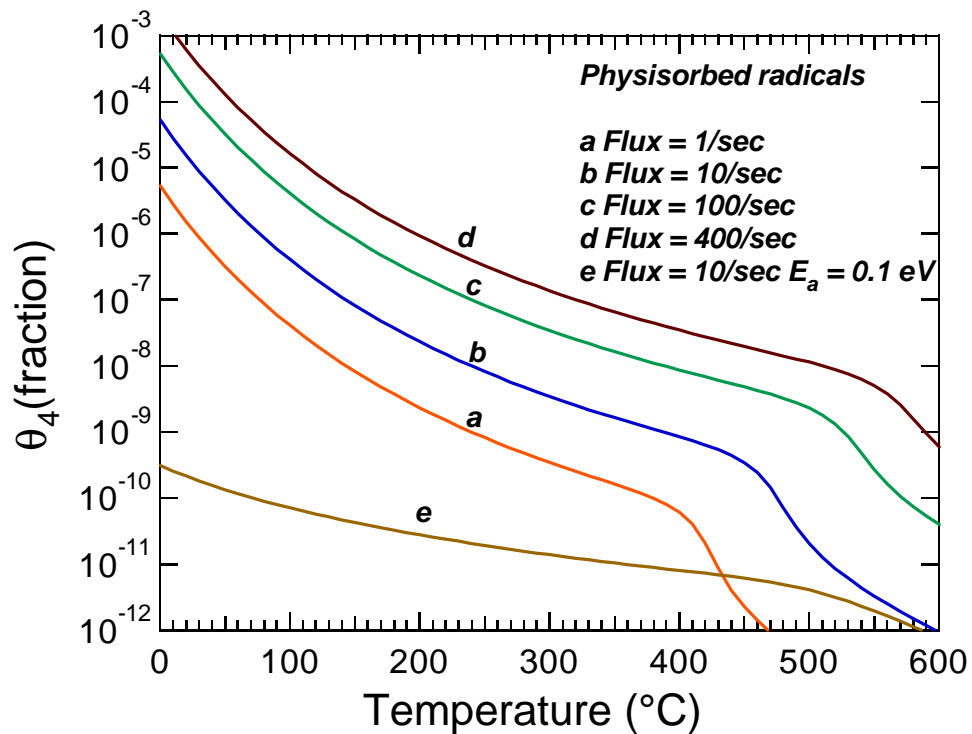


Fig 6.4: Effect of temperature on the surface coverage of physisorbed radicals for varying silyl radical flux with  $E_a(\text{abs}) = 0.4$  eV (a) Flux = 1/sec, (b) Flux = 10/sec, (c) Flux = 100/sec and (d) Flux = 400/sec and (e) Flux = 10/sec with  $E_a(\text{abs}) = 0.1$  eV.

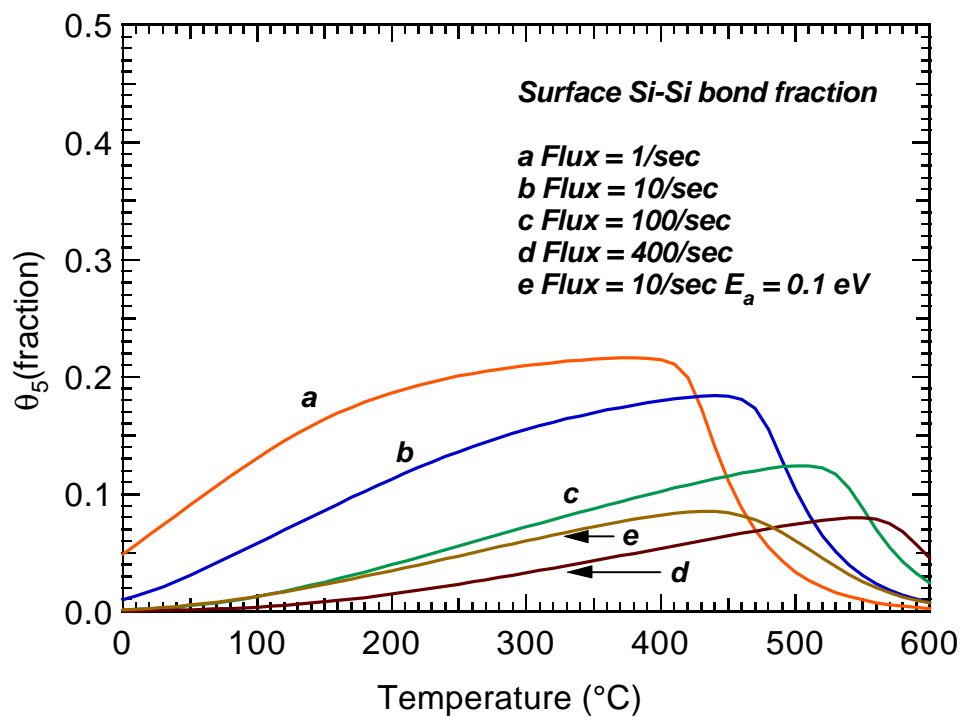


Fig. 6.5: Surface Si-Si bond ( $\theta_5$ ) fraction vs. temperature for varying silyl radical flux with  $E_a(\text{abs}) = 0.4$  eV (a) Flux = 1/sec, (b) Flux = 10/sec, (c) Flux = 100/sec and (d) Flux = 400/sec and (e) Flux = 10/sec with  $E_a(\text{abs}) = 0.1$  eV.

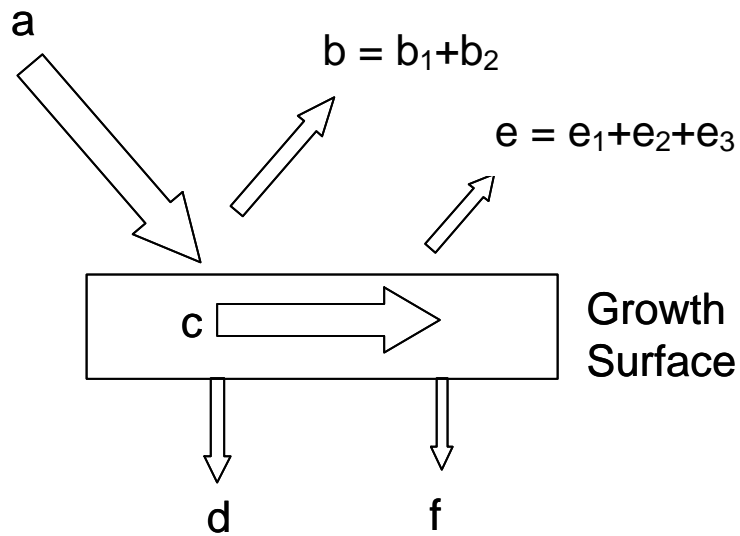


Fig. 6.6: Schematic of various reaction and sticking probabilities on the surface.

Probabilities associated with various events

a : Incoming Silyl Flux (=1)

b<sub>1</sub> : Reflection of SiH<sub>3</sub>

b<sub>2</sub> : Direct H abstraction by SiH<sub>3</sub>

c : Physisorption of Silyl radicals

d : Direct incorporation of Silyl radicals through chemisorption or insertion (*s<sub>a</sub>*)

e<sub>1</sub> : Recombination of two physisorbed Silyl radicals as Si<sub>2</sub>H<sub>6</sub>

e<sub>2</sub> : Desorption of physisorbed Silyl radical as SiH<sub>3</sub>

e<sub>3</sub> : H abstraction by physisorbed Silyl radical

f : Incorporation of physisorbed radical through chemisorption or insertion (*s<sub>b</sub>*)

$$1 - \beta = b_1 + e_2$$

$$\gamma = b_2 + e_1 + e_3$$

$$s = d + f$$

$$\beta = s + \gamma$$

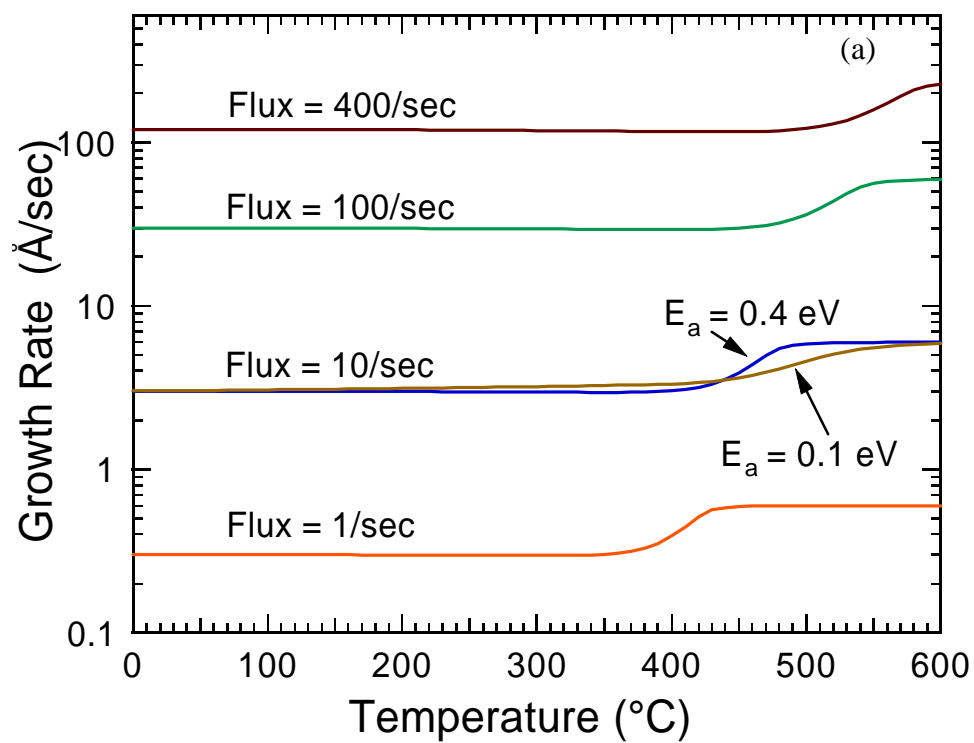


Fig. 6.7(a): Growth rate variations with deposition conditions (temperature, silyl radical flux and hydrogen abstraction barrier).

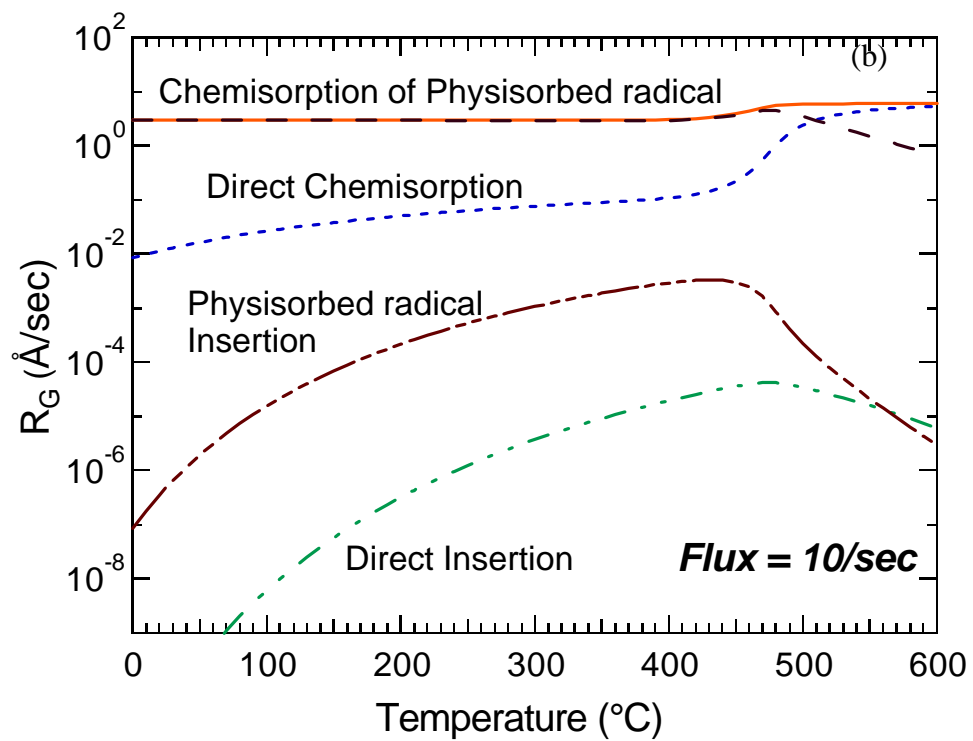


Fig 6.7(b): Contribution of different incorporation pathways to growth rate for Flux = 10/sec and  $E_a(\text{abs}) = 0.4$  eV.

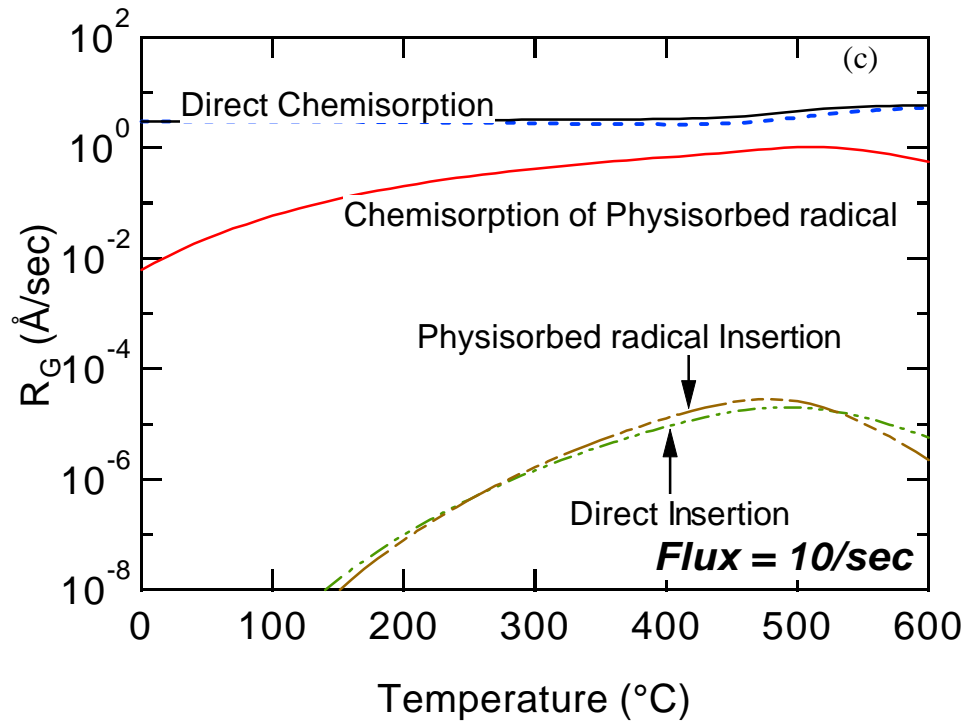


Fig 6.7(c): Contribution of different incorporation pathways to growth rate for Flux = 10/sec and  $E_a(\text{abs}) = 0.1$  eV.

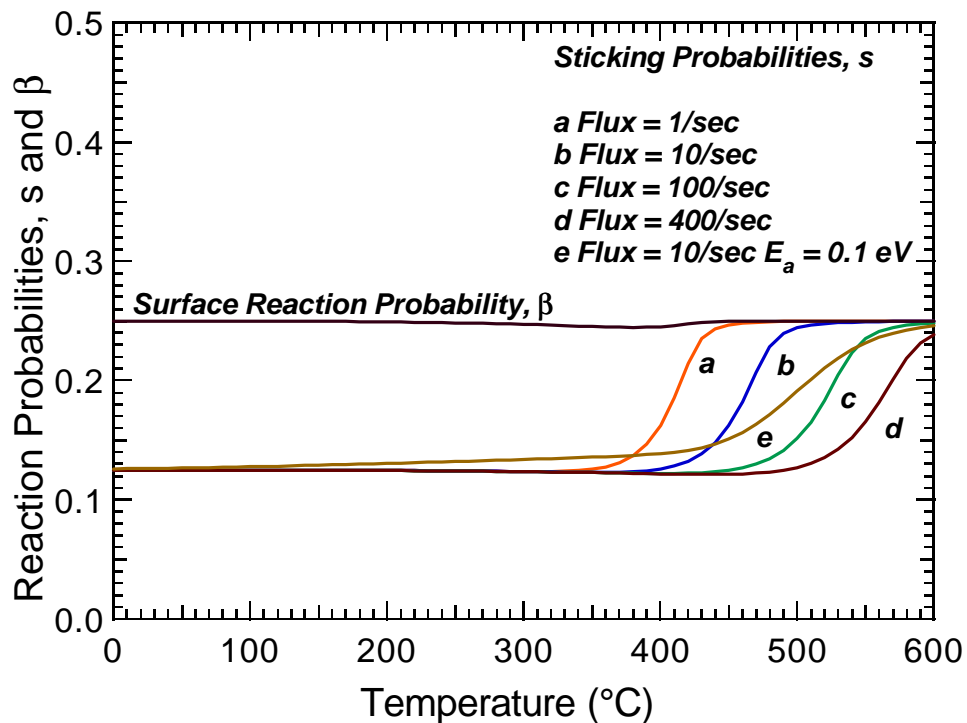


Fig. 6.8: Reaction and sticking probabilities ( $\beta$  and  $s$ ) predicted by the kinetic model vs. temperature for varying silyl radical flux with  $E_a(\text{abs}) = 0.4$  eV. (a) Flux = 1/sec, (b) Flux = 10/sec, (c) Flux = 100/sec, and (d) Flux = 400/sec and (e) Flux = 10/sec with  $E_a(\text{abs}) = 0.1$  eV.

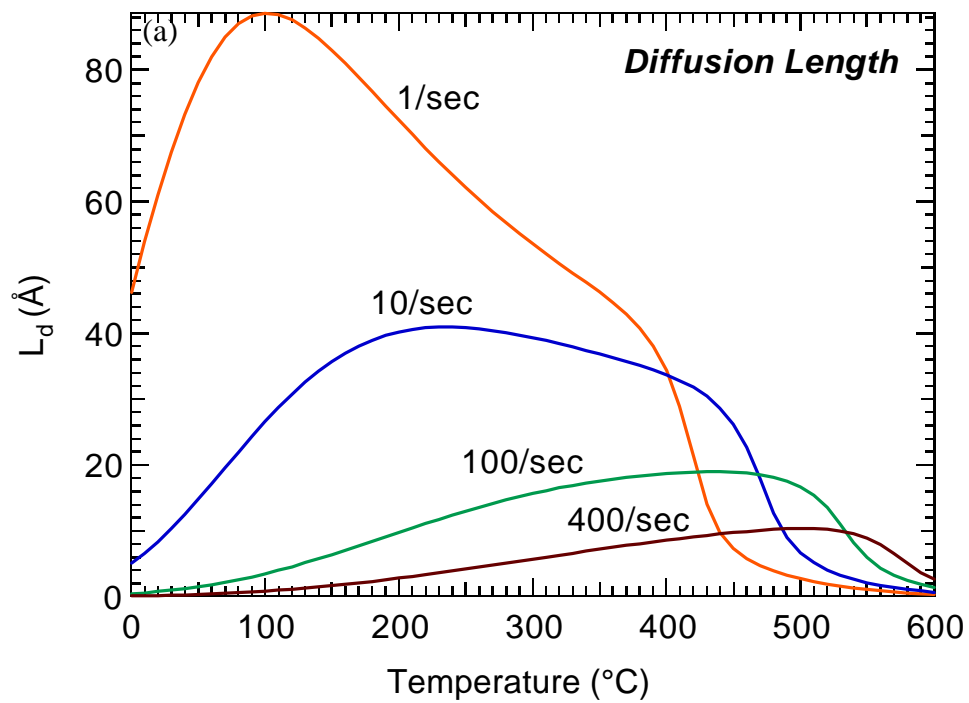


Fig. 6.9(a): Diffusion length vs. temperature for varying silyl radical flux with  $E_a(\text{abs}) = 0.4 \text{ eV}$ .

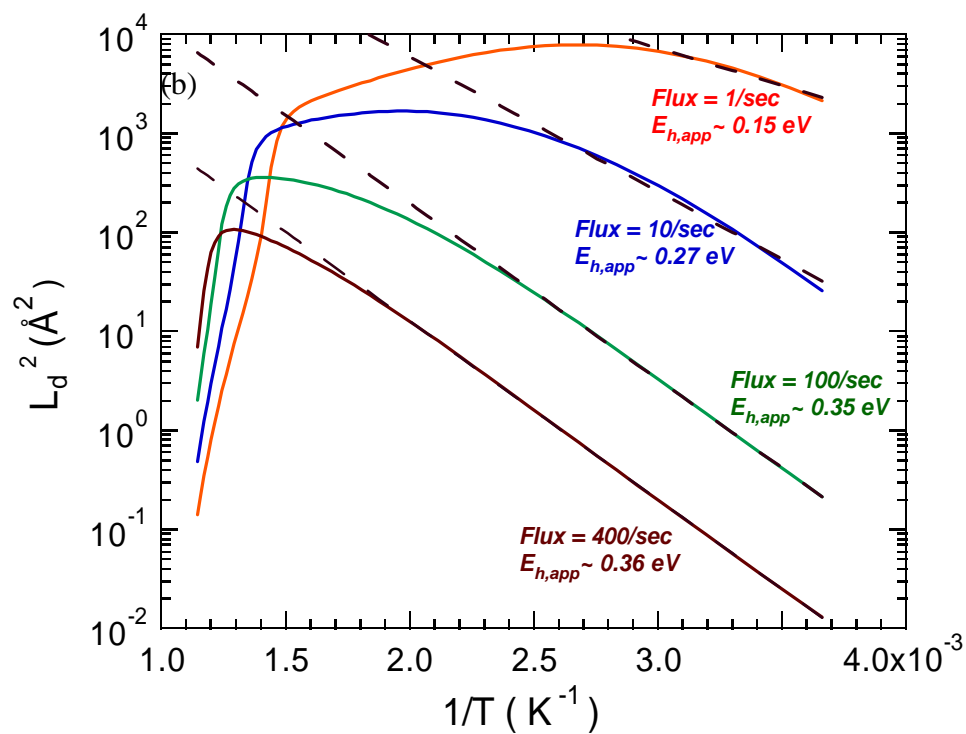


Fig. 6.9(b): Semi-log plot of  $L_d^2$  vs  $1/T$  to calculate the apparent activation barriers for the diffusion of physisorbed radicals on the surface for varying silyl radical flux with  $E_a(\text{abs}) = 0.4$  eV.

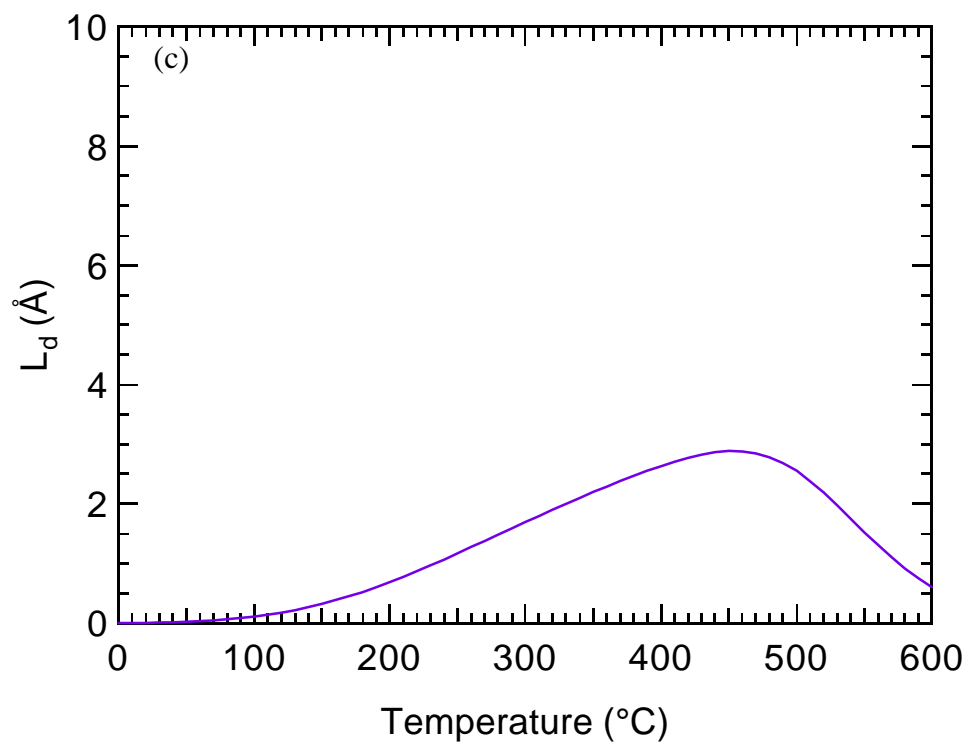


Fig. 6.9(c): Diffusion length vs. temperature for silyl radical flux = 10/sec with  $E_a(\text{abs}) = 0.1$  eV.

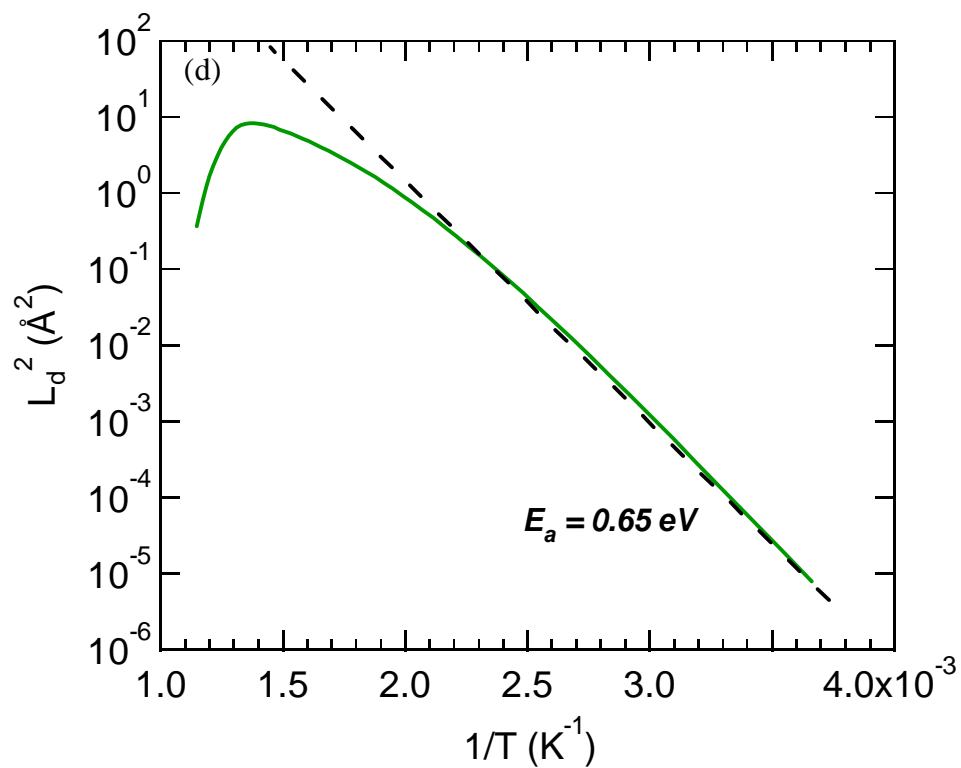


Fig 6.9(d): Semi-log plot of  $L_d^2$  vs  $1/T$  to calculate the apparent activation barriers for the diffusion of physisorbed radicals on the surface for silyl radical flux = 10/sec with  $E_a(\text{abs}) = 0.1 \text{ eV}$ .

*Chapter 7 is a draft of a manuscript to be submitted for publication.*

## **CHAPTER 7**

### **7 INTRINSIC DIFFUSIVITY OF SILICON ON SILICON**

by: Kevin .R. Bray<sup>1</sup>, Andrew S. Dalton<sup>2</sup>, Diana Llera-Hurlburt<sup>2</sup>, Edmund G. Seebauer<sup>2</sup>,  
and Gregory N. Parsons<sup>1</sup>

<sup>1</sup>*Department of Chemical Engineering, North Carolina State University, Raleigh, NC,  
27695-7905*

<sup>2</sup>*Department of Chemical Engineering, University of Illinois, Urbana, IL, 61801*

#### **ABSTRACT**

Intrinsic diffusivity of silicon on silicon is studied using hemispherical grained silicon. Fractal analysis of the surface topography is used to extract scaling coefficients from the surface topography. Images of the surface topography obtained from atomic force microscopy are examined using dimensional fractal analysis and the static scaling coefficient and lateral correlation length are extracted from the analysis. Two regimes are seen on the surface: (a) large hemispherical grains and (b) smooth amorphous regions between the grains. The static scaling coefficient confirms that surface diffusion is

controlling the surface transport and the correlation length is used to estimate a diffusion barrier of 0.88 eV. Comparison of the scaling analysis with parameters from thin film growth and step edge diffusion indicates that the diffusion barrier measured corresponds to the intrinsic site-to-site hopping barrier on the surface.

## 7.1 INTRODUCTION

Surface transport plays an important role in a wide variety of technological processes. A current challenge in materials processing is to understand the kinetics of the surface processes to control surface reactions and improve material properties. Models based on thermodynamic balances only apply in the equilibrium limit. This limit is impractical for current technology where high deposition rates and low deposition temperatures require processing far from equilibrium. These deposition conditions lead towards the use of amorphous materials. Amorphous materials are structurally and energetically heterogeneous, and these properties may change the surface properties compared to those of the crystalline material [1]. Hemispherical grained silicon (HSG) provides a unique opportunity to study surface diffusion on amorphous materials. HSG forms by surface-diffusion-driven crystallization of a-Si that begins at the free surface above about 600°C. The crystallites mushroom out of the surface as small grains up to 100 nm in size. Since the grain shape is roughly size-invariant, the growth is limited by diffusion over the a-Si surface [1, 2].

Surface diffusion can be divided into two terms, intrinsic diffusivity,  $D_I$ , which describes site-to-site hopping of individual atoms and mass transfer diffusivity,  $D_M$ , which includes the creation and removal of mobile species [3, 4]. The two quantities are related by the surface coverage of mobile atoms,  $\theta$  by the expression:

$$D_M = \theta D_I \quad (1)$$

Correlations of HSG grain size with anneal time and temperature have been used to extract kinetic transport parameters from these surfaces [1, 2]. The growth of HSG grains

was related to the flux of silicon impinging on the grains, which was a function of grain size and anneal time. But differences between the anneal time of the sample and characteristic decay time of the silicon flux did not allow a unique solution to be obtained for intrinsic diffusivity. Using a steady state approximation for the silicon flux across the surface, mass transfer diffusivity parameters were estimated from a fit of the time and temperature dependence of the HSG grain size [1].

Surface topography can also be used to gain insight into transport kinetics during film growth [5-11]. Fractal analysis of the surface results in the determination of the static and dynamic scaling coefficients,  $\alpha$  and  $\beta$ , and the lateral correlation length,  $L_c$ . The static scaling coefficient relates how the root-mean-square (RMS) roughness changes with the length area over which it is measured. The dynamic scaling coefficient correlates the RMS roughness and film thickness. Measurement of these parameters allows surface transport mechanisms, including viscous flow, evaporation/condensation, bulk diffusion, and surface diffusion to be differentiated and identified [7, 12, 13]. Under conditions where surface diffusion dominates the transport mechanisms, the lateral correlation length can be used as an estimate of the diffusion length. Kinetic parameters have been extracted using  $L_c$  for physical vapor deposition of glassy metals [11] and plasma enhanced chemical vapor deposition of hydrogenated amorphous silicon [7, 8]. These surface analysis techniques will now be applied to study intrinsic diffusion of amorphous silicon during HSG silicon growth.

## 7.2 EXPERIMENTAL METHOD

In this letter, HSG silicon was grown by first depositing a uniform amorphous silicon film. The amorphous silicon was then seeded with disilane at 650°C for 40 seconds. The samples were subsequently annealed at temperatures ranging from 635°C to 655°C for 60 – 65 seconds. HSG grains blossomed out of the smooth amorphous silicon layer. Surface topography of the HSG films was characterized using atomic force microscopy (AFM). All AFM measurements were performed under ambient conditions. Image areas of 200nm x 200nm, 500nm x 500nm, and 5 $\mu$ m x 5 $\mu$ m were studied. Dimensional fractal analyses were used to extract the static scaling coefficient and the lateral correlation length from the topography data.

## 7.3 RESULTS

The topography of an HSG surface annealed at 655°C for 65 seconds is shown in Fig. 7.1. Two distinct surface features can be identified: (a) large hemispherical grains and (b) areas of flat, smooth amorphous silicon. Similar features were seen on samples annealed at other temperatures. Dimensional analysis was applied to the two sections of the surface separately. Analysis of section (a) utilized the complete 5 $\mu$ m x 5 $\mu$ m topography image including the HSG grains and the areas between. For analysis of section (b), smaller 200nm x 200nm and 500nm x 500nm AFM scans were taken in the different regions of smooth amorphous silicon surfaces located between the large HSG grains. Figure 7.2 is a dimensional analysis, plotting the RMS roughness vs.

measurement length from both sections (a) and (b) for films annealed from 635°C to 655°C. The roughness increases with measurement length until it reaches a saturation value. The lateral correlation length,  $L_c$ , is the distance at which the surface roughness first reaches saturation and is approximately 500 – 700 nm for section (a) and 45 – 55 nm for section (b) and increases with increasing anneal temperature. The surface in region (a) is dominated by the presence of the hemispherical grains. This leads to large roughness values and long correlation lengths. The grains cause large changes in the local slope on the surface. The fractal analysis utilized here requires small variations in the local slope on the surface [13], therefore this technique is not valid for directly studying the HSG grains in region (a). However, section (b) avoids the HSG grains and shows a smooth surface with small local variation. This region is suitable for a fractal evaluation of the surface.

The static scaling coefficient,  $\alpha$ , is extracted as the slope of the initial plots in Fig. 7.2. Figure 7.3 compares  $\alpha$  for the different anneal temperatures studied. A constant value of  $\alpha = 0.78$  is obtained across the entire temperature range. This value falls within the range of 0.7 – 1.0 reported for surface diffusion processes [5, 7, 8, 12, 13] and is consistent with the assumption that surface diffusion across the amorphous surface controls the HSG growth [1, 2]. The constant value for  $\alpha$  indicates that the same process is occurring at all temperatures. Since surface diffusion is the dominant transport mechanism, the correlation length can be used as an estimated of the diffusion length [7, 8].  $L_c$  was measured for a series of temperatures and the diffusion activation barrier was estimated from the Arrhenius plot of  $L_c^2$  vs.  $1/T$  shown in Fig. 7.4. A diffusion barrier of  $E_a = 0.88 \pm 0.38$  eV is obtained from a best fit of the data in Fig. 7.4.

## **7.4 DISCUSSION**

Previous studies of HSG silicon relied on fits of grain size with anneal time and temperature to extract kinetic parameters [1, 2]. These models were able to estimate mass transfer diffusivity parameters, but could not directly measure diffusion on the surface. Surface fractal analysis is usually used to describe growth processes where mobile species arrive on the surface from the gas phase [6, 7, 11, 13]. In these situations, the barriers being measured correspond with site-to-site hopping and represent intrinsic diffusivity values. The static scaling coefficient for the HSG silicon growth has a similar value as that for surface diffusion during film growth, which measures intrinsic diffusivity. This similarity implies the kinetic transport parameters extracted from the dynamic surface analysis represent the intrinsic diffusion barrier for silicon diffusion across amorphous silicon.

## **7.5 CONCLUSIONS**

The results presented here provide important insight in the intrinsic diffusion of silicon on silicon. Hemispherical grained silicon growth is known to proceed through a surface diffusion controlled mechanism. Fractal topography analysis parameters also confirm that surface diffusion is controlling the surface structure. The consistency between the scaling coefficients measured on HSG silicon and those from thin film deposition processes indicate that the diffusion barriers obtained correspond to site-to-site

intrinsic hopping of the diffusing atoms. Diffusion activation barriers based on the lateral correlation length show an intrinsic barrier of  $\sim 0.9$  eV.

## **7.6 ACKNOWLEDGEMENTS**

This work was supported under NSF Grant No. 0072784 and DARPA.

## 7.7 REFERENCES

- [1] A.S. Dalton, D. Llera-Hurlburt, and E.G. Seebauer, *Surface Science*, **494**, L761 (2001).
- [2] A. Sakai, T. Tatsumi, and K. Ishida, *Journal of Vacuum Science and Technology A*, **11**, 2950 (1993).
- [3] E.G. Seebauer and C.E. Allen, *Progress in Surface Science*, **49**, 265 (1995).
- [4] C.E. Allen, R. Ditchfield, and E.G. Seebauer, *Physical Review B*, **55**, 13304 (1997).
- [5] D.M. Tanenbaum, A.L. Laracuente, and A. Gallagher, *Physical Review B*, **56**, 4243 (1997).
- [6] W.M. Tong, E.J. Snyder, and R.S. Williams, *Surface Science*, **277**, L63 (1992).
- [7] K.R. Bray and G.N. Parsons, *Physical Review B*, **65**, 035311 (2002).
- [8] K.R. Bray, A. Gupta, and G.N. Parsons, *Applied Physics Letters*, **80**, 2356 (2002).
- [9] M. Kondo, T. Ohe, K. Saito, T. Nishimiya, and A. Matsuda, *Journal of Non-Crystalline Solids*, **227-230**, 890 (1998).
- [10] L. Bardotti, C.R. Stoldt, C.J. Jenks, M.C. Bartlet, J.W. Evans, and P.A. Thiel, *Physical Review B*, **57**, 12544 (1998).
- [11] B. Reinker, M. Moske, and K. Samwer, *Physical Review B*, **56**, 9887 (1997).
- [12] W.M. Tong and R.S. Williams, *Annual Review of Physical Chemistry*, **45**, 401 (1994).
- [13] A.L. Barabasi and H.E. Stanley, *Fractal Concepts in Surface Growth* (Cambridge UP, Cambridge, 1995).

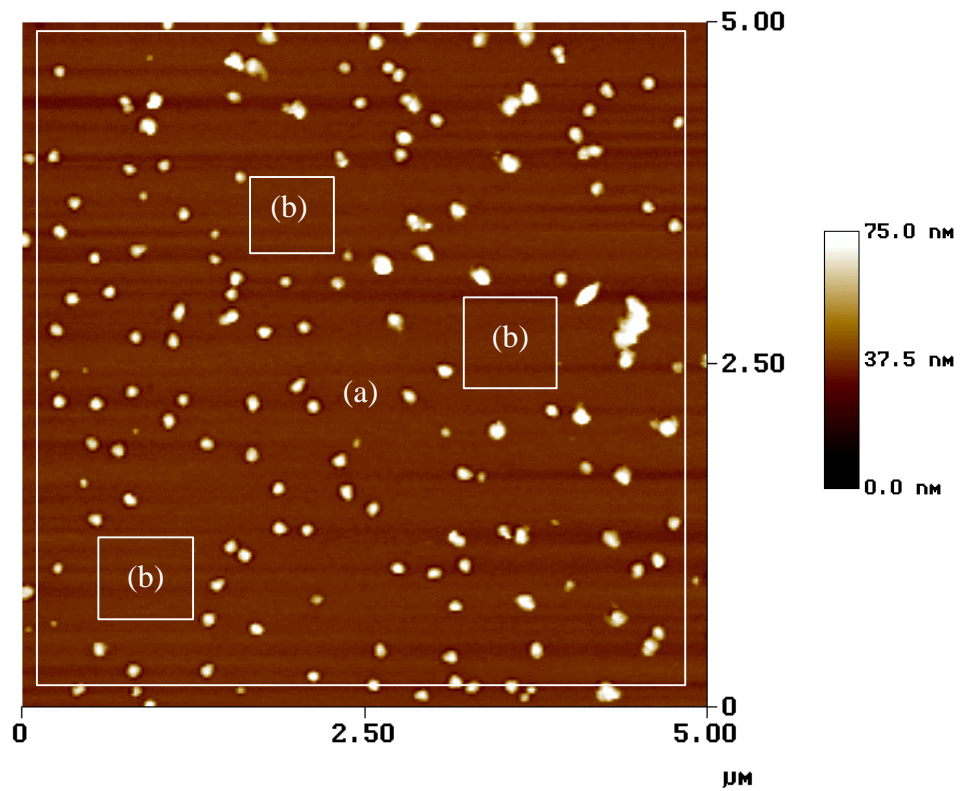


Fig. 7.1: Atomic force microscopy image of HSG silicon surface. Two regions of the surface are observed. Region (a) consists of several large HSG grains and region (b) consists of the smooth, amorphous silicon between the grains.

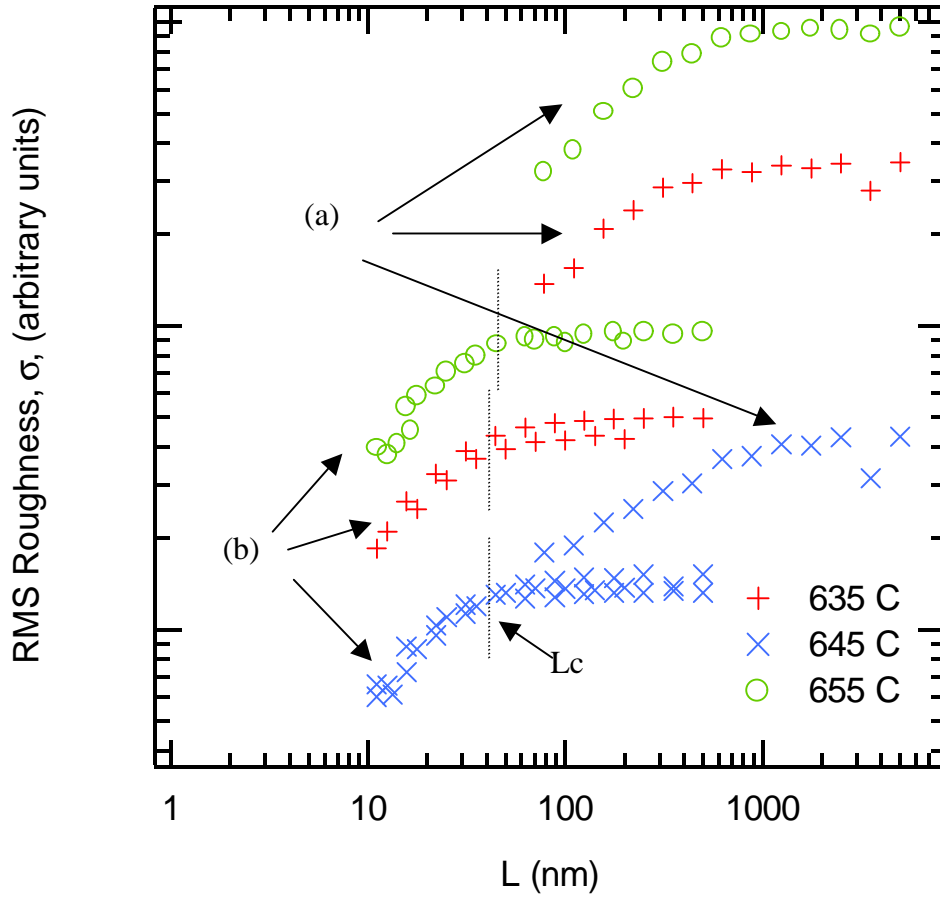


Fig. 7.2. Dimensional fractal analysis of HSG silicon regions (a) and (b). RMS Roughness increases with measurement length and then saturates.

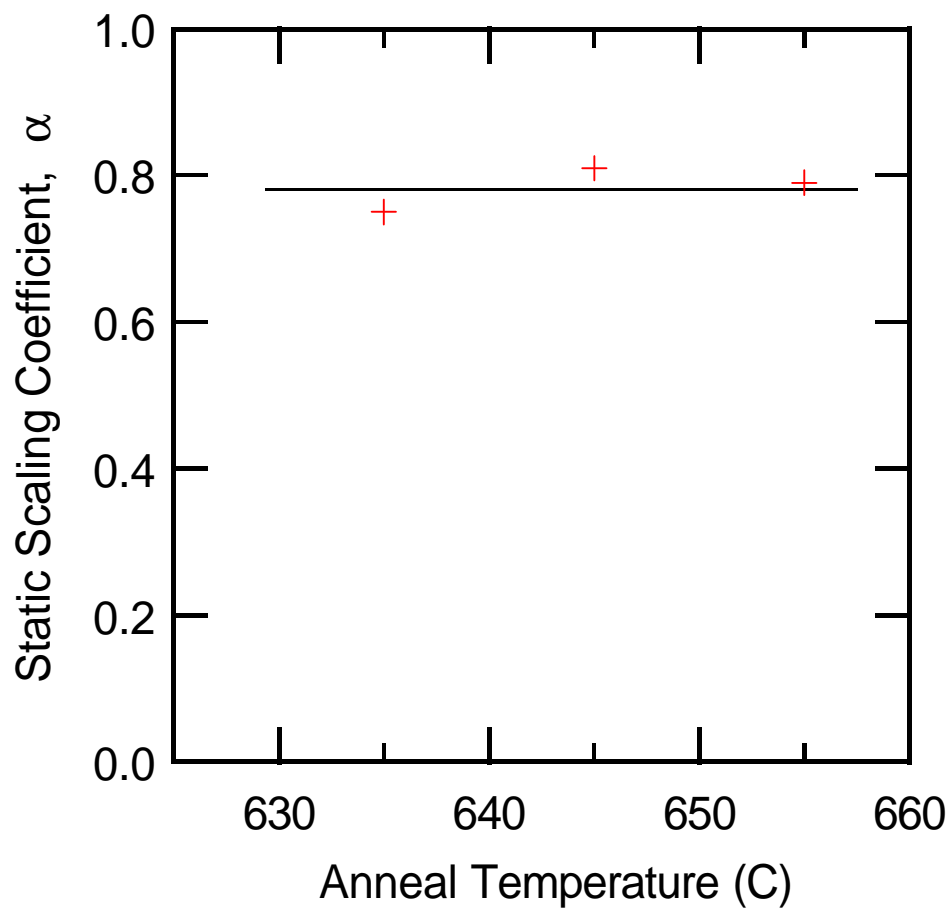


Fig. 7.3. Static scaling coefficient,  $\alpha$ , vs. anneal temperature.  $\alpha$  remains constant with temperature.

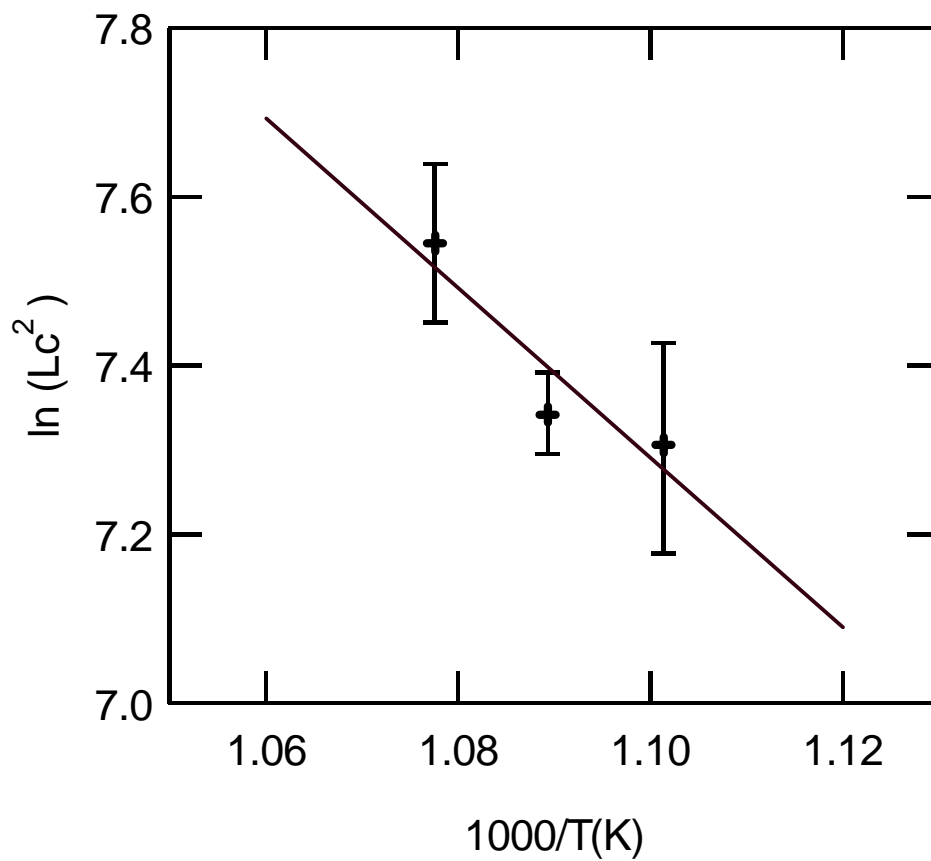


Fig. 7.4. Arrhenius plot of  $L_c^2$  vs.  $1/T$  for correlation length obtained from region (b).

Diffusion barrier of  $E_a = 0.88 \pm 0.38$  eV is obtained from a best fit of the data.

## CHAPTER 8

### 8 CONCLUSIONS AND FUTURE STUDIES

#### 8.1 CONCLUSIONS

##### 8.1.1 Dynamic Scaling

We have demonstrated that dynamic scaling provides insight into the growth of amorphous silicon. The evolution of the surface roughness has been used to identify the surface transport mechanisms active during film growth and to extract kinetic parameters from this data. The scaling coefficients can be used to distinguish between films deposited through different techniques such as plasma enhanced chemical vapor deposition (PEVCD) and thermal evaporation. We have shown that the growth mechanism during amorphous silicon deposition is independent of temperature up to the hydrogen desorption temperature. The static and dynamic scaling coefficients remain constant across this temperature range, with values of  $\alpha = 1.0$  and  $\beta = 0.3$ , consistent with surface diffusion dominated transport.

### **8.1.2 Kinetic Parameters**

The scaling analysis has been used to determine diffusion lengths and extract surface diffusion barriers. The diffusion length was estimated as the lateral correlation length. The correlation length increased with increasing substrate temperature, indicating thermally activated surface diffusion. Arrhenius plots were used to calculate diffusion barriers in the vicinity of 0.2 eV. The barrier depended on the conditions during processing. For films deposited from pure silane precursors, as the process pressure increased, the surface diffusion barrier increased. These results are explained through surface coverage dependent diffusion barriers. The correlation length also decreased with increasing process pressure. At low hydrogen dilutions, the diffusion length decreased, but the barrier remained constant. At higher dilutions, the diffusion length increased and the barrier decreased. The hydrogen was altering the surface hydride coverage.

### **8.1.3 Kinetic Model**

A kinetic model was developed to describe amorphous silicon growth from  $\text{SiH}_3$  precursors. Two key new features differentiate our model from previous models of silicon growth. First, a valence balance was used to account for individual bonds on the surface. This allows for the formation of Si-Si network bonding to be incorporated. Second, a surface hydride dependent surface diffusion barrier was included. The diffusion barrier is based on the supposition that it is easier for a physisorbed radical to

diffuse on a monohydride surface than on a di- or trihydride surface. Model predictions for surface coverage, growth rate, diffusion length, diffusion barrier, sticking coefficient and overall reaction probability were compared with available experimental results. The model reproduced the trends found in experimental results. The model works well between 0.4 and 1.2 Torr for a pure silane plasma. The model does not account for the presence of hydrogen or ions. Deposition under process conditions that promote these species should not follow the model predictions, even in the pressure regime where the model is accurate for silane plasmas. At lower pressures the model also breaks down. This may be due to an increased mean free path of hydrogen in the plasma, allowing hydrogen flux to the surface to become significant.

## **8.2 FUTURE STUDIES**

### **8.2.1 Dynamic Scaling**

Dynamic scaling has been used to characterize amorphous silicon deposition. Next, experiments should be conducted to determine if the scaling coefficients can be related to film electrical properties. The density of states, and light and dark conductivity will be measured for a-Si:H films. The scaling coefficients will also be obtained from topography analysis. The deposition conditions will be varied to obtain high quality amorphous silicon. The scaling coefficients will be related to the film properties. A correlation of the scaling coefficients and correlation length with the film quality would provide a new approach to analyze film quality.

### 8.2.2 Kinetic Model

Our kinetic model has been shown to reproduce the trends found in experimental observations. There are a large number of parameters input into the model. A more detailed analysis of the activation barriers and prefactors for the various reactions is needed to improve the actual values obtained from the model. Experimenting with a matrix of high and low values for the activation barriers and prefactors will provide further insight into the growth process. A careful study of these parameters will help determine which processes are most critical during film growth and improve the predictive capabilities of the model.

Another item that needs to be accounted for in our model is atomic hydrogen. We have shown that the model predictions do not correspond with experimental results at low pressures with atomic hydrogen present. Hydrogen plays an important role in the deposition of high quality amorphous silicon. Hydrogen is active in many reactions during silicon growth. Hydrogen has a low barrier for the abstraction of surface hydrogen to form dangling bonds. It also saturates dangling bonds on the surface. Incorporating hydrogen flux in the model will make it more robust and useful for predicting high quality amorphous silicon.